INFORMATION TO USERS

This manuscript has been reproduced from the microfilm master. UMI films the text directly from the original or copy submitted. Thus, some thesis and dissertation copies are in typewriter face, while others may be from any type of computer printer.

The quality of this reproduction is dependent upon the quality of the copy submitted. Broken or indistinct print, colored or poor quality illustrations and photographs, print bleedthrough, substandard margins, and improper alignment can adversely affect reproduction.

In the unlikely event that the author did not send UMI a complete manuscript and there are missing pages, these will be noted. Also, if unauthorized copyright material had to be removed, a note will indicate the deletion.

Oversize materials (e.g., maps, drawings, charts) are reproduced by sectioning the original, beginning at the upper left-hand corner and continuing from left to right in equal sections with small overlaps.

Photographs included in the original manuscript have been reproduced xerographically in this copy. Higher quality 6" x 9" black and white photographic prints are available for any photographs or illustrations appearing in this copy for an additional charge. Contact UMI directly to order.

ProQuest Information and Learning
300 North Zeeb Road, Ann Arbor, MI 48106-1346 USA
800-521-0600

Sonoluminescence for the Quantitative Analysis of Alkali and Alkaline Earth Chlorides

Alex Lockwood Robinson

A dissertation submitted in partial fulfillment
of the requirements for the degree of

Doctor of Philosophy

University of Washington

2001

Department of Chemistry

UMI Number: 3014109

Bell & Howell Information and Learning Company
300 North Zeeb Road
P.O. Box 1346
Ann Arbor, MI 48106-1346

In presenting this dissertation in partial fulfillment of the requirements for the Doctoral degree at the University of Washington, I agree that the Library shall make its copies freely available for inspection. I further agree that extensive copying of the dissertation is allowable only for scholarly purposes, consistent with "fair use" as prescribed in the U.S. Copyright Law. Requests for copying or reproduction of this dissertation may be referred to Bell and Howell Information and Learning, 300 North Zeeb Road, Ann Arbor, MI 48106-1346, to whom the author has granted "the right to reproduce and sell (a) copies of the manuscript in microform and/or (b) printed copies of the manuscript made from microform."

Signature Alex Rockwood Robinson

Date January 17, 2001

University of Washington
Graduate School

This is to certify that I have examined this copy of a doctoral dissertation by

Alex Lockwood Robinson

and have found that it is complete and satisfactory in all respects,
and that any and all revisions required by the final
examining committee have been made.

Chair of Supervisory Committee:

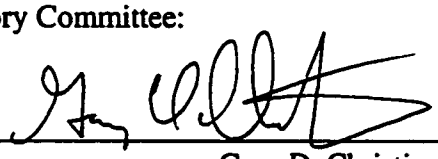

Gary D. Christian

Reading Committee:

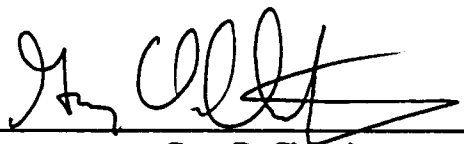

Gary D. Christian

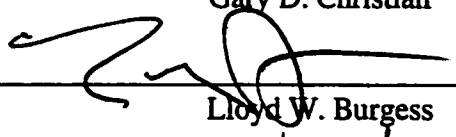

Lloyd W. Burgess

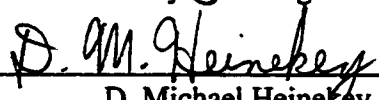

D. Michael Heinekey

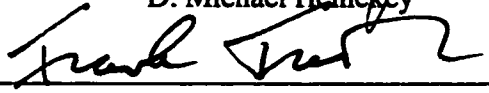

Frantisek Turecek

Date: January 17, 2001

University of Washington

Abstract

Sonoluminescence for the Quantitative Analysis of Alkali and Alkaline Earth Chlorides

Alex Lockwood Robinson

Chairperson of the Supervisory Committee

Professor Gary D. Christian

Department of Chemistry

The use of sonoluminescence for quantitative analysis is demonstrated with possible applications for on-line process measurement. When acoustic energy of sufficiently high intensity is applied to a liquid, microscopic bubbles are generated at weak points in the liquid. These bubbles oscillate non-linearly in the acoustic field, collapsing violently during the compressive phase in a process known as cavitation. Under the right conditions, a subset of the cavitating bubbles emits weak, broadband light, known as sonoluminescence. When certain species are present in a

sonoluminescing system, such as alkali and alkaline earth metals, they emit spectral lines characteristic of their lowest energy neutral excited states. By measuring the intensity and spectral distribution of this radiation, these species may be identified and quantified over a wide range of concentrations. Data is presented from solutions of sodium, potassium, and calcium salts that have been analyzed and quantified from as low as parts per billion up to saturation concentrations. Over this wide range, spectral output is neither linear nor monotonic. Partial Least Squares analysis is used to quantify over these regions, in particular, near saturation. The presence of a second salt alters the emission of the first salt in a predictable manner, still allowing quantification.

An acceptable explanation of the source of sonoluminescence remains to be found. Approximately a dozen theories, some from notable scientists, have been proposed to explain the phenomenon, but the actual mechanism remains elusive and highly debated. Experimental results presented here will argue against some of the more commonly presented explanations. The results suggest that while excitation likely originates from hydrodynamic compression, emission may result from isotropic lasing of the species.

While most of the proof-of-concept data was obtained in a batch reactor cell, there are certain advantages to using a flow cell. Besides being closer to the format of an on-line instrument, sample volume can be reduced with an increase in control over parameters affecting sonoluminescence. Several flow-through cells are described with evaluations of their potential for quantitative analysis and sonochemistry.

Table of Contents

List of Figures

List of Tables

Acknowledgments

I would like to thank Professor Lloyd Burgess for his role in mentoring my advancement through the graduate chemistry program at the University of Washington. His enthusiasm, encouragement, and the diversity of his projects and skills, gave me the courage and freedom to explore new areas within and outside my project. I thank Professor Anatol Brodsky for driving advancements in the theory of my project and for exposing me to a multitude of physical and chemical concepts. I thank Professor Tom Matula from Applied Physics Laboratories for taking an active role in our collaborations and for offering different perspectives on sonoluminescence and sonochemistry. This provided opportunities to expand the project in new directions. For personal friendship and for scientific discussions promoting my intellectual advancement over the past five years, I thank current and former graduate students from the Burgess research group: Dr. David Kuhns, Dr. Benton Free, Dr. Simonida Thurber, Dr. Sean Smith, Dr. Brian Marquardt, and future Drs. Heather Edberg, and Mazen Hamad.

I must also thank my family, without whose support I would never have begun. Thank you to my father and mother, David and Sheila, who exemplified high standards and encouraged high self-expectations in a manner that was never oppressive. Thanks to my brothers Joshua and Anthony, who supported my efforts and helped me out when they could. Finally, thank you to my children, Riggon and Sierra. They are yet too young to appreciate how my hours away from them were in large part for them.

To my parents,
David and Sheila Robinson

and my children,
Riggon and Sierra

Chapter 1

Introduction

A. Acoustics for Chemical Sensing

Acoustics and ultrasonics have been used for physical and chemical analysis in an increasing number of applications over the past 50 years. Information can be obtained from measurements of acoustic velocity, attenuation, backscatter, and chemical acoustic emission. This information can be used to determine percent liquid composition, dissolved gas concentration, interfacial properties, particle size distribution and density, and other physical and chemical properties of samples.[1] With the advent of photoacoustic spectroscopy in the 1970s,[2] acoustics has been used to probe individual molecular energy levels.[3]

Perhaps the most commonly used acoustic sensors for chemical information today are mass sensors, such as QCMs and SAW devices.[4] The mass induced frequency dampening of these first-order sensors can be monitored to quantify analyte concentration. Calibrations formed from the responses of selectively coated mass sensor arrays can be used to identify and quantify molecular classes.[5] Extreme selectivity of individual molecules can be achieved by coating a mass sensor with antigens while

detecting the presence and concentration of the complimentary antibody.[6] A review of other more sophisticated acoustic sensors was recently published in Sensors and Actuators A.[7]

The application of a moderate to high intensity ultrasonic acoustic field to a liquid is another method by which chemical information can be obtained from certain solutions. The acoustic field forces highly non-linear oscillations of tiny bubbles present in the solution in a process known as cavitation. During the violent, inertial collapse of certain bubbles, weak, broadband radiation is emitted (see Figure 2-1, Chapter II). The light, generated from an energy cascade of the acoustic energy, is known as sonoluminescence (SL). By measuring the SL intensity and spectral characteristics, the presence and concentration of alkali and alkaline earth metals can be determined. Recently, SL was mentioned in Analytical Chemistry,[8] amongst other acoustic techniques, as a developing analytical method for determining the concentration of trace contaminants and heterogeneous impurities. It will be shown that quantification at much higher concentrations can also be performed using this technique.

B. Motivation

In the past several decades there has been a move by industry away from cookbook style processing of materials, from precursors to final products. By measuring chemical and physical properties in- or on-line, efficiency can be greatly enhanced. This comes in several forms from determination of an end point, to failure of a chemical

process, to the need for additional reactants. By either directly measuring properties or by making correlations from these measurements, production costs can be reduced through reduction in materials, energy consumption, and time.

The use of sonoluminescence as an on-line analytical technique shows promise for a small range of industrial processes. The instrumentation required includes a spectrometer, a photodetector, and a source of cavitation. The latter may comes in a several forms, most commonly involving sturdy piezoelectric transducers. The method is robust, relatively accurate, and highly resistant to fouling by its nature. While cavitation bubbles are somewhat destructive to all but simple fluids, the affected volume is extremely small in a flow-through format.

Production of sodium hydroxide in the chlor-alkali process is one application that may benefit from quantification through sonoluminescence. Sodium hydroxide is an important precursor to many products in use today. With over 22 billion pounds produced a year (1989), it finds use in the manufacturing of paper, petroleum, polymers, detergents, drain cleaners and aluminum. Chlorine and hydrogen gases are also produced from the process, which is the second largest consumer of energy in the United States, after aluminum production.[9]

In the production of sodium hydroxide, salt water from brine wells is electrolyzed in a mercury cell according to the following equations:

anode:	$2Cl^-_{(aq)} \rightarrow Cl_{2\,(g)} + 2e^-$	$E° = -1.36$ V	(1)
cathode:	$2Na^+_{(s)} + 2e^- \rightarrow 2Na_{(s)}$	$E° = -2.71$ V	(2)
second cell:	$2Na_{(s)} + 2H_2O_{(l)} \rightarrow 2Na^+_{(aq)}\ 2OH^-_{(aq)} + H_{2\,(g)}$	$E° = +1.88$ V	(3)

Unfortunately, it is difficult to find high purity sodium chloride from an economical source. Impurities of calcium, iron, aluminum, and silicon are usually found at ppb levels in the final product. While it would be desirable to quantify all impurities in the system, calcium is of particular importance to some end users of sodium hydroxide. The problem arises when calcium hydroxide or calcium carbonate precipitates from solution, fouling expensive membranes. If a rapid measurement of calcium and sodium concentrations in brine could be made in-line or on-line to the redox chamber, the stream could be redirected when calcium concentration exceeds acceptable levels. The common practice of mixing low concentration brine with high concentration brine to achieve acceptable levels could also be performed on the fly, rather than after the final product has been made and tested. Batches with excessively high calcium concentration could thus be minimized. Another issue with the chlor-alkali process is avoiding sodium chloride saturation in the process cell.

Currently, there is no accurate, economical method for low level, on-line measurement of calcium concentration in the presence of high sodium concentration. Sodium is a strong interferent for the standard calcium electrode. Samples are thus taken from the brine or final product and tested by titration, at the expense of time, reagent, and personnel. When calcium concentration is too high, the product may be post-mixed with low concentration batches to achieve acceptable levels.

A second application area for sonoluminescence is in the production of calcium chloride flakes, also used in aluminum production. This process involves dissolving

limestone with hydrochloric acid. The following neutralization reaction takes place, leaving calcium chloride and a few impurities:

$$CaCO_{3\,(s)} + 2HCl_{\,(aq)} \rightarrow CaCl_{2\,(aq)} + H_2O_{\,(l)} + CO_{2\,(g)}. \qquad (4)$$

One impurity commonly found is 1/2-3/4% sodium chloride in an approximately 45% calcium chloride solution. Density measurements are made on-line to determine the approximate salt concentration. Individual salt percentages are not determined until lab analysis is performed.

On-line quantification using sonoluminescence could benefit both of these applications. Sonoluminescence has been shown to contain spectral emission lines of alkali and alkaline earth metals present in solution. The intensity and shape of the emission lines are related to the concentration of the metals, and to the conditions of the matrix. Sonoluminescence can be induced non-intrusively through a container wall, or directly with an immersion probe, with no need for withdrawing a sample. The only additional requirement of the measurement cell is an optical fiber or viewing port through which to collect the resulting light.

C. Objective

The goal of the research presented in this dissertation was to develop a technique using sonoluminescence to simultaneously quantify sodium and calcium in a flowing stream format. The specific aims were to:

- Characterize sonoluminescence emission from model chemical systems containing concentrations of sodium and calcium relevant to chlor-alkali and calcium chloride production processes.
- Develop and build a prototype cavitation flow cell with integrated cavitation transducer and light collection capabilities in an on-line process stream format.
- Further the theory of the currently unexplained light emission mechanism of sonoluminescence.

In 1997, a doctoral dissertation entitled "The Viability of Multiple Bubble Sonoluminescence for Analytical Applications"[10] was completed by David Kuhns at the University of Washington. Amongst other accomplishments, it showed that sonoluminescence could be used for univariately determining sodium chloride concentration in the ppm range. This dissertation demonstrates a number of advances since then, allowing the use of new techniques for quantification of sodium and additional hard metals over a broader range of conditions and concentrations.

Notes to Chapter 1

(1) Wade, A. P.; Sibbald, D. B.; Bailey, M. N.; Belchamber, R. M.; Bittman, S.; McLean, J. A.; Wentzell, P. D. *Anal. Chem.* **63**, 497A (1991).

(2) Rosencwaig, A.; Gersho, A. *J. Appl. Phys.* **47**, 64 (1976).

(3) Ho, C. K.; Moon, G. J. *Jap. J. Appl. Phys. Part 1* **35**, 2758 (1996).

(4) Janata, J. *Principles of Chemical Sensors*; Plenum Press: New York, 1990; Chapter 3.

(5) Ballantine, D. S. Jr.; Rose, S. L.; Grate, J. W.; Wohltjen, H. *Anal. Chem.* **58**, 3058 (1986).

(6) Welsh, W.; Klein, C.; von Schickfus, M.; Hunklinger, S. *Anal. Chem.* **68**, 2000 (1996).

(7) Hauptmann, P.; Lucklum, R.; Puttmer, A.; Henning, B. *Sens. and Act. A* **67**, 32 (1998).

(8) Workman, J. Jr.; Veltkamp, D. J.; Doherty, S.; Anderson, B. B.; Creasy, K. E.; Koch, M.; Tatera, J. F.; Robinson, A. L.; Bond, L.; Burgess, L. W.; Bokerman, G. N.; Ullman, A. H.; Darsey, G. P.; Mozayeni, F.; Bamberger, J. A.; Greenwood, M. S. *Anal. Chem.* **71**, 121 (1999).

(9) Zumdahl, S. S. **Chemistry**, 2nd Ed. (D.C. Heath and Co., USA, 1989), pp. 813, 1048.

(10) Kuhns, D. W., Ph.D. Dissertation, University of Washington (1997).

Chapter 2

Cavitation and Sonoluminescence

A. A Brief History

Cavitation refers to the generation and subsequent violent collapse of gas and vapor filled bubbles in a liquid under the influence of moderate to high tensile pressure. The phenomenon was discovered in the 1870s when propellers on certain ships did not reach their calculated efficiencies.[1] In 1917 Lord Rayleigh calculated these small bubbles could produce damage equivalent to 10,000 atmospheres of pressure upon their collapse.[2] He constructed the first mathematical model of this effect, though he assumed the process was isothermal. It was reported by Frenzel and Schultes in 1934 that a water bath exposed to acoustic waves could darken a photographic plate.[3] This effect was not due directly to the sound field, but from luminescence caused by cavitation in the water. This was confirmed by a second experiment with the photographic plate outside of the bath. The phenomenon later came to be known as multiple bubble sonoluminescence (MBSL). Cavitation theory has subsequently been refined by others, most recently by Kamath and Prosperetti.[4]

Ultrasonic cavitation occurs when an acoustic field creates cavitation. This effect has found a number of uses over the years. It has been utilized in ultrasonic mixers, cleaning baths, and for medical treatments such as lithotripsy, cauterization, and cancer treatment. The field of sonochemistry may be the least understood application, but advances in understanding continue to be published. When cavitation occurs under a certain set of suitable conditions, sonoluminescence occurs. With the discovery in 1988[5] of conditions whereby a single bubble could be cavitated to sonoluminescence indefinitely, a surge of activity in the field occurred. This resulted in millions of dollars in grants, hundreds of papers, and new hopes for "cold" fusion.[6] While fusion from a sonoluminescing bubble will most likely never occur due to surface instabilities and other effects, the light emission has found use as an analytical signal in a chemical environment.

B. Hydrodynamic Theory

The non-linear motion of an existing or newly generated bubble is determined by stress placed on the fluid. When the pressure P is reduced below the vapor pressure of a liquid P_V, the liquid comes under tension ΔP according to Equation 5. As the tension

$$P_V - P = \Delta P \tag{5}$$

increases, rupture of the fluid occurs at a critical pressure P_c. The theoretical critical pressure of water is quite high. However, omnipresent impurities of dust, dissolved gas, *et cetra* significantly lower this threshold. Under sufficient acoustic pressure, a small

bubble will form at the the site of the rupture and grow during the rarefaction portion of the sound field. The pressure in a simple sound field can be calculated using Equation 6,

$$P = P_o + P_A sin(\omega t) \tag{6}$$

where P_o is the ambient pressure, P_A is the maximum acoustic amplitude, ω is the angular frequency, and t is time. Once a bubble is generated, its radial motion will be driven by the acoustic field for low amplitudes of $P_A << P_o$. With medium- to high-pressure amplitudes, inertial effects become important and the radius of a bubble no longer follows a linear volume change with pressure. At this point, the bubble is said to be cavitating. Formulas that approximate the time-radius curve of such a bubble can be found in Appendix A.

A cavitating bubble grows rapidly through rectified diffusion of vapor and dissolved gases[7] as long as the negative phase of the applied acoustic field lowers the external pressure below the vapor pressure of the liquid. After a cycle of rectified diffusion the maximum radius can be 100 times the equilibrium radius at ambient pressure.[8] Subsequently, the cavity is driven to an implosive collapse as the sound field turns positive and applies a compressive force. Due to surface tension, the bubble may maintain spherical symmetry during most of the collapse,[9] magnifying the acoustic energy, up to 12 orders of magnitude by some estimates.[10] Temperatures[11] and pressures[2] of 10^8 K and 10^5 atmospheres, respectively, have been calculated for collapses of perfect symmetry. These values can not be reached in real systems due to chemical transformations and physical instabilities in the liquid-air interface. In a multiple bubble

field, interaction with near neighbors causes bubbles to collapse asymmetrically in a variety of shapes. These have been shown to greatly magnify the acoustic energy as well, though to a lesser extent.

The impetus behind the violence of a cavitation collapse can be roughly modeled with a few assumptions. If the acoustic pressure is removed from a cavitating bubble, its equilibrium radius at ambient pressure can be observed. The bubble immediately begins to dissolve as its vapor and gas contents diffuse back into the solution. The gas content can be estimated using Henry's law of partial pressures (Equation 7), where P_g is the partial pressure of a gas, H is Henry's constant for that gas, and c_g is the concentration of the gas in the liquid.

$$P_g = Hc_g \tag{7}$$

The sum of the partial gas pressures and the vapor pressure of the liquid gives the total gas and vapor content. If the bubble reaches a maximum radius 100 times larger than the equilibrium radius during cavitation, Boyle's law predicts a million fold decrease of internal pressure. While rectified diffusion continually increases the gas and vapor during the negative phase of the acoustic cycle, it can be seen that the interior is still a weak vacuum in a fluid. When the acoustic cycle turns positive, there is little pressure to prevent a violent collapse.

Cavitation and luminescence may be created in several ways. While not technically sonoluminescence, focused laser pulses and flow constriction tubes (Venturi tubes) can cause cavitation and luminescence by similar bubble dynamics.[12] Typically,

sonoluminescence in a lab is generated using a mechanically focused acoustic horn (cell disrupter, for biologists) or a simple piezoelectric transducer coupled to the liquid through a container wall. If the acoustic energy is sufficiently intense, sonoluminescence will occur, though not every cavitation event will produce light. In fact, very few cavitation events result in cavitation.

Acoustic cavitation bubbles originate at weak points in the fluid. While the dynamic tensile strength of highly purified water has been measured as high as 250 bar,[9] the cavitation threshold for a typical sample is much lower due to seed nuclei. Seed nuclei are present as container walls, dissolved gases, air pockets on dust particles, and may even be initiated by cosmic rays. Any disruption in the intermolecular hydrogen bonding constitutes a weak spot where cavitation may initiate. Once a bubble has formed, cavitational collapse may disintegrate it into multiple new seed nuclei.

Cavitation in a multiple bubble field typically involves hundreds or thousands of bubbles in localized regions experiencing the greatest acoustic stress. It is rather difficult to study any particular event due to time and space constraints. An individual bubble may grow to tens of microns (at 20 kHz), then compress to hundred of nanometers during collapse. After collapse, a bubble may begin another cycle of non-linear growth and collapse, may dissolve, or may disintegrate to a number of new seed bubbles. A single cycle at 20 kHz lasts 50 μs, or 300 ns at 3 MHz. The broadband sonoluminescence flash lasts from 35 to 350 ps, depending on system conditions.[13] Studies of multiple bubble cavitation generally involve time-averaged dynamics of many bubbles.[9]

A new type of sonoluminescence was realized a decade ago. In 1988, Gaitan *et al.* discovered the conditions under which a single bubble could be levitated at the antinode of a simple sound field.[14] At this location, Bjerkness forces[15] counteract buoyancy over a complete acoustic cycle, and the bubble maintains its position to within a few microns. At the antinode, the bubble pulses radially with each acoustic cycle, cavitating and emitting light repetitively. The bubble is not destroyed, but may persist for hours or longer. It is through studying this system that many inferences can be made about the nature of multiple bubble cavitation events and MBSL. Although the time scale of sonoluminescence in the above paragraph was based on single bubble sonoluminescence (SBSL) measurements, measurements of single MBSL events conclude the emission time is significantly shorter than 1 nanosecond, the rise time of the photodetector used.[16,17] Recent experiments by Didenko and Gordeychuk[18] show additional similarities between MBSL and SBSL spectra, strengthening the hypothesis that light emission originates from the same mechanism for both cases. Despite similarities in the generation of MBSL and SBSL, one striking dissimilarity exists. While spectra of MBSL show distinct spectral features, SBSL spectra have smooth profiles, similar to blackbody radiation curves (Figure 2-1). The maximum occurs at approximately 220 nm, where water begins to absorb higher energy UV radiation. Exceptions occur with xenon gas and heavy water (D_2O). When xenon is the only dissolved noble gas, the maximum in SBSL shifts to 340 nm.[13] Heavy water shifts the peak to 450 nm. MBSL spectra show broad emission lines at 280, 310, and 340 nm from relaxation of excited H_2O and OH species.[19] Spectra from both types of sonoluminescence extend into the near infra-red.[20]

Emission lines from alkali and alkaline earth metals, absent in SBSL, are readily observed in MBSL.[21] Early studies[22] suggested these significantly broadened and slightly shifted emission lines could be used as temperature and pressure probes for the internal conditions of cavitation bubbles. More recent studies[23] conclude the emission does not occur in the bubble's interior and that excitation is from high energy radicals produced from the cavitation event. The broadening is due to rapid collisional deactivation in the surrounding liquid. While this provides little information about the pressure and temperature of a bubble collapse, information about the bulk matrix is carried on the signal. It is the spectral lines found in MBSL that provide potential for use in making analytical measurements in cavitating systems.

It has been shown that experimental parameters are extremely important to sonoluminescence intensity and spectra.[24] These include gas type and content, temperature, static pressure, acoustic pressure, driving frequency, and standing wave formations in a cell. The physical properties of a liquid are also important, such as viscosity and vapor pressure.

Temperature and gas content appear to be the two most important factors for maximizing light intensity at a given acoustic pressure. Lowering solution temperature reduces the vapor pressure. With less vapor in the bubble to cushion the collapse, approximately 200 times more light intensity is observed in water at 0°C than at 35 °C.[2] Noble gas doping also has an extraordinary ability to increase sonoluminescence intensity. Diatomic and larger gases, including liquid vapors, have higher molar heat capacities. Thus, these molecules absorb more of the energy of collapse than noble gases.

For the noble gas series, the order of increasing sonoluminescence intensity is He < Ne < Ar < Kr < Xe. This is explained by the decreasing values of thermal conductivity.[25] An interesting facet of sonoluminescence is that a great increase in intensity is seen if even just 1% of the dissolved gases is a noble gas.[2] It has been proposed that noble gases form eximers during the collapse and contribute to light emission.[26] Another theory predicts that non-noble gases are sonochemically "pumped out" of the bubble by conversion to soluble compounds (e.g.: $N_2 + 2O_2 + 2H_2O \rightarrow 2HNO_3 + H_2$).[27] The remaining noble gas then provides the necessary medium for a highly energetic collapse.

Other parameters have the following effects on sonoluminescence with other factors held constant. Increased static pressure increases SL intensity by contributing to a more violent collapse. Above a certain static pressure the acoustic pressure can no longer overcome static pressure, and intensity rapidly decreases to zero. For a homologous series of liquids with increasing vapor pressure, SL intensity decreases. Increased viscosity dampens the radial excursion, decreasing bubble size and SL intensity. Increased surface tension raises SL intensity. Increasing the acoustic pressure also increases SL intensity to a limit. Once a substantial cavitation field is established, bubbles near the acoustic source shield fluid and bubbles further away.[28] Decoupling of the fluid from the source at high acoustic pressures can also occur. All the parameters described above also affect spectral characteristics.

While some papers have tried to explain the effects of acoustic frequency on cavitation,[29] little regard has been paid to acoustic pressure and bubble density. This is largely due to the mechanical nature of resonators, which makes sweeping frequency

space at constant and sufficient transmitted power impractical. Cell resonances change with frequency, affecting bubble cloud populations. Thus, absolute comparisons of frequency effects on MBSL and sonochemistry are difficult. However, several generalizations can be made. First, bubbles grow larger at low frequencies compared to high frequencies. This is due to a longer rarefaction period. The mass transfer time constant for vapor and gas pressure equilibration is significantly longer than the acoustic cycle. The result is more violent collapses at lower frequencies. At higher frequencies, there are more acoustic waves per time unit as well as shorter distances between wave crests. Thus, there are more bubbles collapsing more frequently in a given area per unit time. However, bubbles collapse less violently at higher frequencies. Chemically, the dissociation of water vapor ($H^{\cdot}$, $OH^{\cdot}$, $HOO^{\cdot}$) appears to be the most efficient at low frequencies. However, the longer growth period of the bubble allows recombination to occur. While gas and vapor dissociation is less efficient at higher frequencies, by-products are more quickly delivered to the gas-liquid interface. This trade-off appears to maximize bulk or interfacial sonochemistry around 200 kHz[30]. Lower frequencies appear best for direct decomposition of volatile compounds that can enter the bubble during the rarefaction phase.

C. Theories of Emission

There are a number of theories attempting to explain the origin of sonoluminescence. An adequate theory must explain the picosecond time scale (35-350

ps) and the broadband spectrum (UV to NIR), which has the same emission time over the measured range of 200 to 800 nm.[13] While contending theories are based on either classical hydrodynamics or quantum theory, each has its short-comings. Some theories are more extravagant than others. Only the most important ones are discussed here.

According to one of the earliest and most basic theories, the liquid interface of a bubble compresses the gas and vapor contents so rapidly in the final stages of collapse that the system can be treated adiabatically. The emission mechanism is thermal blackbody radiation or collision induced molecular emission. According to a mathematical simulation at 25 kHz, the temperature would reach a maximum of about 7000 K.[9] Emission should be visible during the 20 ns that the temperature remains over 2000 K. A major failing of this mechanism is lack of an explanation for the short sonoluminescence pulse duration. The emission time would also be longer at the red end of the spectrum.[6]

The shock wave theory of sonoluminescence, first introduced almost 30 years ago,[31] is still commonly considered by experts studying the phenomenon today. The bubble wall is assumed to maintain its spherical symmetry during most of the collapse, reaching a velocity greater than mach 4[6] (6000 m/s in water). The supersonic speed launches a shock wave symmetrically inward from the bubble wall, magnifying the acoustic energy by up to 12 orders of magnitude. [9] While calculations for perfectly symmetric bubble collapse estimate extraordinarily high temperatures and pressures (Chapter II, B), more reasonable estimations of 19,000 K and hundreds of bars have been calculated using hydrogen bomb computer codes at Los Alamos National

Laboratories.[32,33] Radiation is predicted to arise from either a weakly ionized plasma or Bremsstrahlung,[11] which is rapidly quenched according to a poorly explained phase transition mechanism. This theory fails to explain sonoluminescence from bubbles near symmetry disrupting surfaces, where emission generally produces the same spectral characteristics. In multiple bubble sonoluminescence, near neighbors also typically disrupt the sphericity of a collapse. This theory also does not explain the extreme dependence on parameters such as gas content and concentration. These do not detectably change the bubble's macroscopic dynamics, including the minimum measurable radius (~500 nm). [6] They do, however, drastically change sonoluminescence intensity. Recent calculations, which take into account water vapor in the core during collapse, estimate single bubble collapse temperatures of just 5000 Kelvin.[34]

Water fracture, or fracto-luminescence,[35] was proposed by Prosperetti as an alternative mechanism to account for the disparities mentioned above. An argument is made that the bubble cannot maintain sphericity during the latter stages of collapse due to measurable bubble translation during this period. A jet forms from the wall of the trailing side, traverses the interior, and strikes the more physically inhibited leading wall. The time scale of impact is significantly shorter than the time required for the liquid to flow, thus causing "fracture" on the impact side. High pressure from the collapse would also serve to solidify the liquid interface. Light emission could result from from charge separation causing electrical discharge, ionization, or thermal breakdown. Fracto-luminescence is readily seen from crystal fracture of Wint-O-Green Lifesavers as well as from ice.

The cooperative emission[36] mechanism involves a two step process, and compliments classical hydrodynamic theories. First, a population inversion occurs, followed by stimulated, cooperative emission. By one variant, elevated temperature and pressure induces a population inversion of excited molecules and atoms. Another variant has the population inversion occur when the surface double layer is no longer in a thermodynamically favorable orientation due to the rapidly shrinking bubble surface during collapse.[37] When the intermolecular distance of excited species is on the order of the wavelength of an emission event, phase correlation of the electromagnetic radiation may result. Radiation intensity I increases as the square of the excited population N, and the duration equals the spontaneous emission time constant divided by N. In contrast, recent measurements of single bubble sonoluminescence flashes show an increase in peak width with increased intensity. [13]

No theory unambiguously predicts or explains all the data. However, certain theories can be ruled out. In particular, experiments have ruled out thermal blackbody radiation and electrical discharge theories.[38] It has been proposed that there are two types of collapse in multiple bubble fields.[17] The first type is symmetrical, as with SBSL, and may be responsible for the broadband continuum. The second type includes asymmetrical collapses, and may be responsible for spectral features. This leaves open the possibility of more than one emission mechanism.

The chemistry that occurs during and immediately after a collapse in not completely understood. Vapor and gas molecules react due to high temperatures, pressures, and ultraviolet radiation. Intermediates include OH^*, H_2O^*, H_2O_2, HO_2, H^*, $(H_2O{\cdot}M)^*$, and

M*, where M is an inert gas.[39] These are responsible for much of the MBSL spectrum, and most of the sonochemistry of solutes. In MBSL, three bands at 280, 310, and 340 nm have been assigned to the excited hydroxyl radical.[40]

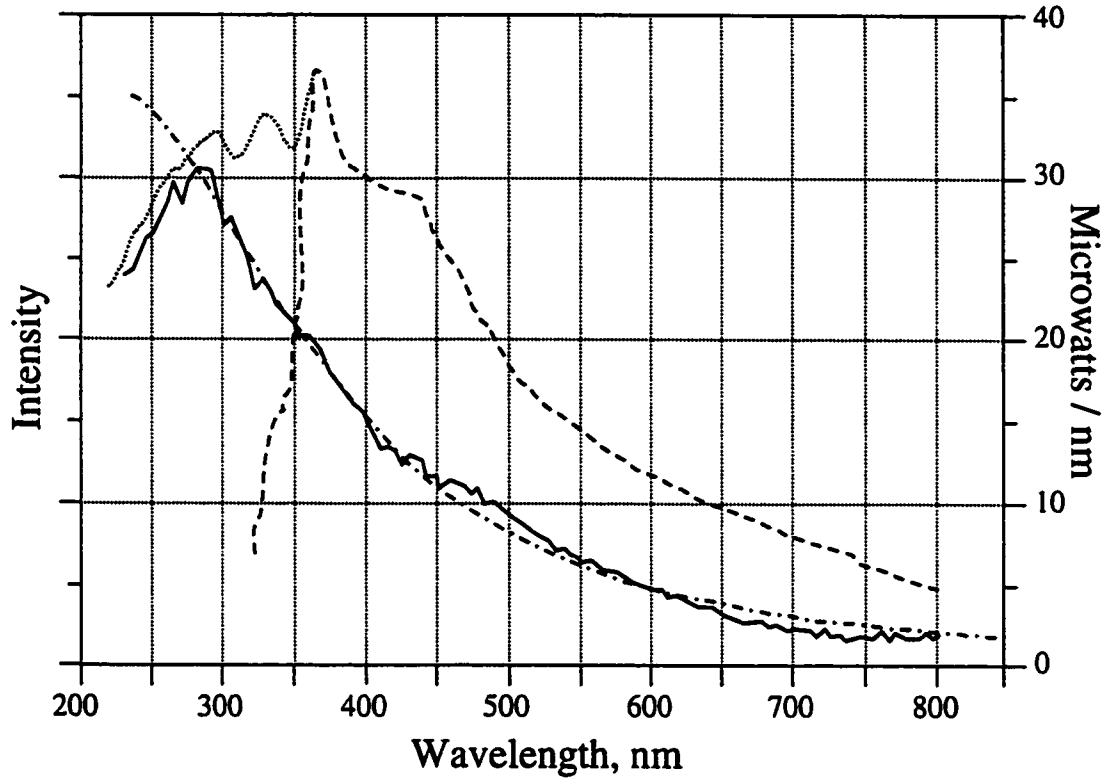

Figure 2-1. MBSL and SBSL Spectra

Adapted from Crum, L. A. *Physics Today* **Sept.**, 22 (1994). The general shapes of MBSL (dashed) and SBSL (solid) spectra are compared along with a best-fit black-body radiation curve (dot-dashed) for the SBSL case.

Notes to Chapter 2

(1) Young, F. R. **Cavitation**, (Mcgraw Hill, New York, 1989) p. 2.

(2) Putterman, S. J. *Scientific American* **Feb.**, 47 (1995).

(3) Frenzel, H.; Schultes, H. *Z. Phys. Chem.* **27B** 421 (1934).

(4) Kamath, V.; Prosperetti, A. J. *J. Acoust. Soc. Am.* **94**, 248 (1993).

(5) Gaitan, D. F.; Crum, L. A. **Frontiers of Nonlinear Acoustics,** 12th ISNA. (Elsevier Applied Science, London, 1990) pp.459-463.

(6) Putterman, S. *Physics World* **May,** 38 (1998).

(7) Crum, L. A. *Ultrasonics* **9**, 215 (1984).

(8) Brennen, C. E. **Cavitation and Bubble Dynamics** (Oxford University Press, New York, 1995) p.65.

(9) Crum, L. A. *Physics Today* **Sept.**, 22 (1994).

(10) Barber, B. P.; Hiller, R.; Arisaka, K.; Fetterman, H.; Putterman, S. J. *J. Acoust. Soc. Am.* **91**, 3061 (1992).

(11) Wu, C. C.; Roberts, P.H. *Phys. Rev. Lett.* **70**, 3424 (1993).

(12) Putterman, S.; Weninger, K.; Hiller, R. A.; Barber, B. P. *Proceedings of the 16th International Conference on Acoustics and the 135th Meeting of the Acoustical Society of America,* p. 2837 (1998).

(13) Hiller, R. A.; Putterman, S. J.; Weninger, K. R. *Phys. Rev. Lett.* **80**, 1090 (1998).

(14) Gaitan, D. F.; Crum, L. A.; Roy, R. A.; Church, C. C. *J. Acoust. Soc. Am.* **91**, 3166, (1992).

(15) Bjerkness, V. F. K. **Fields of Force** (Columbia University Press, New York, 1906).

(16) Matula, T. J.; Roy, R. A. *Ultrasonic Sonochemistry* **4**, 61 (1997).

(17) Giri, A.; Arakeri, V. H. *Phys. Rev. E.* **58**, R2713 (1998).

(18) Didenko, Y. T.; Gordeychuk, T. V. *Phys. Rev. Lett.* **84**, 5640 (2000).

(19) Didenko, Y. T.; Gordeychuk, T. V.; Koretz, V. L. *J. Sound and Vib.* **147**, 409 (1991).

(20) Crum, L.; Matula, T. J.; Robinson, A. L.; Burgess, L. W., manuscript in preparation.

(21) Kuhns, D. W., Ph.D. Thesis, University of Washington (1997).

(22) Sehgal, C.; Steer, R. P.; Sutherland, R. G.; Verrall, R. E. *J. Chem. Phys.* **70**, 2242 (1979).

(23) Flint, E. B.; Suslick, K. S. *J. Phys. Chem.* **95**, 1484 (1991).

(24) Didenko, Y.T.; Pugach, S. P. *J. Phys. Chem.* **98**, 9742 (1994); Barber, B.; Wu, C.; Lofstedt, R.; Roberts, P.; Putterman, S. *Phys. Rev. Lett.* **72**, 1380 (1994); Didenko, Y.T.; Gordeychuk, T. V.; Koretz, V. L. *J. Sound and Vib.* **147**, 409 (1991).

(25) Didenko, Y. T.; Pugach, S. P. *J. Phys. Chem.* **98**, 9742 (1994).

(26) Unnikrishnan, C. S.; Mukhopadhyay, S. *Phys. Rev. Lett.* **77**, 4690 (1996).

(27) Lohse, D.; Brenner, M. P.; Dupont, T. F.; Hilgenfeldt, S.; Johnston, B. *Phys. Rev. Lett.* **78**, 1359 (1997).

(28) Gutierrez, M.; Henglein, A. *J. Phys. Chem.* **94**, 3625 (1990).

(29) Didenko, Y. T.; Nastich, D. N.; Pugach, S. P.; Polovinka, Y. A.; Kvochka, V. I. *Ultrasonics* **32**, 71 (1994); Entezari, M.H.; Kruus, P.; Otson, R. *Ultrasonics Sonochemistry* **4**, 49 (1997).

(30) Petrier, C.; Francony, A. *Ultrasonics Sonochemistry* **4**, 295 (1997).

(31) Jarman, P. D., *J. Acoust. Soc. Am.* **32** 1459 (1960).

(32) Moss, W. C.; Clarke, D.; Young, D. *Science* **276**, 1398 (1997).

(33) Moss, W. C., *et al.*, *Phys. Rev. E* **59**, 2986 (1999).

(34) Storey, B. D.; Szeri, A. J. *Proc. Roy. Soc. Lond. A* **456**, 1685 (2000).

(35) Prosperetti, A. *J. Acoust. Soc. Am.* **101**, 2003 (1997).

(36) Mohanty, P.; Khare, S. *Rev. Mod. Phys.* **80**, 189 (1998).

(37) Brodsky, A. M. *Mod. Phys. Lett. B* **13**, 1019 (1999).

(38) Suslick, K.; Kemper, K. A. *Ultrasonics* **31**, 463 (1993); Hiller, R. A.; Putterman, S. J.; Weninger, K. R. *Phys. Rev. Lett.* **80**, 1090 (1998).

(39) Didenko, Y. T.; Pugach, S. P. *J. Phys. Chem.* **98**, 9742 (1994); Didenko, Y. T.; Gordeychuk, T. V.; Koretz, V. L. *J. Sound and Vib.* **147**, 409 (1991); Gordeychuk, T. V.; Didenko, Y. T.; Pugach, S.P. *Acoustical Physics* **42**, 240, (1996).

(40) Didenko, Y. T.; Nastich, D. N.; Pugach, S. P.; Polovinka, Y. A.; Kvochka, V. I. *Ultrasonics* **32**, 71 (1994).

Chapter 3

Experimental Instrumentation and Procedures

A. Instrumentation

The instrumentation required for generating and measuring sonoluminescence consists of several components. These can be broken down into two categories. First, standard spectroscopic optics are required for dispersing and detecting the light. Sonoluminescence in general is quite dim. This necessitates high quality optics and sensitive photodetectors. A simple photo multiplier tube (PMT) may be sufficient for measuring the total broadband emission. However, when the light is dispersed as with a grating, photon counting PMTs or charge coupled device (CCD) arrays are most useful for measuring the spectra. An advantage of a liquid nitrogen cooled CCD array detector is that thermal noise is extremely low, and integration times of many hours may be used. This is useful to compensate for wavelengths removed from the region of a grating's peak sensitivity, or near the edges of the detector's useful range. This can greatly increase signal to noise. A disadvantage of a CCD array is that it is sensitive to cosmic rays. When the array absorbs a cosmic ray, it registers a sharp peak of one to two pixels wide, and up

to thousands of counts higher than surrounding pixels. Multiple cosmic rays may register in a single spectrum during longer data acquisitions.

The second category of equipment consists of an alternating current (AC) power supply, a piezoelectric or magneto-restrictive oscillator (acoustic transducer), and a sample cell. A transducer is the circuit equivalent of an inductor, capacitor, and resistor in series. Thus, certain frequencies resonate when a transducer is driven with an AC voltage, causing enhanced mechanical displacement. The power supply and transducer should have matching electrical impedances when the transducer is driving a load (a load is any mass against which the force of the transducer acts). When this condition is satisfied, electrical energy is most efficiently coupled into mechanical motion. The remainder of the energy is dissipated as heat in the circuit. With poorly matched electrical impedance, energy reflection occurs, resulting in an overload of the power supply. A good power supply will automatically shut down before this state causes damage.

The transducer may either drive a solution directly or through the bottom or wall of an acoustic cell. If the latter is chosen, care must be taken to closely match the acoustic impedance of the transducer and cell material. The acoustic impedance Z is the product of the speed of sound c and the density ρ of a material. As with any wave, reflections occur at interfaces where physical properties change. The ratio of the transmitted pressure p_{trans} to the incident pressure p_{inc} can be estimated from Equation 8, where subscript 2 refers to the second medium. Quarter-wavelength matching also improves the transfer of acoustic

energy, whereas half-wavelength multiples increase the reflected power. Quarter-wavelength matching is not useful when the frequency of the transducer is scanned.

$$\frac{p_{trans}}{p_{inc}} = \frac{Z_2}{Z_2 + Z_1} \tag{8}$$

A number of custom acoustic cell/transducer pairs were evaluated. However, most of the data presented in this thesis was acquired using the system that provided the best stability and generated the brightest SL emission. Other cell/transducer pairs will be described as needed.

The main acoustic cell was originally designed and fabricated by former graduate student David Kuhns (Ph.D., UW 1997). Several modifications have since been made, resulting in the instrument described here (Figure 3-1). The centerpiece around which the cell was constructed is an acoustic horn from Sonics and Materials, Inc. (model CV26). An accompanying 400 Watt power supply (model VCX400), drives the horn at 20 kHz. The horn has a 5" mechanically focusing tapered probe, with a replaceable 0.5" diameter titanium alloy tip. These tips were replaced as needed, when the cavitation damage caused excessive pitting. Figure 3-2 shows a new horn tip next to one that has been used for approximately 50 hours. The probe of the horn is pipe threaded in the middle. A 304 stainless steel, double-walled, cylindrical cell (3.5" I.D. x 4.14" inner length) was fabricated with compatible thread. When the horn is inserted, the tip is 0.7" away from a 1" quartz window at the bottom end of the cell. The window is sandwiched between two O-rings and is held in position by compression with a hollow, threaded plug. Coolant from a refrigerated circulator flows between the double walls for temperature control. For

additional thermostatting, solutions were pumped at a rate of 4 liters per minute through a stainless steel coil submerged in the coolant of the refrigerated circulator, and then returned to the cell. With typical test solution volumes of 80 mL, the turnover rate is 50 times per minute. A number of other ports are also present. A membrane pressure sensor (Omega, model PX-203) and a T-type thermocouple (Omega) occupy two ports for measuring headspace pressure and fluid temperature, respectively. Below the fluid level argon or other gases can be introduced for sparging. The gas flows from an argon tank into a 5 L reservoir, and then out to a T-valve. In one direction, the gas is directed through a frit submerged in DI water, where it saturates with moisture before flowing through the sparging port. The other T-valve position directs the gas through a port above the fluid level, enabling regulation of headspace static pressure up to 100 p.s.i. A relief valve prevents higher pressures. Other ports are present for releasing headspace pressure and discharging waste solution.

A custom-made AC complex-power meter was inserted in-line between the power supply and acoustic horn. The meter measures the voltage and current from a power supply driving a loaded transducer. Five electrical parameters are output: instantaneous voltage, current, and power, the phase difference between voltage and current, and average reactive (real) power. Reactive power is the mechanical energy transmitted to the load. Using the phase difference, average consumed (imaginary) power can be calculated, which is that portion of the energy that results in heating of the circuitry.

During cavitation SL was collected with fiber optics through the quartz window. The use of 1,5-pentadiol for index matching was found to increase light collection,

despite the resulting reduced collection angle. The optical fiber most commonly used consists of a bundle of twenty-four 200 micron glass on quartz fibers from Oriel. At the collection end the fibers were circularly packed in an STA connector. At the other end the fibers were reorganized into a stack, which was aligned with the entrance slit of a spectrometer when spectral data was acquired. When total light output was monitored, a 1 mm glass on glass fiber was used.

Due to the broadband, low light level of sonoluminescence, various detectors were used depending upon the characteristics of the data desired. For fast, temporal data, a Hamamatsu PMT (model H5783-01) with a 0.65 nanosecond rise-time was used. A Hamamatsu photon counting PMT module (model HC135-01) was used while evaluating new acoustic cells when SL was particularly dim. CCD arrays were used when collecting spectral data.

A 0.3 m McPherson spectrometer (model 218) was used when collecting most of the spectral data. A fiber adapter was attached to the entrance, and an extension tube with a set of two f-number matching lenses focused the light through the entrance slit. Either a 300 or 600 groove/mm grating was used, depending on the resolution and wavelength range desired. Both gratings were blazed at 500 nm. Diffracted light fell upon a liquid nitrogen cooled Princeton Instruments CCD camera (model LN/CCD-576E/1UV) with a 576 x 384 pixel array. The background hot electron count was less than one per pixel per hour with a read noise of 6-8 electrons. With the fiber optic stack, only 12 of the 24 fibers were imaged through the spectrometer optics, and they vertically filled the CCD array. With this optical path and the 600 groove/mm grating, the 585 nm line from a neon lamp

measures 0.2 nm FWHM. Wavelength calibrations were performed with the neon lamp for wavelengths longer than 550 nm, and a mercury lamp for shorter wavelengths. Wavelength calibration errors were on the order of ±0.1 to ±0.2 nm, depending upon the number and position of calibration lines in a spectral region.

B. Experimental protocol

Solutions for analysis were made with water deionized with a Barnstead NANOpure filtration system to an initial resistivity of 17.0-17.8 MΩ/cm. Salts from Fisher and J. T. Baker were used with no additional purification.

For experiments in the stainless steel cell, the cell was cooled in advance to 5 ± 1 °C. Solutions were introduced to the cell where they were sparged with argon for approximately 30 minutes prior to experimentation. Samples were then sonicated with an average reactive acoustic power density of 12.5 W/cm^2, unless otherwise noted, for 10 minutes prior data acquisition. This allowed the dissolved gas content to establish a new equilibrium. Despite the acoustic energy deposited in the cell by the horn, the temperature remained constant at 5 ± 1 °C. Solutions for flow cell experiments were not preconditioned. Approximately 2 hours before data acquisition, the CCD detector was cooled with liquid nitrogen. The dark noise and sensitivity stabilized within ½ hour of achieving an equilibrium temperature of approximately –110 °C.

C. Data Collection and Analysis

For certain experiments, pressure, temperature, and/or PMT signals were digitized with a DASH16jr (Computer Boards, Inc.) A/D card connected to a Pentium powered PC. Data was acquired using programs written in LabVIEW® (National Instruments, Inc.). Data from the CCD camera was collected using Princeton Instrument's Winspec software. Acquisition times varied from 30 seconds to 30 minutes, depending upon the intensity of the emission lines and background sonoluminescence. Data was converted into ASCII and imported into Matlab® (The MathWorks, Inc.) for analysis.

As mentioned above, long integration times are possible when the CCD array is liquid nitrogen cooled. However, this proportionally increases the odds of cosmic rays striking the array. Cosmic rays typically strike the 0.5" x 0.33" array in the Princeton Instruments detector at a rate of one per minute, though this rate can vary widely. The effect of a cosmic ray being absorbed by a CCD pixel is an anomalously high count on that pixel. The sudden charge spike may affect adjacent pixels as well. During post-processing of data acquired over periods longer than tens of seconds, it was useful to mathematically correct the charge count on pixels affected by cosmic rays. Two similar programs with different approaches were written to automate this step. When few spectra were taken, as was often the case when long integration times were required, cosmic rays were identified spatially. The algorithm searched each spectrum individually, wavelength by wavelength, for sudden jumps in intensity that were too narrow to be spectral peaks. The user was then prompted to confirm that each identified peak was indeed a cosmic

ray. The high value was then replaced with the average value of several surrounding data points. When larger numbers of similar spectra were obtained, cosmic rays were identified temporally. The algorithm compared all the spectra together, a single wavelength at a time. Sudden increases in intensity appearing in only one to several spectra at that wavelength were identified. Their values were then replaced by the average value of the unaffected data points from the other spectra at the same wavelength. Both algorithms performed extremely well (Figure 3-3), but they were prone to errors when high numbers of cosmic rays struck the CCD array in a single data matrix. For this reason, spectra were checked visually for errors after cosmic ray correction. The algorithms are included in Appendix C.

For certain analyses of SL spectra, the height and width (FWHM) of spectral lines were measured. As the overall intensity of SL increases with the addition of most salts, a pure water spectrum could not be used for a background subtraction. Thus, straight lines from the edges of the spectra or from other local minima were used when determining peak height and width. This results in an approximation, especially in the case of sodium D lines, where the tails of the doublet appear to extend more than 100 nm in both directions.[1] However, these tails decay very rapidly more than a few nanometers from the main peak. The spectral response through our optical train was determined to be nearly linear within the spectral windows of interest, and the spectra reported here are thus uncorrected for intensity deviations.

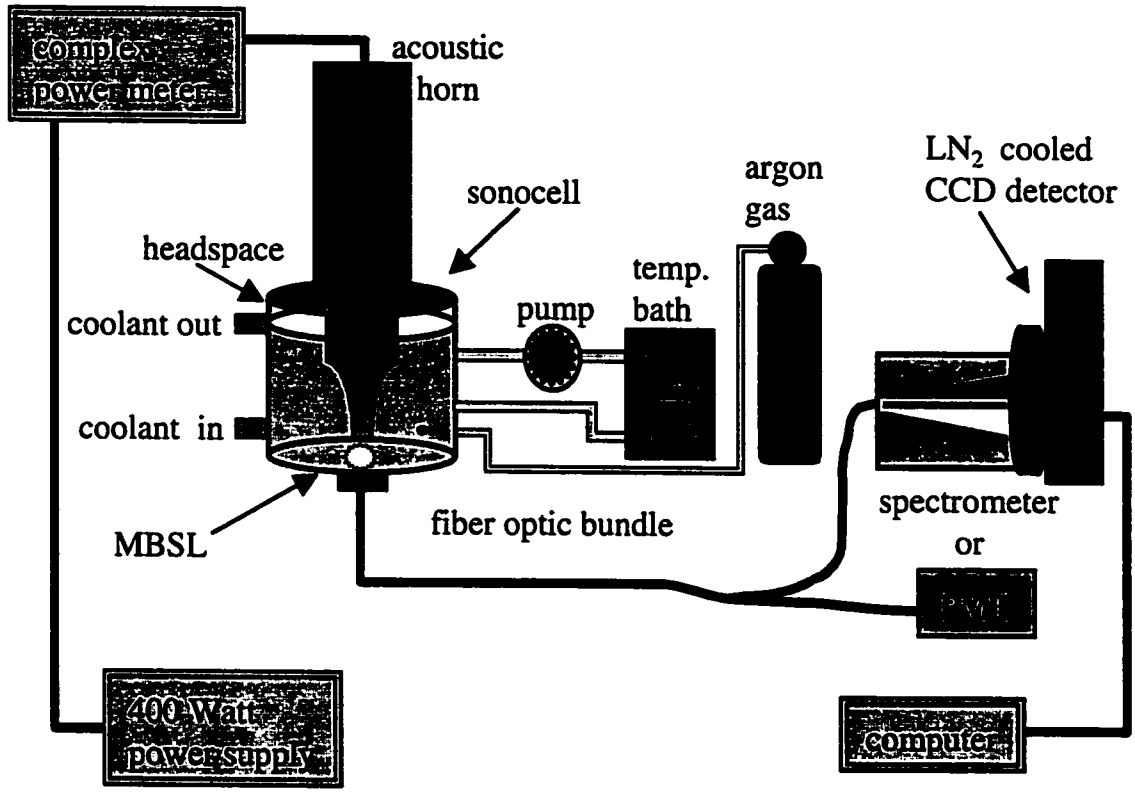

Figure 3-1. Main MBSL Apparatus

The main apparatus for MBSL experiments included ultrasound generating equipment, a conditioning system for samples, and instruments for collecting, dispersing and detecting light.

Figure 3-2. Cavitation Damage

Replaceable titanium alloy tips for the 20 kHz horn are shown. The new tip on the left is smooth and highly reflective. The tip on the right has been used for approximately 50 hours, and has deep pitting from cavitation damage.

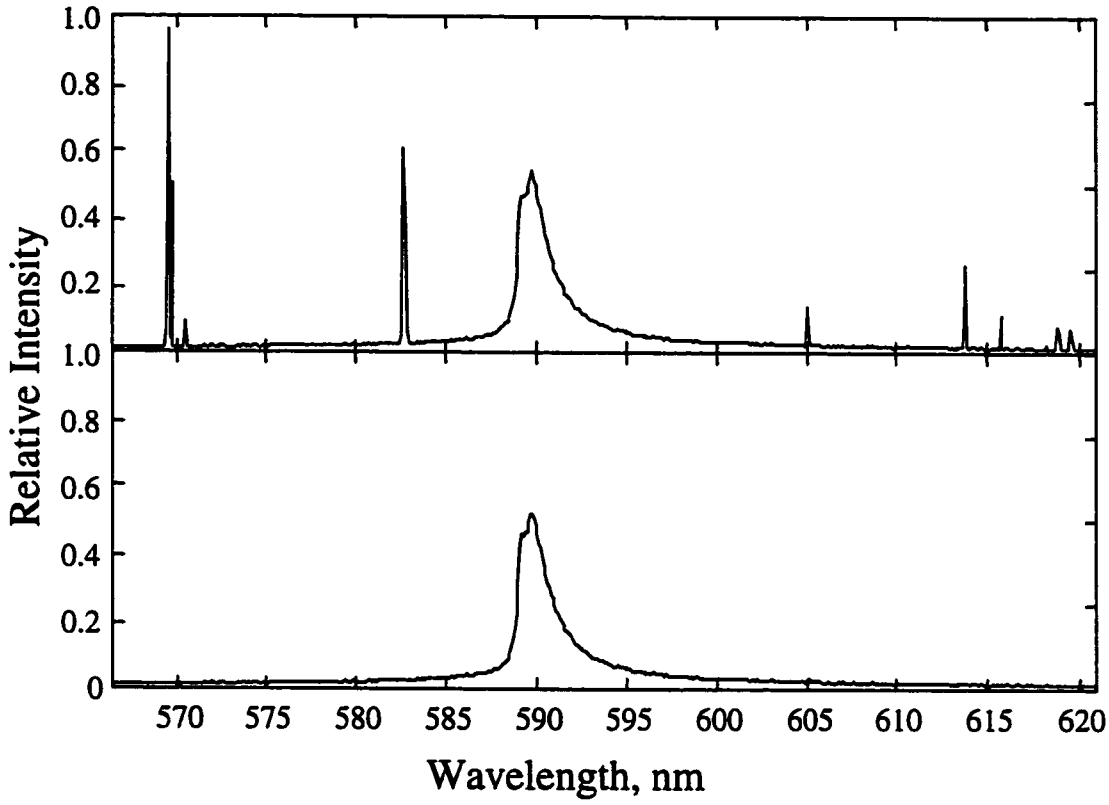

Figure 3-3. Cosmic Ray Removal

Cosmic rays can be detected by the CCD array. The upper plot shows an MBSL spectrum with narrow peaks from cosmic rays surrounding a significantly broader analyte emission peak. The lower plot shows the analyte peak after application of the temporal cosmic ray removal algorithm. The plots were from the maximum values of ten 60 second integrations of 1.0 M NaCl.

Notes to Chapter 3

(1) Sehgal, C.; Steer, R. P.; Sutherland, R. G.; Verrall, R. E. *J. Chem. Phys.* **70**, 2242 (1979).

Chapter 4

Characterization of the Sonoluminescing System

With the development of any new sensor, instrument, or technique, the signal response must be characterized. The response in this case is sonoluminescence, which is highly affected by certain parameters. For this reason, care was taken to control such variables as temperature, static and acoustic pressure, and gas content. By holding external variables constant, the total sonoluminescence response to solution parameters has been used to analytically quantify the concentration of surface modifiers.[1] The affects of changing system parameters and the stability of the signal at a given set of parameters were explored to optimize the signal.

A. Temperature

The effects of temperature on the response from the main acoustic cell were characterized previously. It can be seen from Figure 4-1 that the total SL intensity increases with decreasing temperature. As SL is inherently dim, the temperature was kept around 5 ± 1 °C for most experiments. Stability of a lower temperature was not possible with current thermostatting equipment due to ultrasonic heating of the solutions. Within

the range of temperature variability, little change in SL intensity occurred. When spectra were acquired, that variability was averaged over the integration time from 30 seconds to 30 minutes for each spectrum.

B. Temporal Characteristics of SL

Once the SL signal was maximized, an experiment was performed to determine the temporal characteristics of SL in the stainless steel cell. From the literature it was known that the picosecond flashes of SL are orders of magnitude faster than the sub-nanosecond rise time of the model H5783-01 Hamamatsu PMT. However, it was possible to measure the phase of SL emission relative to the acoustic cycle.

Typically, a preamplifier is used to magnify the signal of a PMT. However, it was found that the time constant with the preamplifier was too long relative to the 20 kHz acoustic cycle. This resulted in temporally stretched signal responses, approaching a nearly DC current at the output of the preamplifier. To achieve better temporal measurements, the output of the PMT was connected to the input of a LeCroy 9350AM 500 MHz digital oscilloscope. With the oscilloscope's input impedance set to 50 Ohms, the signal response was too low to measure. With the alternate 1 MOhm input the signal was sufficient, but the rise time was too slow. A compromise between rise time and signal strength was achieved by selecting the 1 MOhm input and attaching a modified BNC T-connector. The T-connector was fitted with a 10 kOhm resistor in parallel with

the PMT (Figure 4-2), resulting in moderate signal amplification and a 0.15 nanosecond time constant.

The average of 1000 oscilloscope acquisitions is shown in Figure 4-3. The phase of the acoustic cycle is measured relative to the tip of the horn. SL occurs during most of the acoustic cycle, reaching a maximum at approximately the zero crossing of the acoustic cycle. Some emission continues to occur even as the acoustic cycle achieves its maximum negative pressure. There are two explanations for this observation. First, the maximum acoustic pressure in the liquid has a temporal delay from the horn tip due to the finite speed of sound in the liquid (~1.5×10^5 cm/sec for void-free water). The depth of the emission zone from the horn tip to the viewing port is approximately 1.9 cm. Thus, the maximum acoustic pressure is present in the fiber optic's field of view for nearly 25% of the acoustic cycle. In reality, the presence of bubbles rapidly decreases the speed of sound in water, further lengthening this period. A secondary effect results when the acoustic energy scatters through the cell in complex and unpredictable paths. Constructive and deconstructive interference can briefly produce highly localized areas of high and low pressure.

C. SL Stability and Reproducibility

Once system temperature had stabilized before an experiment, argon gas was sparged through the solution for ½ hour or longer to remove other dissolved gases. The argon itself (or other noble gases) is essential to increasing SL intensity through a

mechanism that remains debated. At the beginning of cavitation, solutions partially degas some of the saturated argon. SL intensity is the brightest as this process begins, stabilizing at a new intensity when dissolved argon achieves a new equilibrium (Figure 4-4). This typically takes less than 10 minutes, at which point data acquisition began.

For constant parametric conditions, SL spectra were quite reproducible. Experimental variability in intensity was typically ±35 counts, with a standard deviation of 20 counts for a set of ten spectra. Integration times were usually chosen such that spectral peaks had intensities of at least several thousand counts. Thus, run to run variations in the peak heights were generally less than 1%. When peak width was measured, typical variations of ±0.02 nm were measured. With the narrowest peak widths measuring 1 nm FWHM, errors were within 2%, and typically less than 1%. Run to run reproducibility over the entire spectra was usually 98%, with the largest relative errors occurring at the ends of the spectra. Figure 4-5 shows the reproducibility of spectra from three solutions of 1.0 M sodium chloride taken on separate days.

D. Effects of Static Pressure

Static pressure plays an important role in the process of acoustic cavitation. Besides affecting dissolved gas concentration, it heavily influences the dynamics of cavitation bubbles (Appendix A). Static pressure opposes bubble inception and expansion during the rarefaction phase, and combines with the acoustic force during the compressive phase. As the static pressure is increased for a given acoustic pressure, the

intensity of the bubble collapse, and hence cavitation, increases up to a certain point. Beyond this point, suppression in the growth of the cavitation bubbles begins to offset the enhanced collapse violence. SL begins to rapidly decrease beyond the threshold pressure, eventually becoming completely quenched.

The effect of increasing static pressure on total SL intensity is shown in Figure 4-6 and Figure 4-7 for DI water and 1.0 M NaCl, respectively. In the experiment, total SL intensity was measured while the static argon headspace pressure was alternately increased and decreased. For DI water, the intensity closely relates to a function of the static pressure, with the exception of the local minimum around 2.7 bar. With the sodium chloride solution, the intensity shows hysteresis dependant upon the prior static pressure. Compared to DI water, solutions of most salts have a significantly smaller average bubble size and a proportionally higher number density. These are affected by the state of the system, in particular static pressure. The effect of their persistence upon the way static pressure is changed is observable in the SL signal. The threshold pressure for both solutions above which SL intensity begins to decrease is 3.4 bar. The acoustic cell was not able to withstand the pressure required for total SL extinction, which is extrapolated to 5.2 and 5.9 bar for water and 1 M NaCl, respectively.

An interesting observation around which Kuhn's thesis was based was termed the "pressure jump." In such an experiment, sodium chloride solutions being cavitated at atmospheric pressure were rapidly subjected to a sudden increase in static pressure (Figure 4-8). The new pressure was held constant, typically 1-2 bars above atmospheric pressure. The effect on SL was to immediately increase its intensity by up to two orders

of magnitude. This enhancement could last up to several minutes, after which the intensity would decay to a new equilibrium intensity dependant upon the final static pressure. The excitation and decay profiles of SL intensity were used to quantify various trace alcohols in solution in the above-mentioned thesis.

It appears that the pressure jump effect results from dynamic equilibration of the solution to the new static pressure. This involves changes in the dissolved gas concentration and the bubble number, size, and distribution. Visual observations of the cavitation zone were made during a pressure jump. While initially visible cavitation bubbles shrink beyond observation, audible cavitation noise greatly increases. Over the course of approximately two minutes, during which time the new SL equilibrium is typically established, bubbles in the cavitation zone grow to visible sizes again. They remain at these sizes until the excess static pressure is relieved. When the pressure is released, the solution froths up bubbles, much like when a shaken up carbonated beverage is opened.

An interesting observation of SL intensity can be made during a pressure jump when the acoustic pressure is interrupted after the static pressure has been increased. With no acoustic cavitation, SL intensity drops to zero. After resuming acoustic power, SL intensity immediately increases to the level where it would have been had the acoustic power never been interrupted (Figure 4-8). This experiment provides evidence that the source of enhanced SL is manifested in the state of the solution, independent of acoustic pumping. New equilibrium likely occurs when the dissolved gas content re-equilibrates.

With rapid pumping (4 L/min) and a dearth of microscopic bubbles to dissolve, new equilibrium is achieved after approximately two minutes.

E. Acoustic Pressure

As higher intensity acoustic energy is transmitted into a liquid, the intensity of acoustic cavitation increases. This is manifested both as more cavitation bubbles as well as more violent collapses of those bubbles. The effect, which increases SL intensity as well, increases up to a limit. Because the acoustic impedance mismatch between water and gas bubbles is fairly large, a phenomenon known as acoustic shielding occurs. As more bubbles with larger cavitation diameters populate the region near the acoustic source, acoustic shielding increases for regions further from the source. At even higher acoustic intensities, the source may momentarily decouple from fluid. A plot of SL intensity versus acoustic power (Figure 4-9) shows how SL intensity increases linearly at first, then asymptotically levels off as acoustic energy saturates.

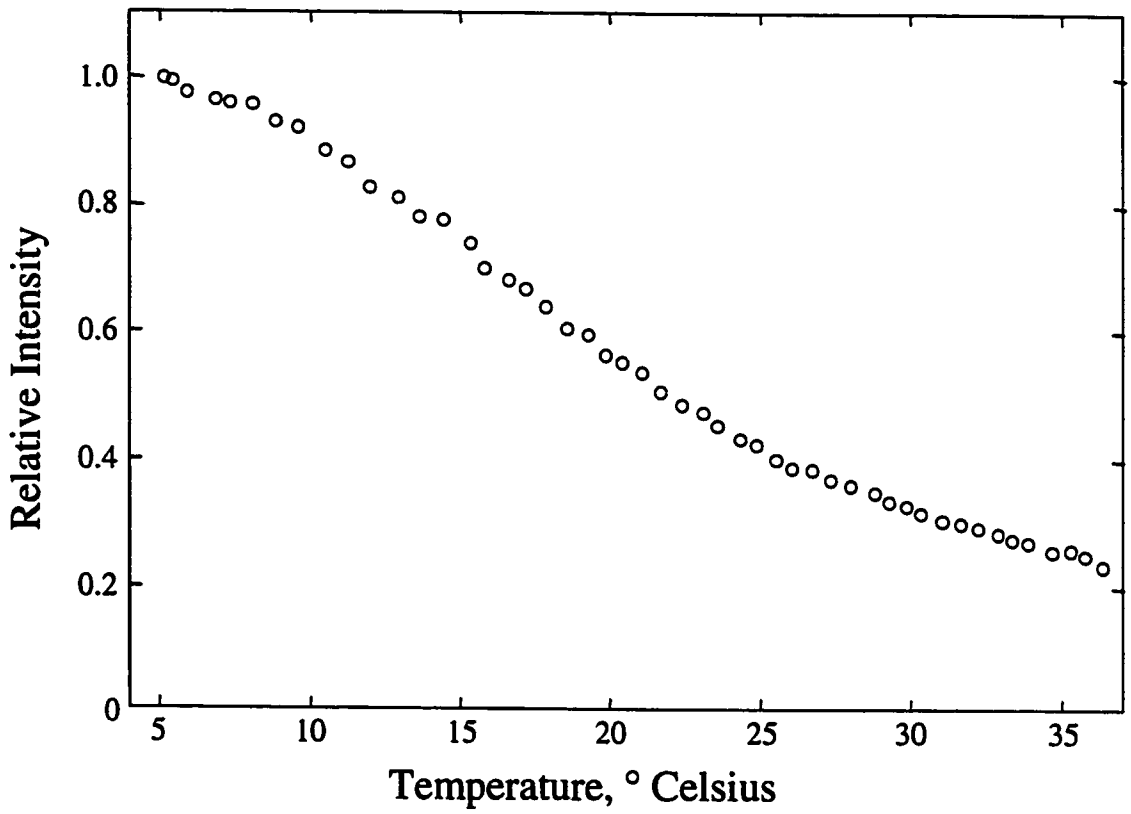

Figure 4-1. Temperature Dependence of MBSL Intensity

Sonoluminescence intensity increases as temperature is lowered due to decreased vapor pressure cushioning the violence of cavitational collapse. Above, total SL was collected from DI water driven with the acoustic horn system

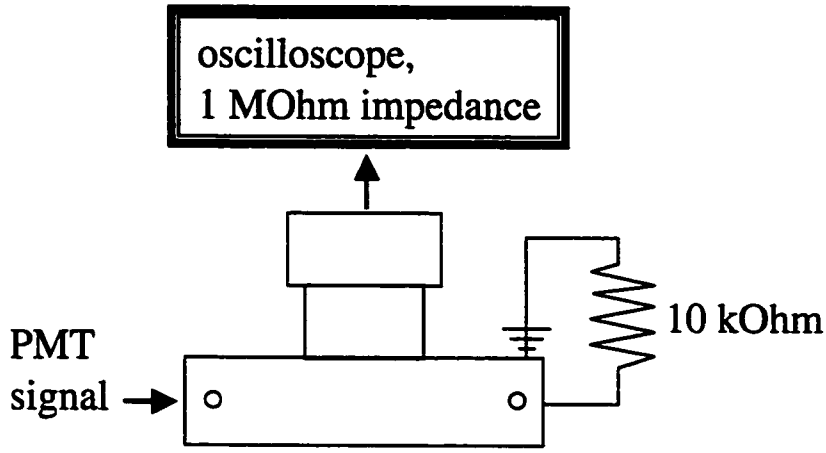

Figure 4-2. Signal Amplification Circuit

To balance sensitivity and rise time between the PMT and oscilloscope, the above circuit was constructed with a BNC T-connector and a 10 kOhm resistor. The time constant and amplification were 0.15 ns and 1 volt/amp respectively.

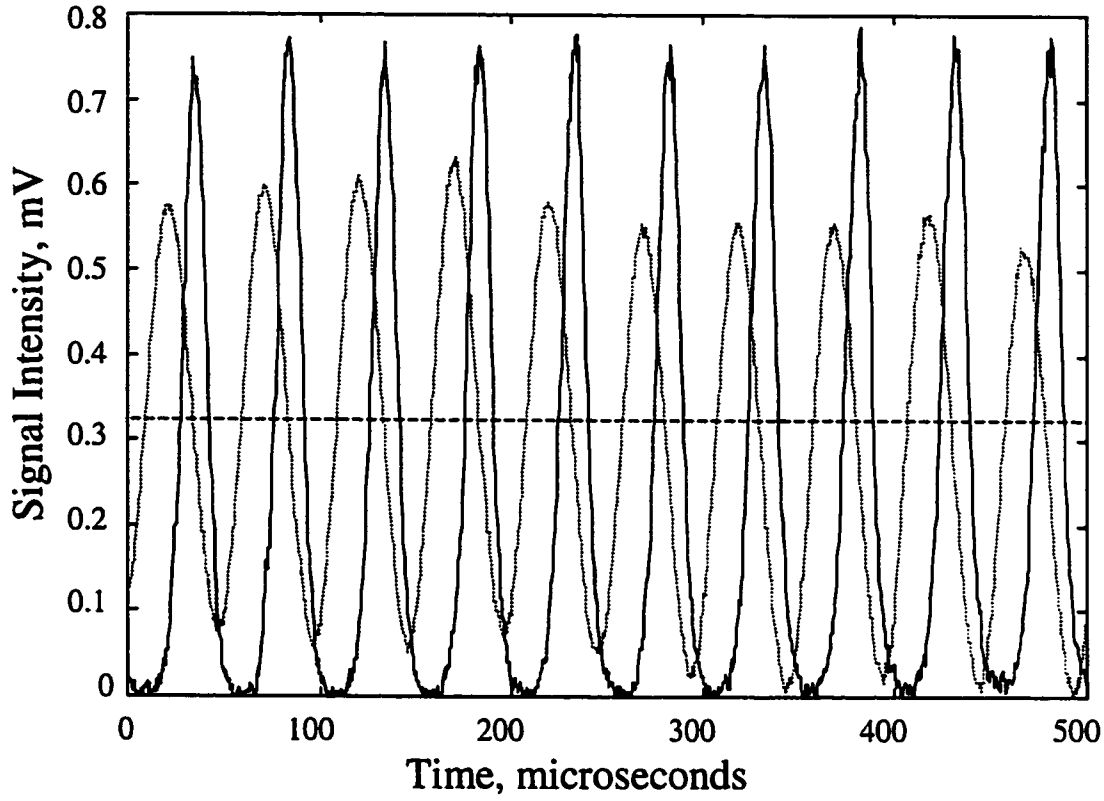

Figure 4-3. Temporal Characteristics of MBSL

The phase of MBSL spatially averaged through the cell volume (solid line) is shown relative to acoustic cycle (dotted line). The acoustic cycle has been offset with zero amplitude at the dashed line for clarity.

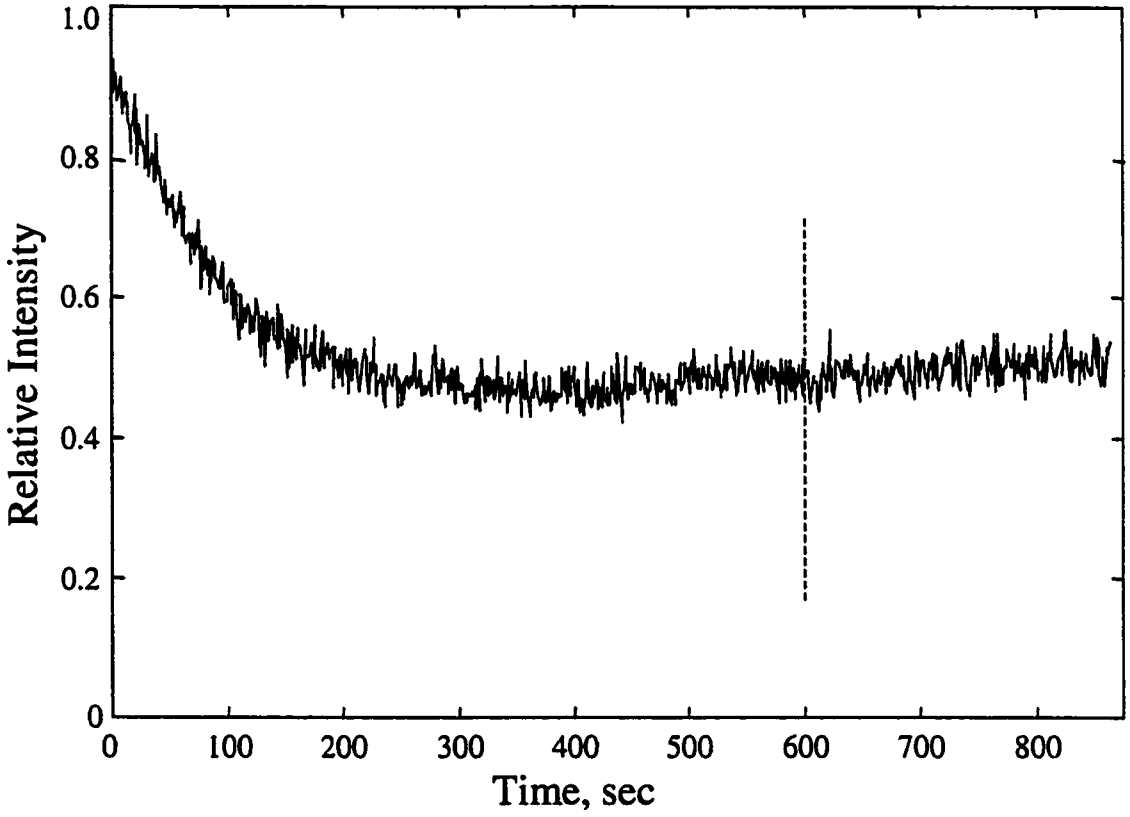

Figure 4-4. Effect of Cavitational Degassing on MBSL

Total MBSL decreases as the solution degasses (1.0 M NaCl above). Equilibrium intensity can take up to 10 minutes (dashed line) to stabilize, at which point data acquisition could begin.

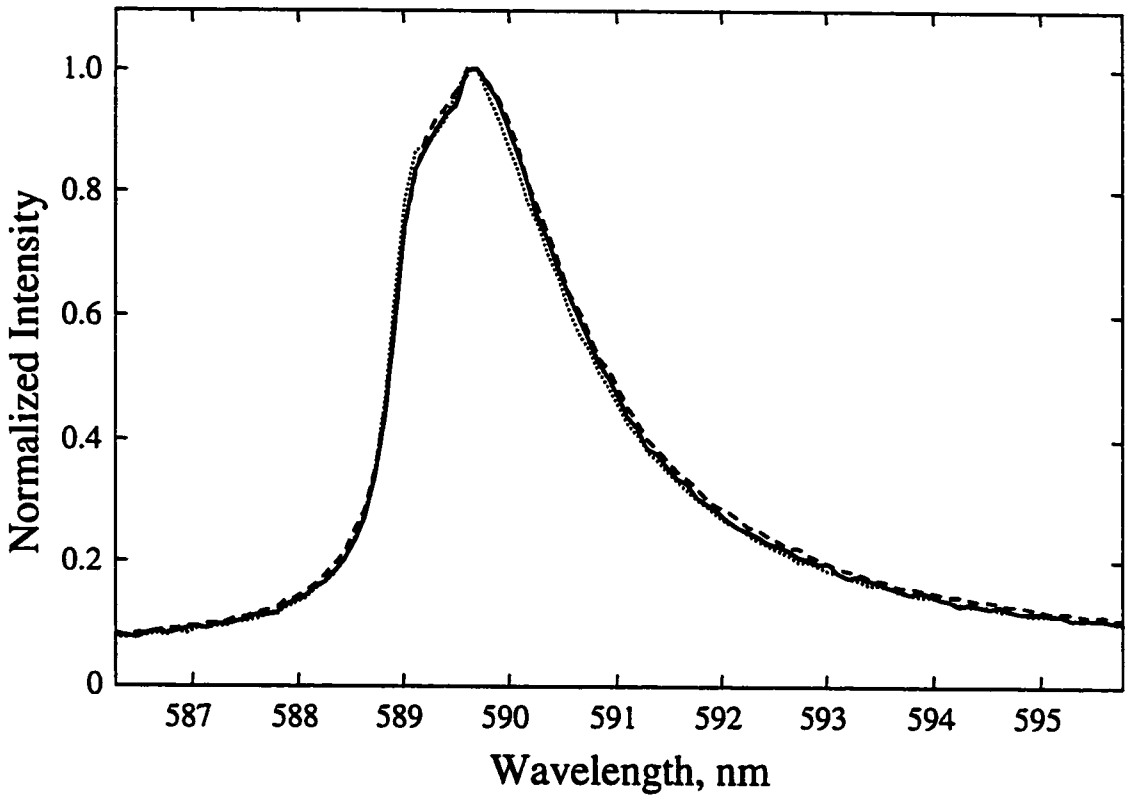

Figure 4-5. Reproducibility of MBSL Spectra

Spectra of 1.0 M NaCl are shown from three different solutions on different days. The optical train had been moved and reassembled between each run (as a consequence of sharing equipment), and the spectra have been normalized to equal intensity to account for differing integration times.

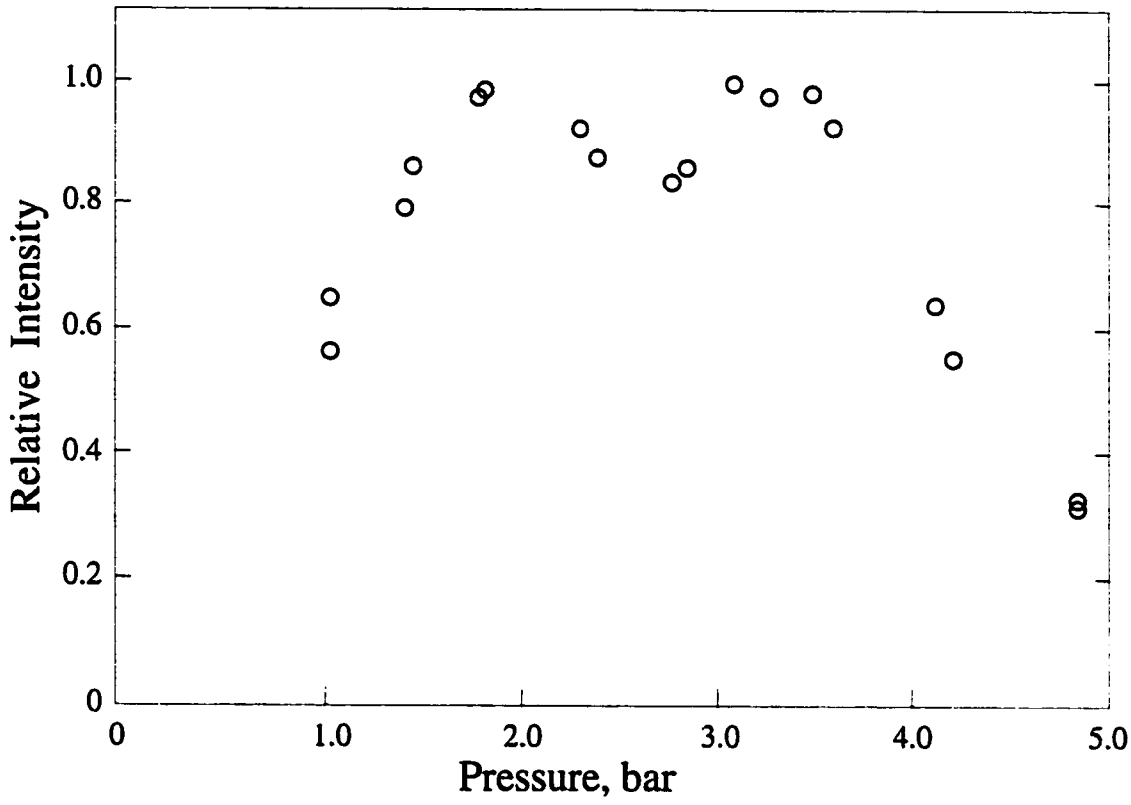

Figure 4-6. Effect of Static Pressure on MBSL

As static pressure is increased for cavitating DI water, MBSL intensity increases to a maximum at 3.4 bar after a local minimum at 2.7 bar. Beyond 3.4 bar, the static pressure competes with the acoustic pressure to grow effective cavitation bubbles.

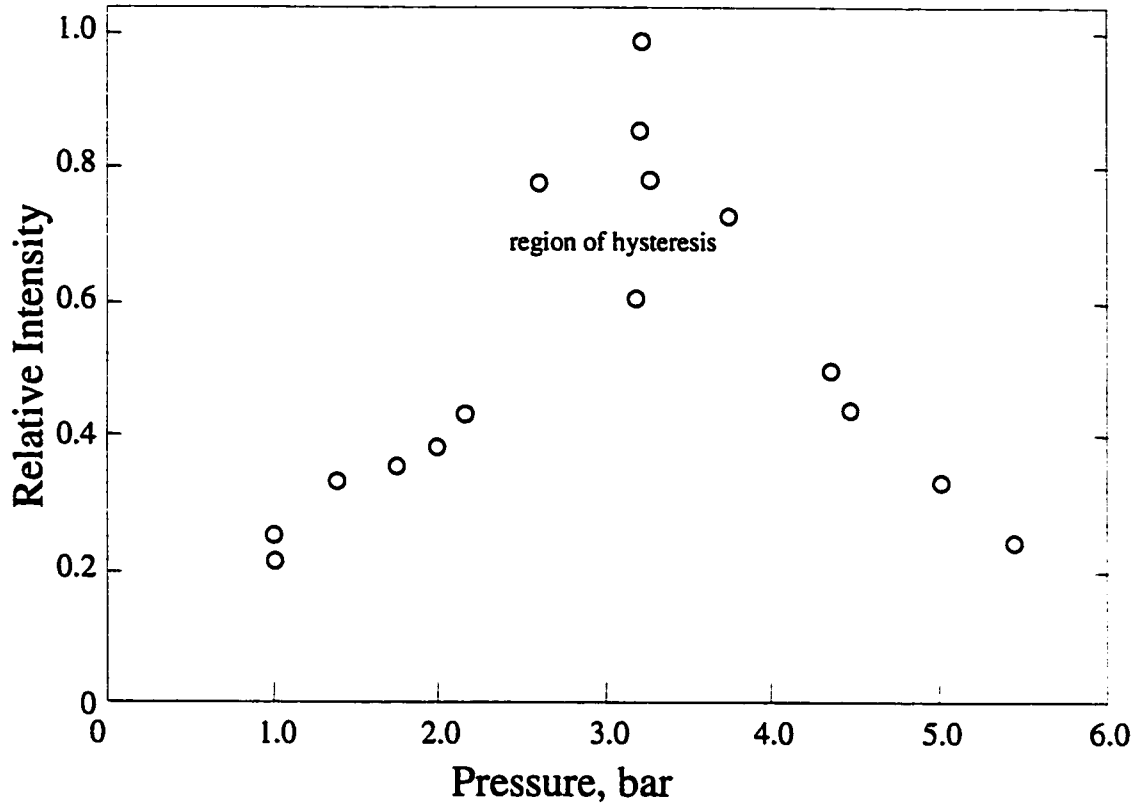

Figure 4-7. Static Pressure Hysteresis of NaCl Solution

A solution of 1.0 M NaCl shows hysteresis, maximized around 3.4 bar when the static pressure is cycled. The intensity at this pressure is dependent upon the pressure from which it was approached. The highest intensities resulted followed the highest previous pressures, and the lowest intensities resulting from the lowest previous pressures.

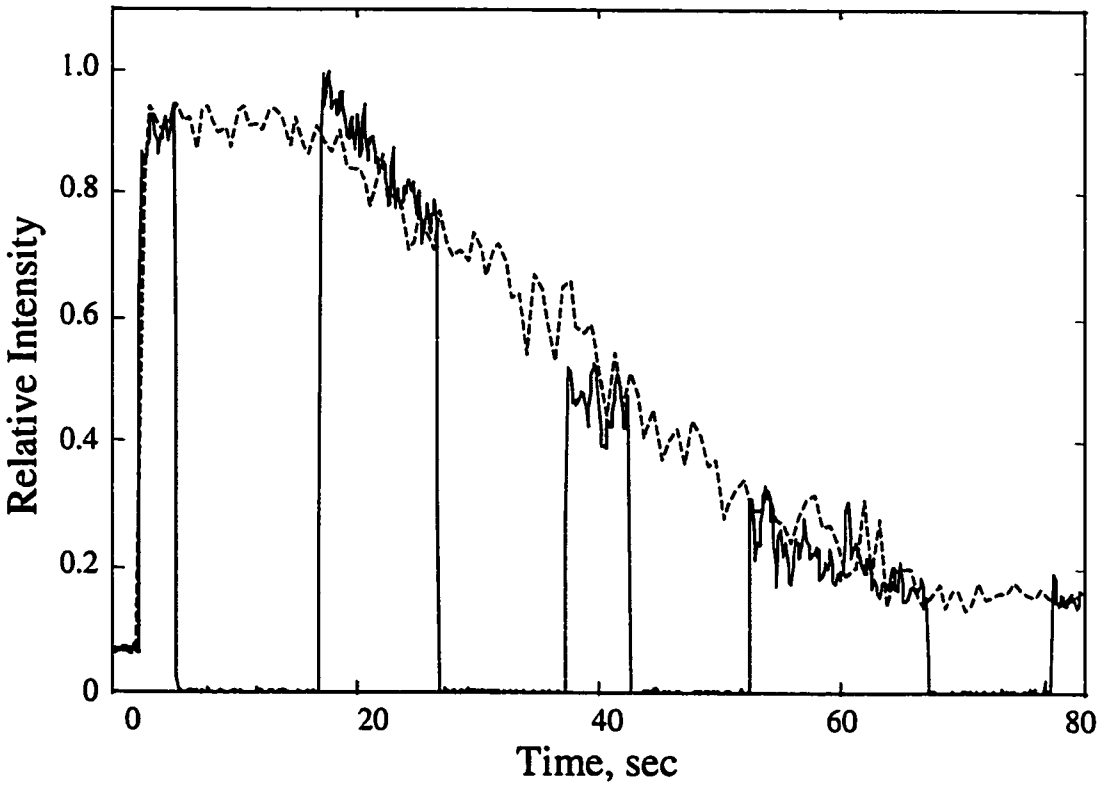

Figure 4-8. Effect of Static Pressure Jump on MBSL

The static pressure over a solution of 1.0 M NaCl was rapidly increased from 1 bar to 2.9 bar (t = 0) and held constant. SL was enhanced by an order of magnitude (solid line) for a period until equilibrium was reestablished (t = 70 sec). During interruptions of the acoustic pressure (dashed line), intensity immediately dropper to zero. Upon resumption of acoustic power, the intensity of SL nearly assumed its expected position on the curve.

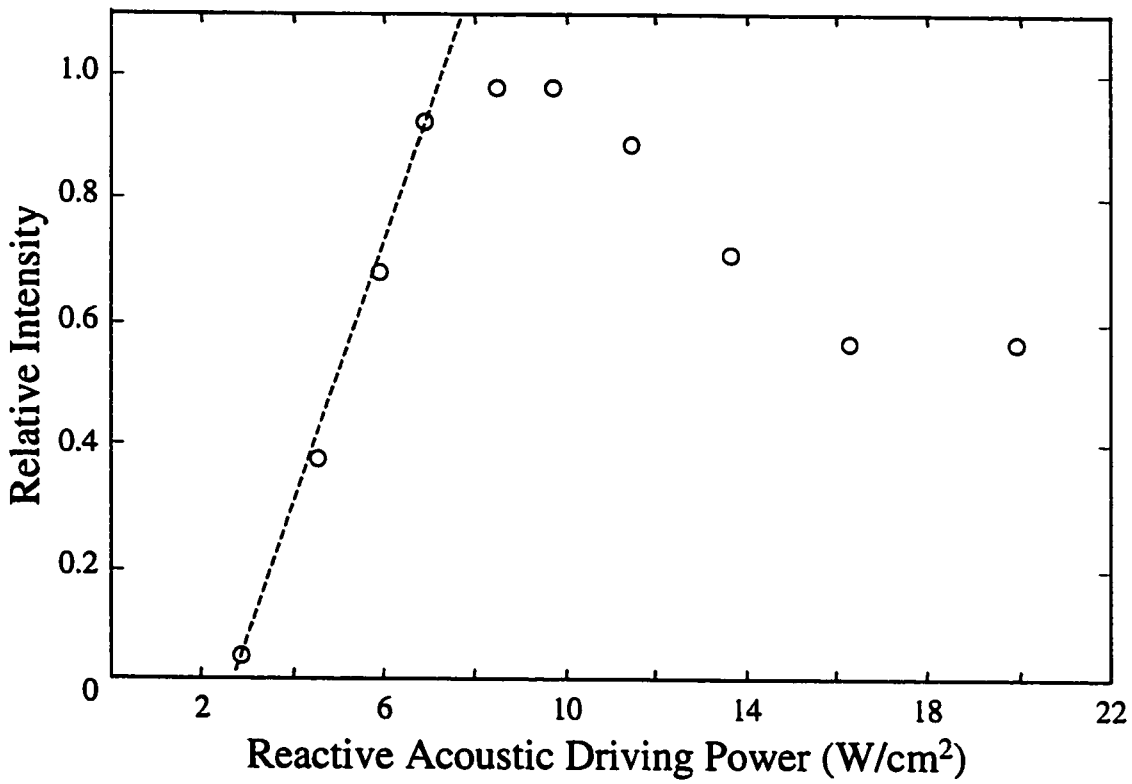

Figure 4-9. Effect of Acoustic Pressure on MBSL

As acoustic power applied to a 1.0 M NaCl solution is increased, MBSL increases linearly over the range of 4 to 10 W/cm^2. At higher powers the intensity asymptotically levels off as secondary effects become important.

Notes to Chapter 4

(1) Kuhns, D. W., Ph.D. Dissertation, University of Washington (1997).

Chapter 5

Salt Spectra and Quantification

In this chapter the use of sonoluminescence for quantitative analysis is presented, with possible applications for on-line process analysis. When alkali and alkaline earth salts are present with a noble gas in a sonoluminescing solution, the cations are reduced to neutral species, which then emit atomic spectral lines. The shape and intensity are determined by the concentrations of the salts, as well as other controllable parameters. Data is presented demonstrating that MBSL from alkali salt solutions can be modeled over a broad range of concentrations and used for quantitative analysis. Information from changes in shape and intensity of the emission lines over a wide range of salt concentrations can be used to construct Partial Least Squares (PLS) models. These models can be used to determine salt concentration from as low as parts per billion through saturation. This has possible applications in water hardness testing, chlor-alkali processing, and other situations where high salt concentration or contaminants interfere with traditional sensors.

Various mechanisms have been proposed to explain the origin of alkali MBSL emission lines.[1,2,3] It is generally accepted that the solvated ionic species are reduced by free electrons or radicals generated during cavitational collapse. During violent cavitation

events, gas and vapor molecules are rapidly heated under high pressure. Dissociation occurs, generating neutral, ionic, and radical species, as well as free electrons. Cations are then reduced in the layer surrounding the bubble. It is also possible that ionic species are introduced to the interior of a collapsing bubble through droplet injection or asymmetric collapse (Figure 5-1), where they are then reduced. During the neutralization event an excess of energy may be retained the by the atom. Excitation from the ground state is also possible. In either instance, the excited atom relaxes to the ground state through emission of a photon with energy characteristic to the atomic level of its origin. With sufficient concentration, this radiation is clearly observable above the background SL emission. Table 5-1 summarizes observed transitions for the Group I and Group II elements studied here, their excitation energies, and their characteristic wavelengths of emissions. The transitions with the lowest excitation energies (np $\rightarrow$ ns) are the brightest for these elements, and are often referred to as resonance transitions.

While studies of SL from salt solutions date back to the 1930s, reports of the effects have varied due to the use of various acoustic pressures, frequencies, cells, and dissolved gases.[1,2,3,4] For this reason, the results presented below may differ slightly from those obtained with different acoustic systems. However, the results are self-consistent, as they are with different sets of constant parameters.

A. Sodium

At moderate acoustic powers, emission from a solution 1.00 molar sodium chloride (Figure 5-2, dashed line) appears as a single, asymmetrically broadened peak. The maximum falls at 589.8 nm with a 2.1 nm peak width FWHM. The additional red-broadening is a real attribute of the doublet, likely caused by inelastic energy loss from collisions with the surrounding, condensed phase media. In the literature it has been suggested that the sodium D lines are broadened into one peak, the average position of which is shifted to longer wavelengths.[1] Figure 5-2 shows that this is not the case. Under the same conditions, emission from a solution of 5.00 molar sodium chloride (solid line) shows the doublet resolved into two peaks at 589.3 and 589.8 nm, and the broadening is greatly reduced. This profile could not be due to self-absorption, which would cause a dip to occur at the position of the low concentration maximum. The self-absorption zone is optically thin, as a compressed cavitation bubble is smaller than the characteristic wavelength of the emitted sodium radiation. All other sodium present in the system is ionized, and thus unable to absorb the atomic emission lines. To the contrary, the two peaks are nearly aligned with the doublet positions found in standard literature. At low concentrations, emission from the higher energy transition is suppressed, while emission from the lower energy transition is highly broadened and clearly dominant. At higher concentrations, this broadening is reduced, mostly from the red side, and the higher energy transition becomes dominant. While the resolved doublet has been reported with 2

molar solutions of NaCl,[3,5] no studies of changing MBSL spectral properties of sodium have been reported in the scientific literature to date.*

As shown in Figure 5-3 and Figure 5-4, the intensity of the sodium doublet increases in a logarithmic manner up to approximately 1.5 molar. It was previously reported that total MBSL intensity follows this same trend.[6] The doublet is dominated by the lower energy transition in this region. Above 1.5 molar the intensity decreases until it reaches a local minimum near 2.5 molar. At higher concentrations, the intensity increases again. At higher concentrations, the higher energy peak begins to emerge from the shoulder of the lower energy peak, increasing its relative intensity through the highest concentration studied. The anomalously low intensity at 5.33 molar resulted from the salt coming out of solution due to saturation from the reduced temperature.

Peak widths of the entire doublet between 0.5 and 5.33 molar are plotted in Figure 5-5. Peak width varies little up to 1.0 molar, with an average value of 2.0 ± 0.1 nm FWHM. The doublet begins to narrow around 1.0 molar. The width decreases sigmoidally with increasing concentration, reaching a minimum of 0.9 nm FWHM at 5.33 molar. The first derivative of this data reaches its maximum at 2.5 molar, the same concentration where the local minimum in peak height is observed.

The trends described above make this data well suited to analysis by PLS. Figure 5-6 shows a calibration curve for sodium chloride over the concentration range of 4.7 to 5.33 molar. Concentrations in this region near saturation are of particular interest as they

---

* A manuscript detailing this effect and its use for analytical purposes is in preparation and will be

are the most difficult to measure directly by other methods. Leave-one-out cross-validation was performed on a set of 5 spectra from each of 11 concentrations. The data was first autoscaled to remove intensity fluctuations and to equally include correlated changes on the wings of the sodium peaks. Using two latent variables, 98.9% of the predicted block variance was captured. The root mean square error of cross-validation (RMSEC) was 0.05 molar for this analysis. PLS can be used to model sodium concentration over a much broader range as well. Figure 5-7 shows a PLS calibration curve from .05 to 5.0 molar. Using 3 latent variables 99% of the predicted block variance was captured, and the RMSEC was 0.1 molar. A plot of the first two latent variables times their respective weight vectors (Figure 5-8) illustrates where the predictive information occurs in the analysis. The first factor mainly emphasizes peak width changes, while the second factor utilizes intensity changes of the emission peaks. At concentrations below 0.8 molar, sodium peak shape varies little and monovariate analysis of the monotonically increasing height is sufficient for quantification. The limit of detection is also of interest for such applications as water hardness testing. For sodium, the monovariate 3x S/N LOD was determined to be 100 ppb (4×10^{-6} M) when 100 x 30 second spectra were average.

---

submitted to *Talanta*. See Curriculum Vitae for further details.

B. Potassium

MBSL spectral characteristics from potassium chloride solutions are similar to those from sodium chloride solutions (Figure 5-9). At lower concentrations the potassium resonance doublet appears at 766.3/769.6 nm and is asymmetrically red-broadened. As concentration increases, overall intensity increases up to 1.5 molar, where it achieves maximum intensity (Figure 5-10). It reaches a local minimum at 3 molar and then increases again. Due to limited solubility 3.7 molar was the highest concentration studied. Unlike with the sodium doublet, the relative ratio of the potassium peaks remains nearly constant, though it does decrease slightly to a minimum at 2.07 molar. This is the same concentration at which the onset of peak narrowing occurs (Figure 5-11). Below this concentration, FWHM peak widths of the higher energy line measure 2.2 nm ± 0.1 nm. Above 2.07 molar, peak narrowing begins and increases through the highest concentration studied. As with sodium, most of the narrowing is due to a decrease in the red-wing broadening. After the onset of narrowing, the peak maxima occur at 766.2/769.5 nm.

The potassium spectra from Figure 5-9 are also well suited to PLS analysis. Figure 5-12 shows a calibration curve from 0.25 to 3.7 molar potassium chloride. Venetian blind cross-validation was used on a set of ten spectra at each concentration. Using 3 latent variables from the autoscaled data, 97.9% of the predicted block variance was captured. The RMSEC was 0.2 molar for this analysis. As with sodium, more accurate analyses can be made with a greater number of spectra covering a narrower

concentration range. The limit of detection was determined for potassium chloride in the same manner as sodium chloride. The LOD at was 40 ppm (1 mM).

C. Calcium

While observing the effects of calcium chloride on MBSL in the region of the spectrum where sodium emission occurs, an unexpected phenomenon was discovered. Broad emission peaks were observed where no strong calcium transitions occur (Figure 5-13). These bands correspond to peaks found in flame photometry of the same solution. They have been identified as originating from the neutral calcium (I) hydroxide species (CaOH), which is generated during combustion, and apparently, cavitation. Atomic hydrogen or free electrons reduce Ca^{2+}, followed by or preceded by reduction with OH*. Extra thermal or collisional energy *E* leaves the resulting molecule in an electronically excited state.

$$Ca^{2+} + e^{-} + OH + E \rightarrow CaOH^{*} \qquad (9)$$

If the relative ratios of the peaks identified in Figure 5-13 can be used to infer the temperature of a sonoluminescing bubble, the temperature at the time of emission corresponds to approximately 3500 K.[7] This may be a lower bound, however, for at higher temperatures calcium (I) hydroxide breaks down.[8] Excitation for this emission may occur before the maximum temperature is achieved, or while the bubble is rapidly cooling during adiabatic expansion immediately following collapse. It is currently debated whether non-volatile or ionic species can enter a cavitating bubble at all.

Emissions from such species may originate from secondary reactions with excited species and free electrons either on a bubble's surface, or in the nearby bulk fluid. In such a case, no estimate of the bubble's interior temperature can be made. Quantification using the calcium (I) hydroxide bands was attempted at low concentrations. MBSL spectra from millimolar calcium chloride solutions are shown in Figure 5-14. The LOD for calcium was determined to be 250 ppm (6 mM).

The calcium resonance emission line occurs at 423 nm (Figure 5-15). Unfortunately, it falls outside the sensitive region of the Princeton Instruments CCD. Attempts at acquiring spectra with other spectrometers and photodetectors were moderately successful, but required inordinate amounts of time. The best spectra were obtained with the CCD detector, though integration times on the order of 30 to 60 minutes were required to obtain significant intensity. This hindrance could be overcome by the use of a back-thinned or image intensified CCD, both of which are sensitive down to the UV region. As the calcium resonance spectra were collected with a great expense of time (including tedious cosmic ray removal), the multitude required for multivariate analysis was not acquired. Quantification was performed for concentrations below 1.0 molar by measuring the peak height. This produced the nearly linear plot shown in Figure 5-16. The 3x S/N LOD was 1600 ppm (0.04 molar).

D. Effects of Second Salt

Sodium-Calcium. The effects of adding a second salt on the MBSL emission profiles of a first salt were also investigated. Parts per billion to parts per million concentrations of calcium are important in certain industrial processes, such as in the production of sodium hydroxide. In this process, sodium salt concentrations approach saturation, and sodium and calcium determinations are performed off-line. From the accuracy and precision of the high concentration sodium experiments above, it appears that MBSL may be a feasible method for on-line monitoring of sodium concentration. However, the LODs for calcium present more of a challenge. The highly broadened, strong emission of the sodium D lines overlap and mask the strongest emission bands from calcium (I) hydroxide. The less sensitive, less intense resonance line at 423 nm is the remaining option. However, in the presence of high sodium concentration, the intensity of this line is further diminished due to increased competition for reducing species at the liquid-bubble interface. Figure 5-17 shows spectra from 0.1 molar calcium chloride with and without the presence of 5.0 molar sodium chloride. The sensitivity of the method has been reduced to 3500 ppm (150 mM), an unacceptable level for the sodium hydroxide application.

An interesting application for this method exists for the reverse situation. Low sodium concentration in the presence of high calcium concentration is found in the production of calcium chloride flakes. Lab analysis is typically required for this measurement as well, requiring titration.[9] To explore this scenario, the concentration of sodium chloride was varied between 0.11 and 0.23 molar in 4.2 molar calcium chloride

solutions. This approximates the concentration range of interest for calcium chloride production. Sets of ten 30 second spectra were signal averaged to enhance the weak sodium signal. Figure 5-18 shows the sodium doublet on the shoulder of a much more intense calcium hydroxide band. Figure 5-19 shows a PLS calibration curve using block cross validation on the resulting data. Two latent variables were retained, capturing 96.2% of the predicted block variance. The RMSEC was 0.06 molar.

Sodium-Potassium. Mixed salt solutions were prepared with incremental amounts of potassium chloride and final sodium chloride concentrations of 1.00 molar. Figure 5-20 shows the sodium emission lines at various potassium chloride concentrations (120 micron slit width). A trend similar to that of simply adding more sodium chloride is evident. The higher energy line of the doublet emerges, though the overall peak intensity decreases with successively higher potassium concentrations. Next, sodium emission spectra from a series of sodium chloride solutions were taken, with and without 1.0 molar potassium chloride. The shape of each spectrum with potassium is similar to a sodium-only spectrum, but with lower intensity. By plotting the relative ratio of the blue to red peaks versus the doublet peak width, an estimate of the similarity between the two groups of spectra was made. Figure 5-21 shows the nearly linear results. This evidence suggests that cation competition at the air/liquid interface is responsible for the reduced intensity, while the shapes of the emission peaks are mainly governed by physical properties. PLS and PCR (Principal Component Regression) had little ability to discriminate between spectra of the pure salt solutions and those of the mixtures. When the potassium contaminated spectra were regressed against a PLS model made using pure

sodium spectra, sodium concentrations were predicted to be 0.4 ± 0.1 molar greater in concentration on average. The pure sodium spectra are plotted in Figure 5-22 along with the potassium contaminated spectra, located at concentration values predicted by the PLS model. Notice the lower intensities for the potassium contaminated spectra. By parameterizing the data into red and blue peak heights, peak width, and area under the curve, a complete separation of the two groups is possible using two principle components (Figure 5-23). This suggests the use of neural networks, which is beyond the scope of the analysis here. However, if emission line spectra from the second salt are available, simultaneous determination of both salts should be possible with a single PLS or PCR model.

When incremental amounts of sodium were added to potassium chloride solutions (final concentration of 1 molar), similar spectral changes were observed with the potassium emission lines (Figure 5-24). Overall intensity decreased and line narrowing occurred. In this case, peak narrowing occurred with the first addition of NaCl, even though narrowing of the potassium lines did not occur until 2.5 molar in the potassium-only case. Beyond 2 molar, no further reduction in intensity was observed, although peak narrowing continued. This is more clearly seen when the spectra are normalized (Figure 5-25). Not enough data was obtained from these solutions for chemometrics analysis.

E. Discussion.

Under a given set of conditions, changes in the spectral distribution of alkali emission lines can be used to determine their concentration in solution. The presence of a second salt decreases emission line intensity due to competition at the air/liquid interface of the cavitating bubbles. While a second salt also changes the spectral profiles of the emission lines in nearly the same manner as the pure salt, quantification can still be performed by including spectra of both analytes in the calibration model. Spectra affected by surface modifiers with no emission spectra may be identified with Principle Component Analysis (PCA). A requirement of this technique is the presence of a noble gas. For industrial processes, a side stream could be cooled, and slightly diluted if saturation is problematic, purged with argon, analyzed, and returned to the process after analysis. Advances in a process flow design is presented in Chapter VII.

Certain other parameters change the spectral characteristics of alkali emission during sonoluminescence. These include gas content, acoustic frequency, static pressure, cell acoustics, and the presence of highly reflective particulates.[10] Line shape, intensity and the overall SL intensity are affected. For this reason, it is necessary to control external parameters so that changes in signal are related only to changes in salt concentration. The affect of other anions has been reported previously,[11] and is not explored in further detail here.

Each SL spectrum results from a statistical average of emitting bubbles. By the nature of a cavitation field, individual bubbles experience the effects of varying acoustic pressure, phase, neighboring bubbles, and vapor and gas pressure. This results in

different bubble collapses over the population.[12] From this, a small subset of conditions are conducive to light emission. Increasing salt concentration reduces vapor pressure and bubble coalescence while increasing surface tension. This results in a smaller average bubble size, and creates a more homogenous size distribution. Lower vapor pressure and increased surface tension are also more favorable for energetic collapse and subsequent sonoluminescence. However, the behaviors of alkali emission lines do not follow these physical trends. For solutions of sodium chloride the minimum rate of bubble coalescence occurs at 0.9 molar,[13] which roughly corresponds to the onset of peak narrowing. However, at higher concentrations, coalescence remains constant while peak narrowing becomes more pronounced. Other properties such as viscosity and surface tension change monotonically, and do not correlate with the low concentration region where emission peak width is constant. The phase transition-like behavior of alkali emission peaks and the short emission time suggest that a non-classical phenomenon may be responsible for sonoluminescence.[14] The theory of a cooperative emission mechanism will be discussed in the following chapter.

Table 5-1. Relevant Group I and II Transitions.

D and S indicate double and single degeneracies of the atomic transitions. Values are from the CRC. [15]

	transition	upper energy level, Joules x 10^{-19}	emission wavelength, nm
Na	3p → 3s (D)	3.37	589.0/589.6
	3d → 3p (D)	5.80	818.3/819.5
K	4p → 4s (D)	2.59/2.58	766.5/769.9
Ca	4p → 4s (S)	4.70	422.7

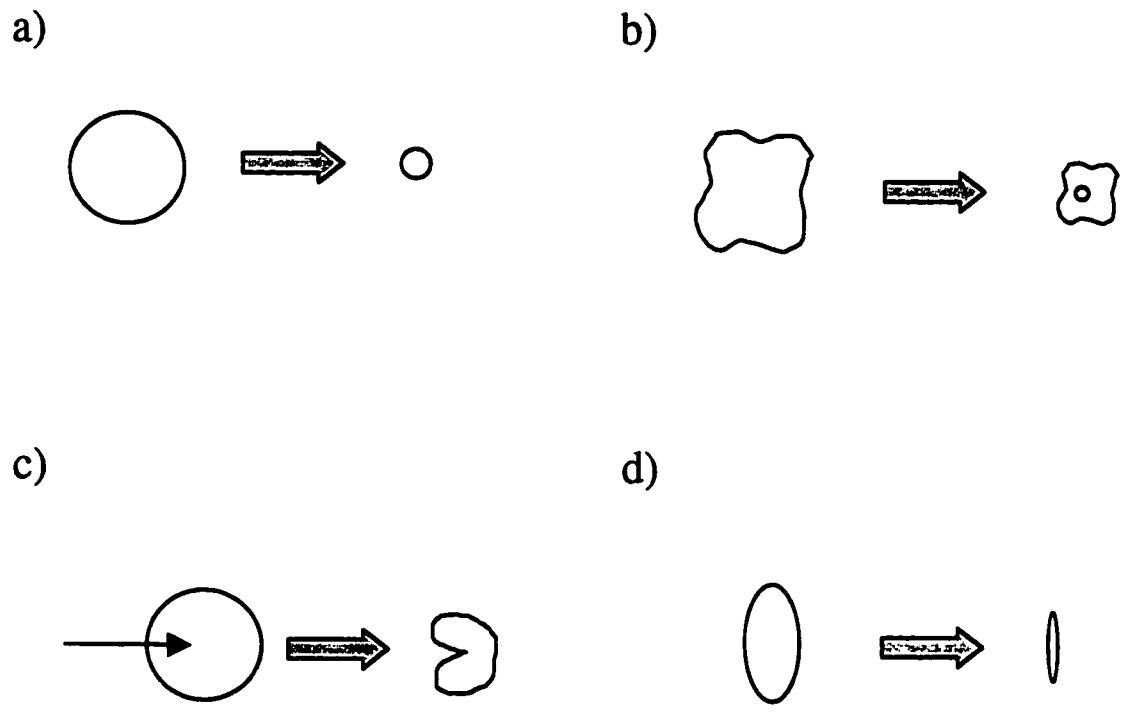

Figure 5-1. Types of Cavitation Collapse

Cavitation bubbles may collapse in a number of ways. Removed from all boundary effects, a bubble may theoretically collapse with perfect spherical symmetry (a). As is more likely the case, parametric instabilities lead to shape oscillations (b), disrupting spherical symmetry. This may lead to droplet injection into the collapsing interior. Liquid can also be injected into a bubble through jetting, which occurs from translation of the collapsing bubble (c). In a more exaggerated case, a bubble will collapse with a "pancake" shape (d).

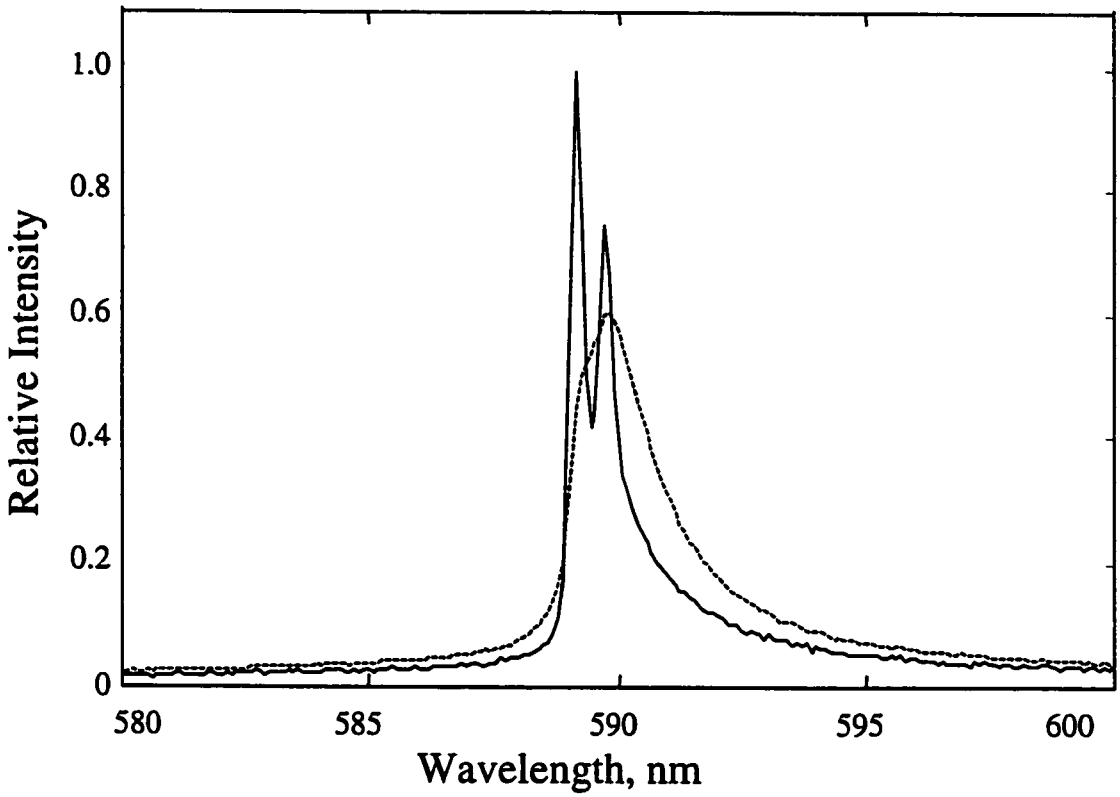

Figure 5-2. Typical Sodium MBSL Emission Lines

Doublet emissions from 1.0 M (dashed) and 5.0 M (solid) NaCl solution have different characteristics. At lower concentration, the doublet is more broadened, especially on the lower energy side. The higher concentration shows the doublet resolved into individual peaks, with less broadening.

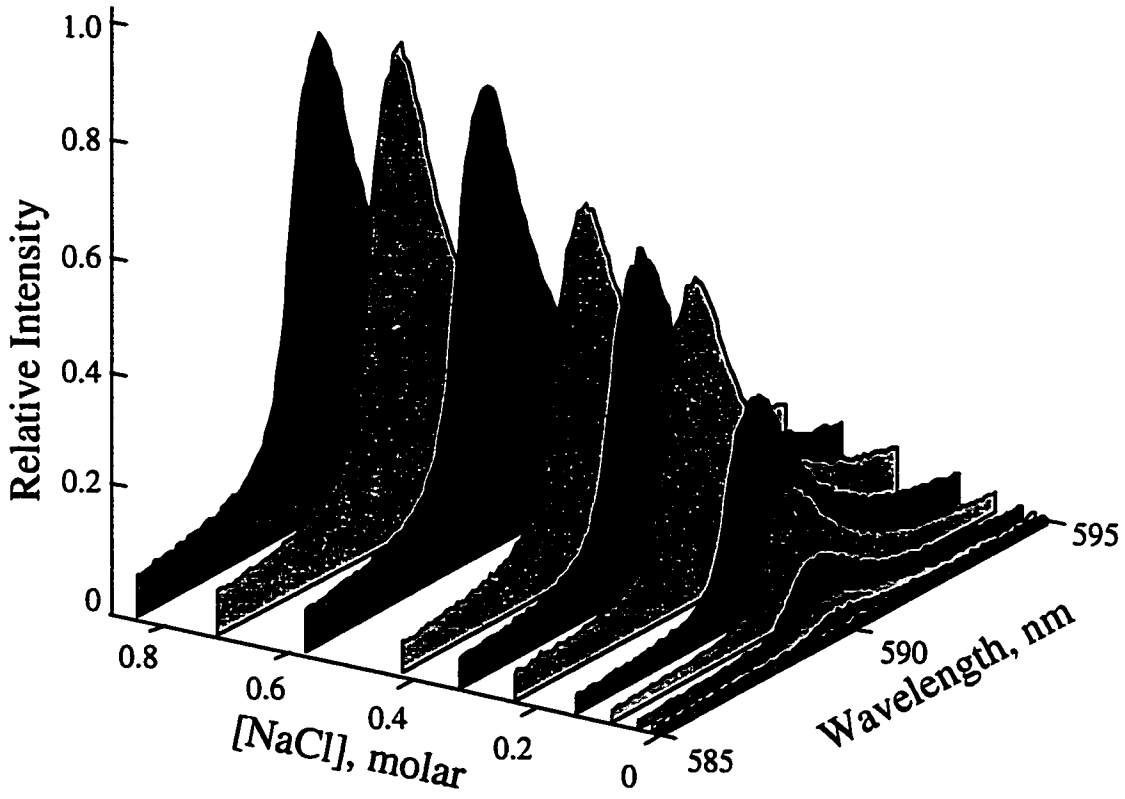

Figure 5-3. Sodium Doublet Emission Below 1 Molar

The general peak shapes of sodium change little with concentration below 1 molar. The intensity increases logarithmically.

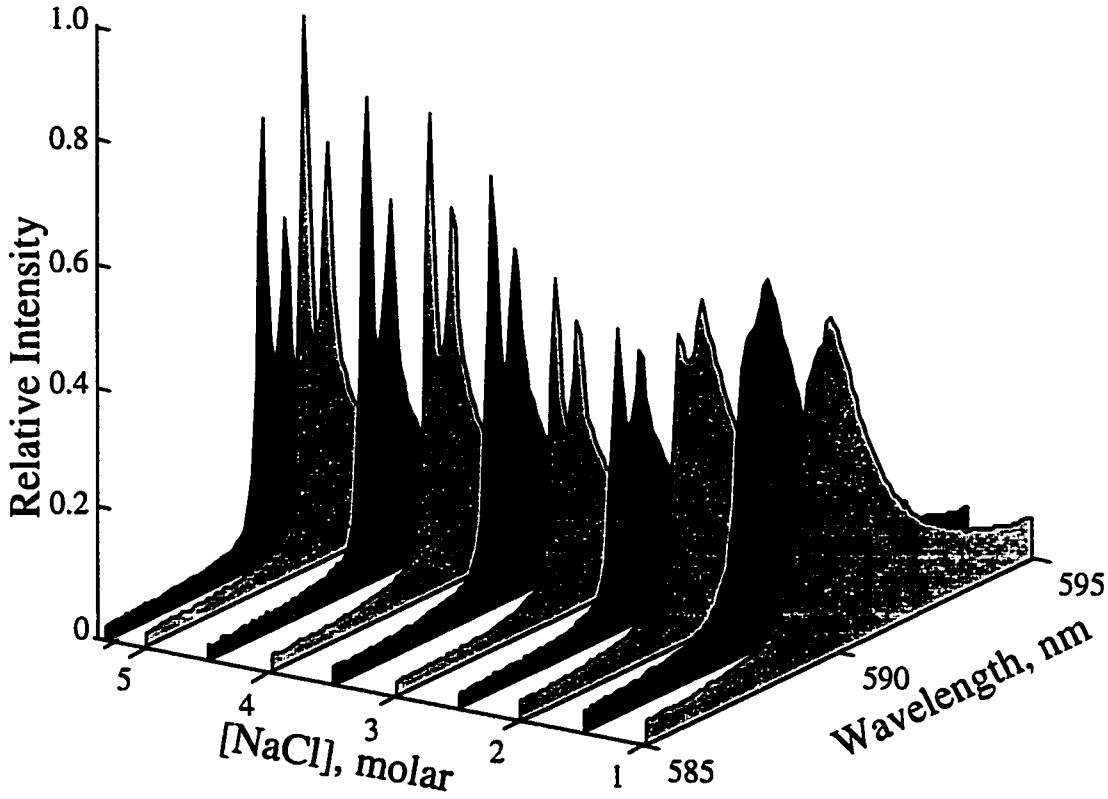

Figure 5-4. Sodium Doublet Emission Above 1 Molar

At increasingly higher concentrations, the sodium doublet becomes better resolved and the red-wing broadening decreases. The ratio of the high to low energy peaks increases through the highest concentration. The unexpectedly low concentration at 5.7 M occurred due to salting out of the solution at the reduced temperature (5 ° Celsius).

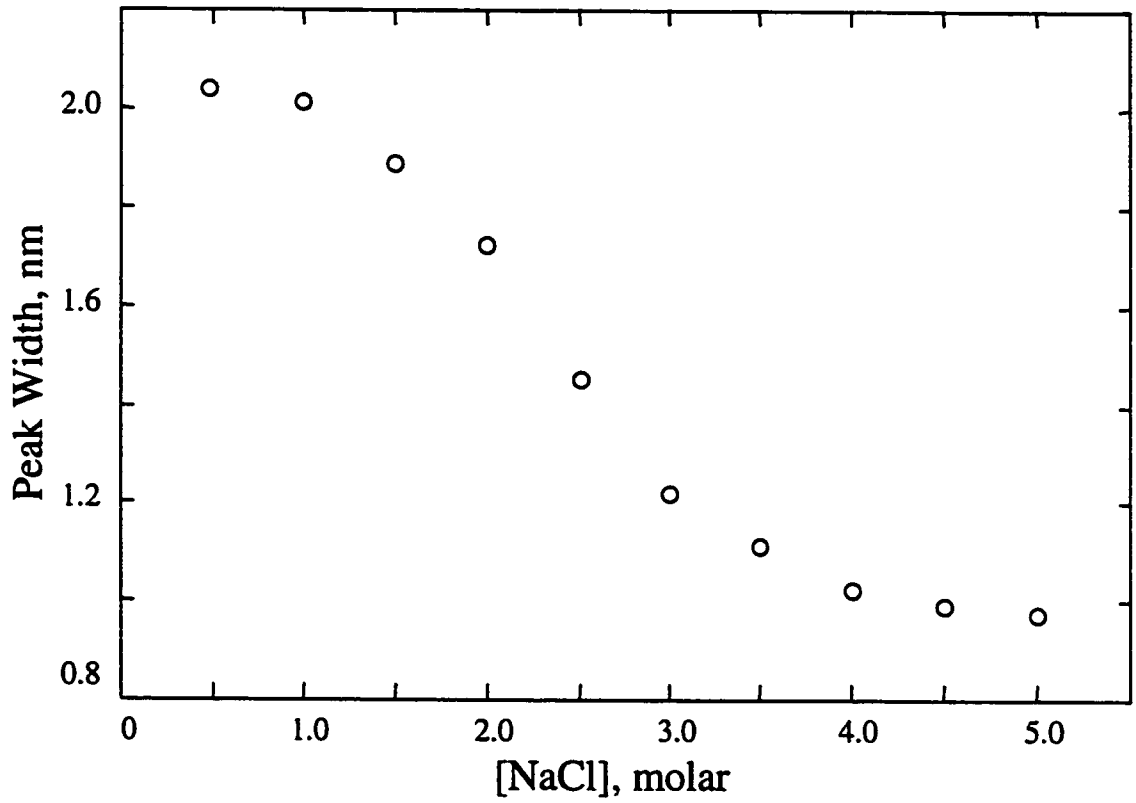

Figure 5-5. Sodium Peak Width vs. Concentration

The peak width of the sodium doublet remains nearly constant up to approximately 1 molar. At higher concentrations, the peak width decreases through saturation.

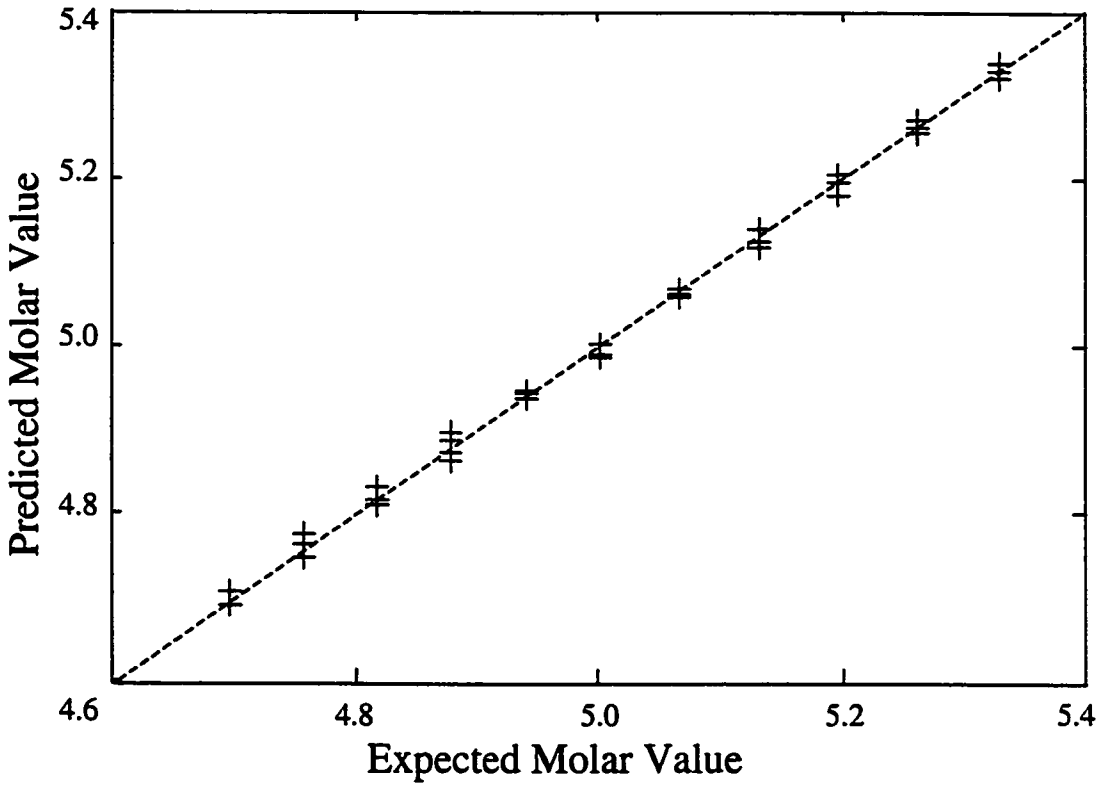

Figure 5-6. Sodium PLS Calibration Curve, Near Saturation

The resulting calibration curve was constructed using leave-one-out cross-validation Partial Least Squares analysis on a series of sodium chloride concentrations near saturation. Two latent variables captured 98.9% of the predicted block variance and the RMSEC was 0.05 molar.

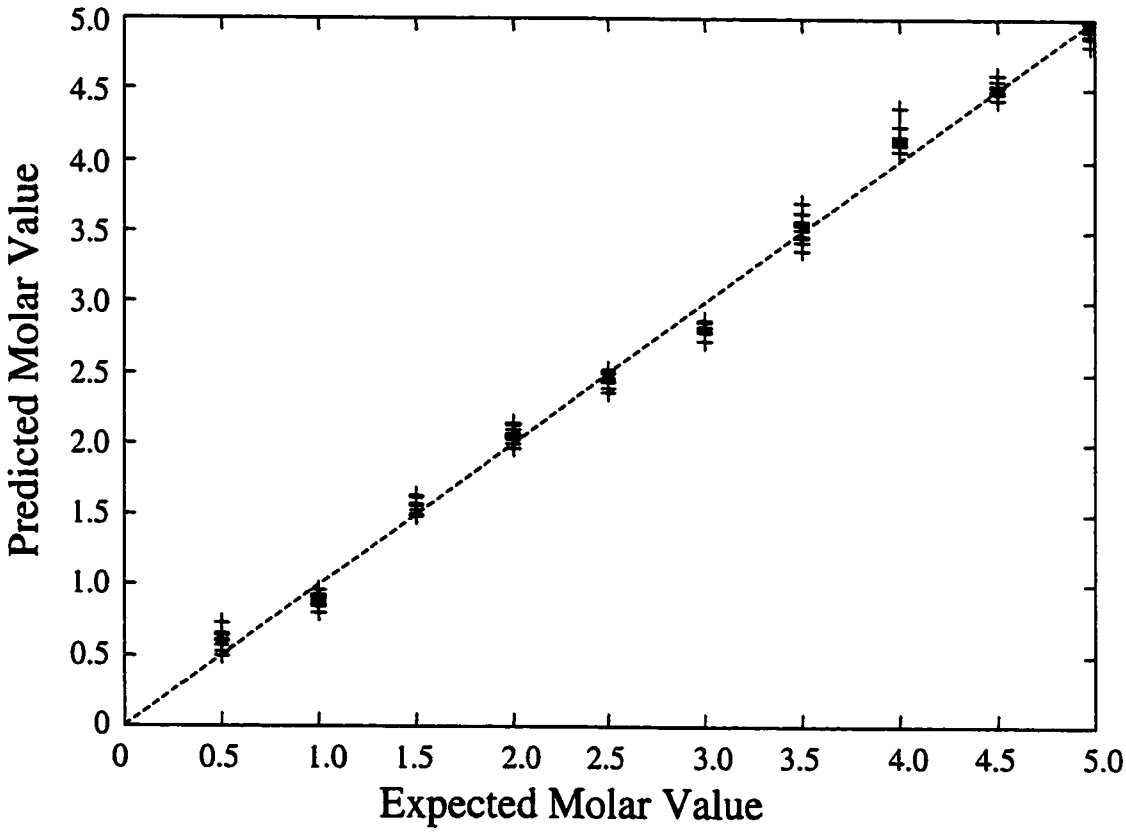

Figure 5-7. Sodium PLS Calibration Curve, Broad Concentration Range

The resulting calibration curve was constructed using leave-one-out cross-validation Partial Least Squares analysis on a broad concentration range of sodium chloride spectra. Using 3 latent variables 99% of the predicted block variance was captured, and the RMSEC was 0.1 molar.

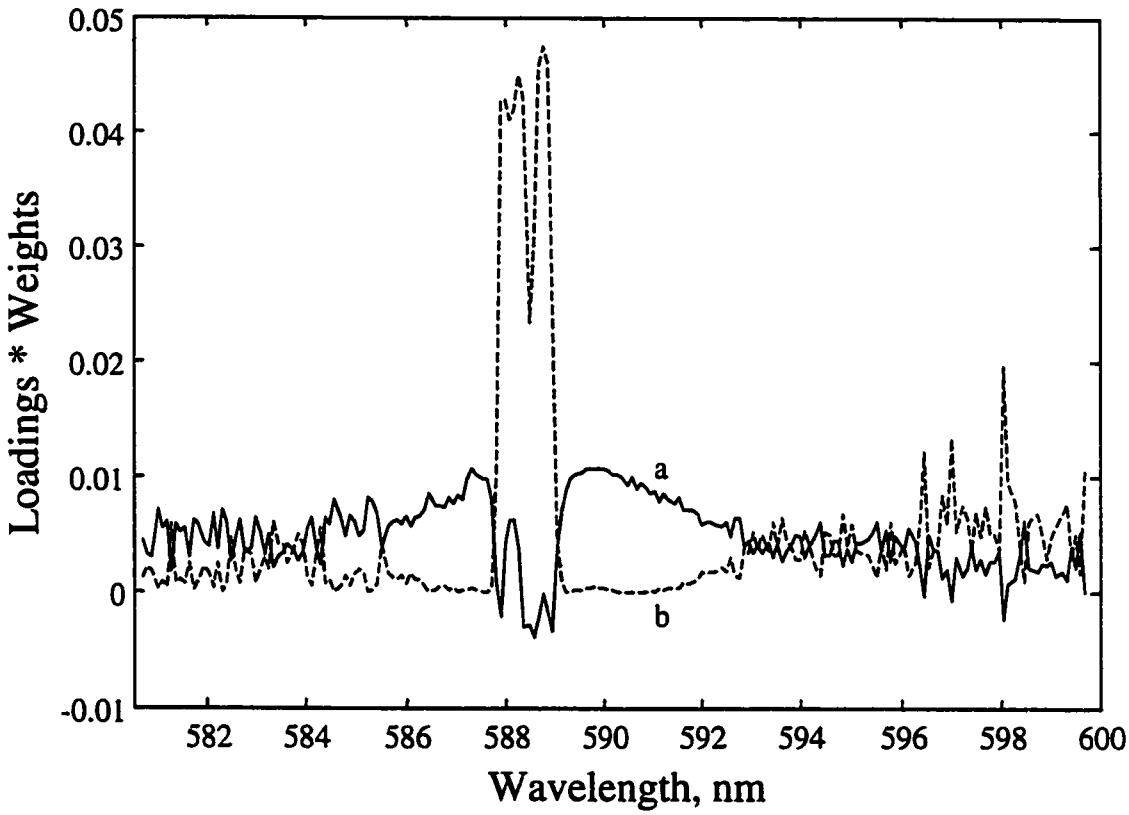

Figure 5-8. Product of PLS Loadings and Weights for NaCl Data

The products of the PLS loadings and their respective weight vectors from the analysis in Figure 5-7 show where the predictive information occurs in variables space (wavelength vector). The first factor (a) mainly emphasizes peak width changes, while the second factor (b) utilizes intensity changes of the emission peaks.

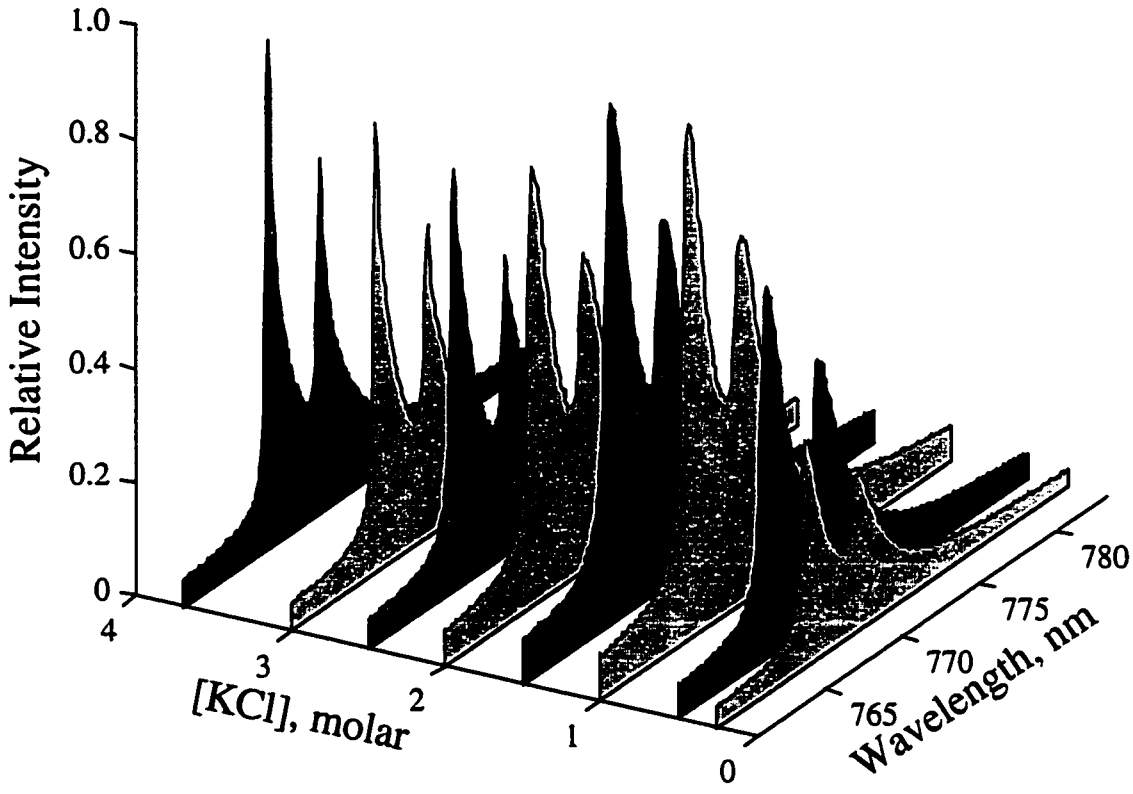

Figure 5-9. Typical Potassium MBSL Emission Lines

The shape of potassium emission peaks changes very little in shape up to 2 molar, and its intensity is nonmonotonic. Peak narrowing begins at 2.1 molar, near the local intensity minimum.

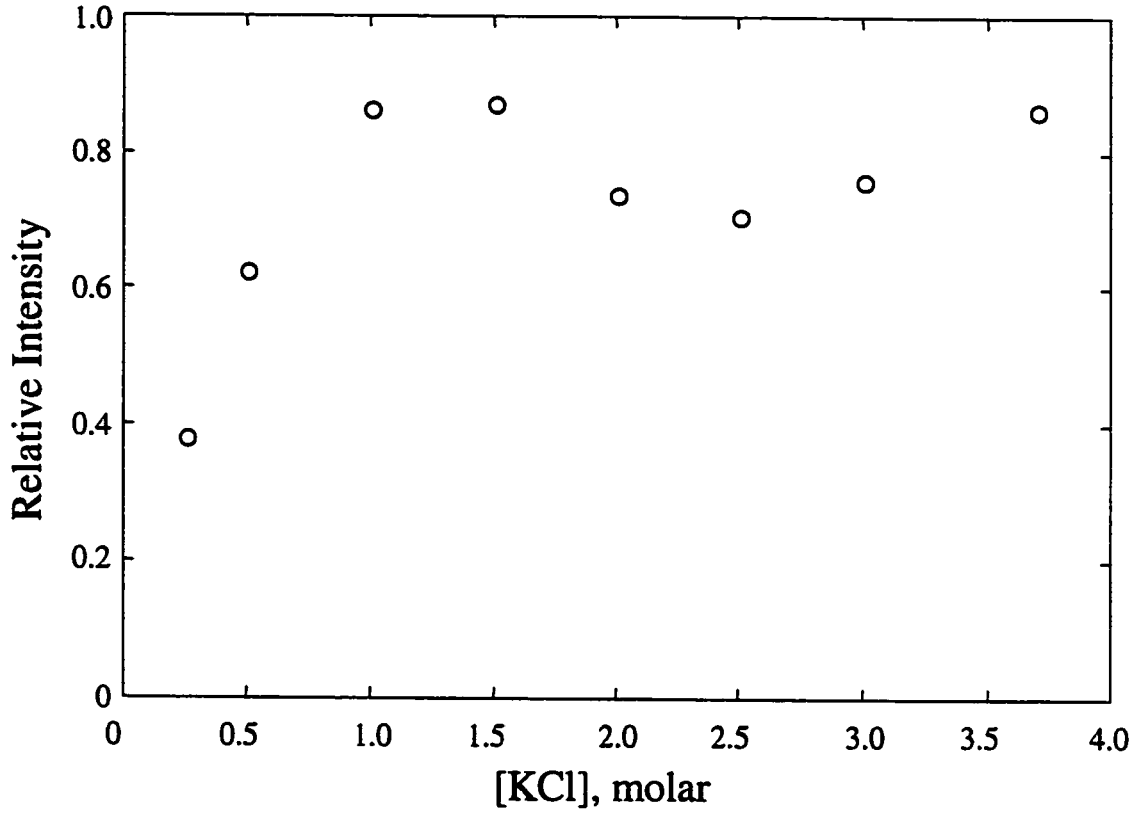

Figure 5-10. Potassium Peak Height vs. Concentration

The peak heights of the potassium doublet increase non-monotonically, reaching maxima at 1.5 and 3.7 molar, and a local minimum at 2.5 molar.

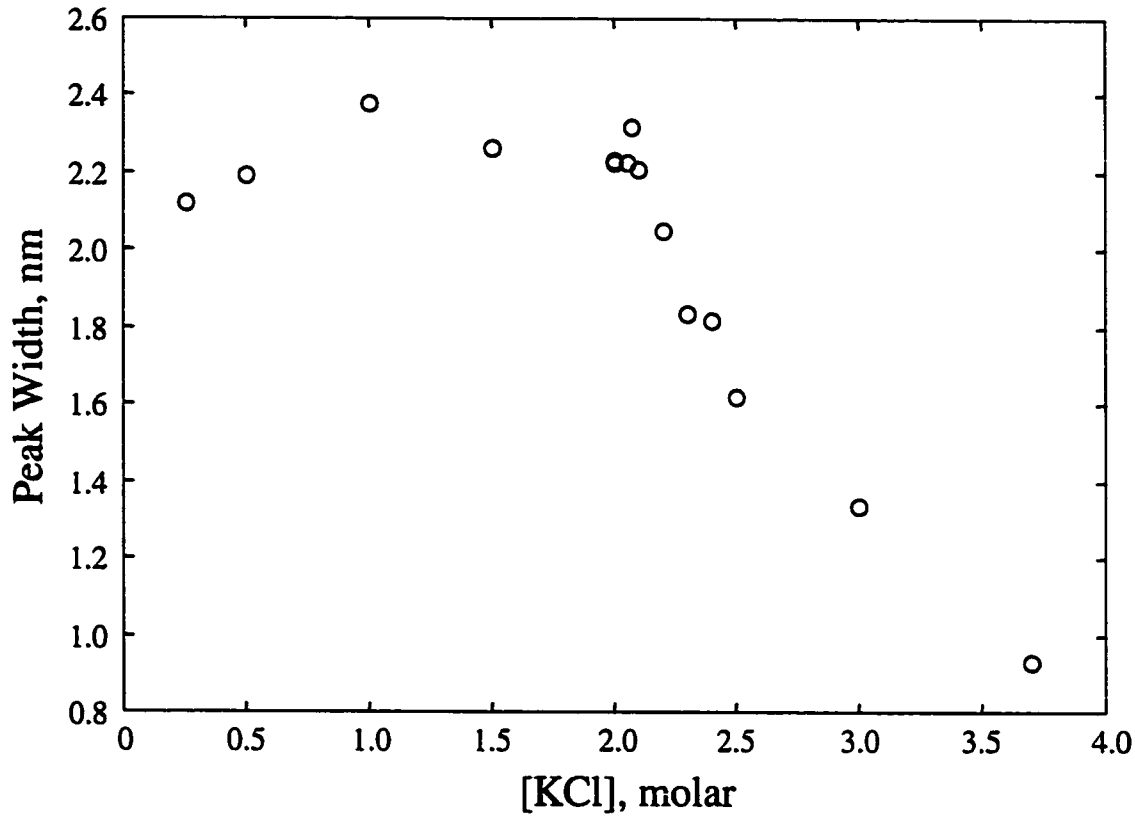

Figure 5-11. Potassium Peak Width vs. Concentration

Potassium peak width remains relatively constant for concentrations up to 2.1 molar, above which it decreases through saturation.

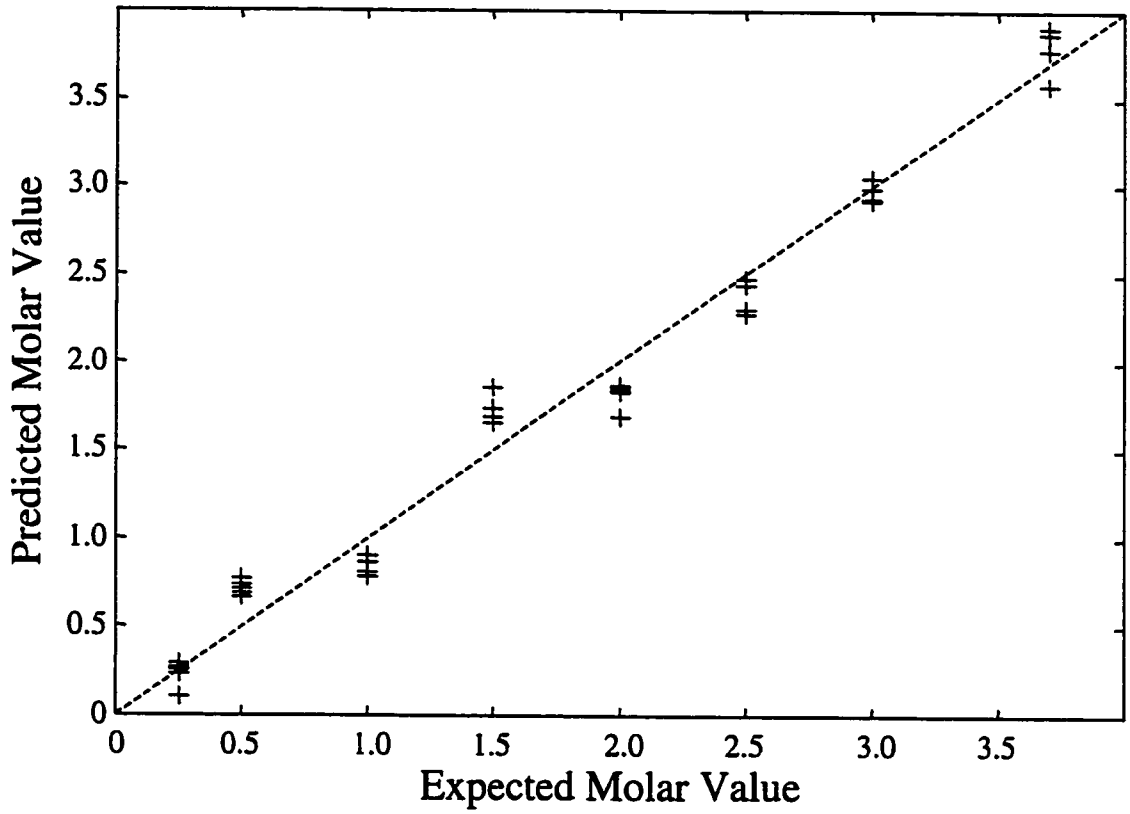

Figure 5-12. Potassium PLS Calibration Curve, Broad Concentration Range

The potassium PLS model is less accurate below 2 molar where normalized peak shapes are very similar. At higher concentrations, peak narrowing allows for better analysis.

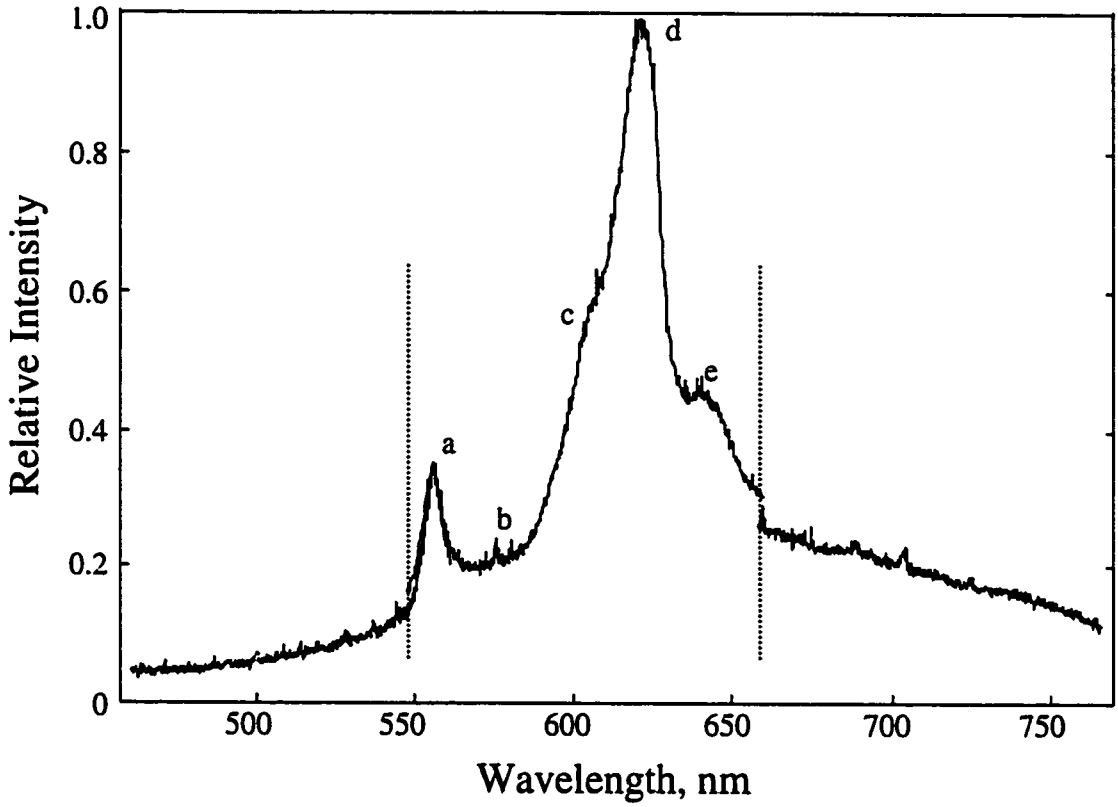

Figure 5-13. Calcium (I) Hydroxide Emission Bands

Cavitation of calcium chloride solutions produces emission from calcium (I) hydroxide, produced as a by-product. Emission bands are found at a) 554, b) 572, c) 604, d) 622, and e) 645 nm. This is the result of three spectra concatenated at the vertical dashed lines.

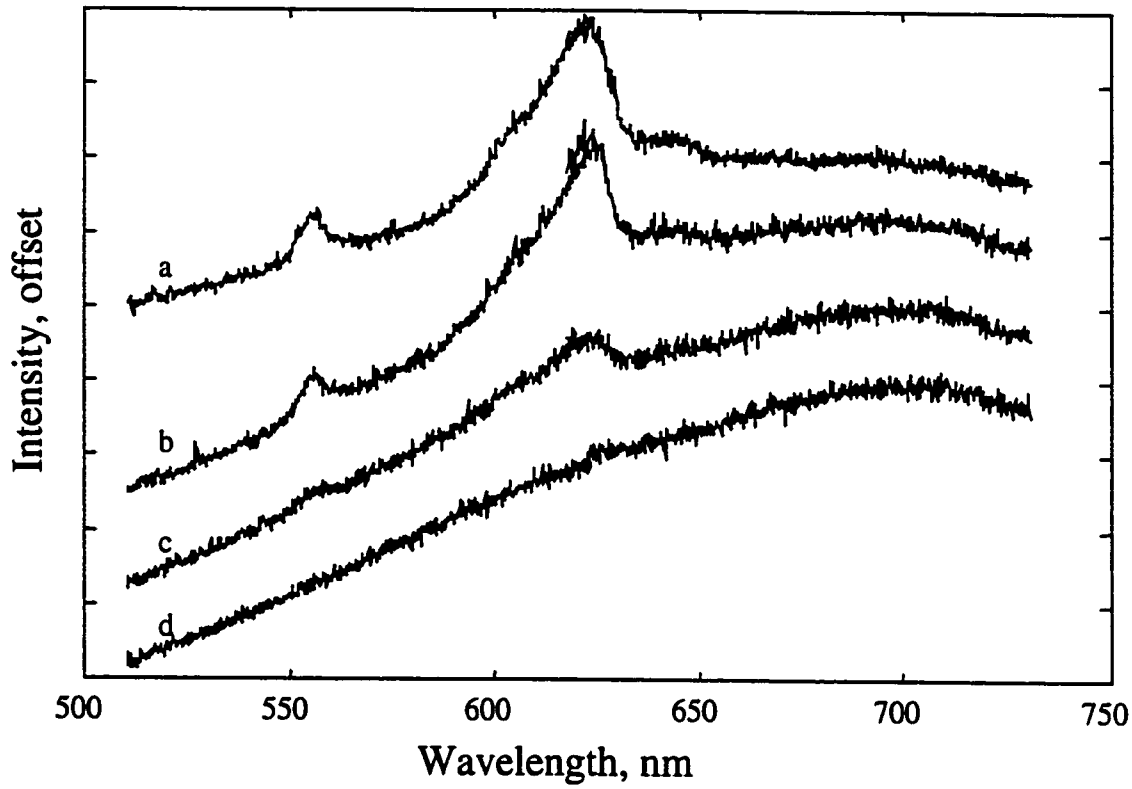

Figure 5-14. Low Concentration Calcium (I) Hydroxide Emission

Spectra of CaOH emission from the following concentrations of $CaCl_2$ solutions are shown: a) 250, b) 100, c) 25, and d) 2.5 mM.

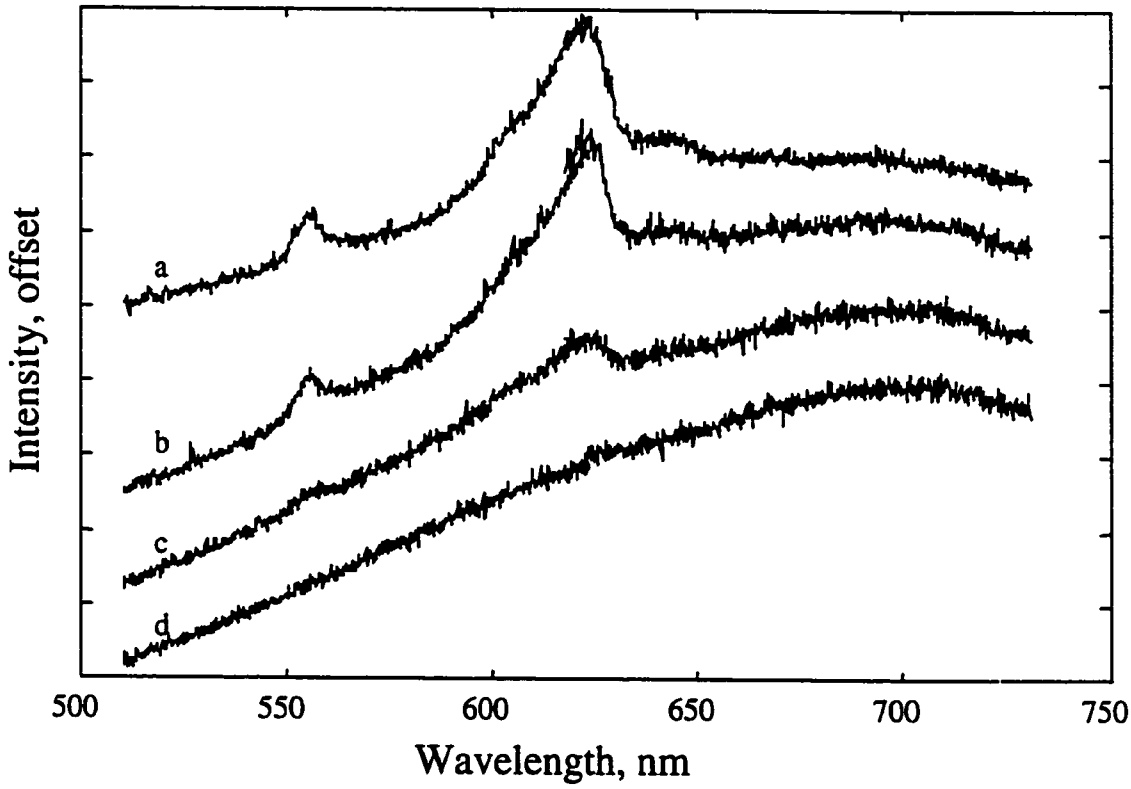

Figure 5-15. Calcium Resonance Emission Line

The resonance atomic emission line from calcium at 423 nm is shown from cavitation of a 0.8 M $CaCl_2$ solution.

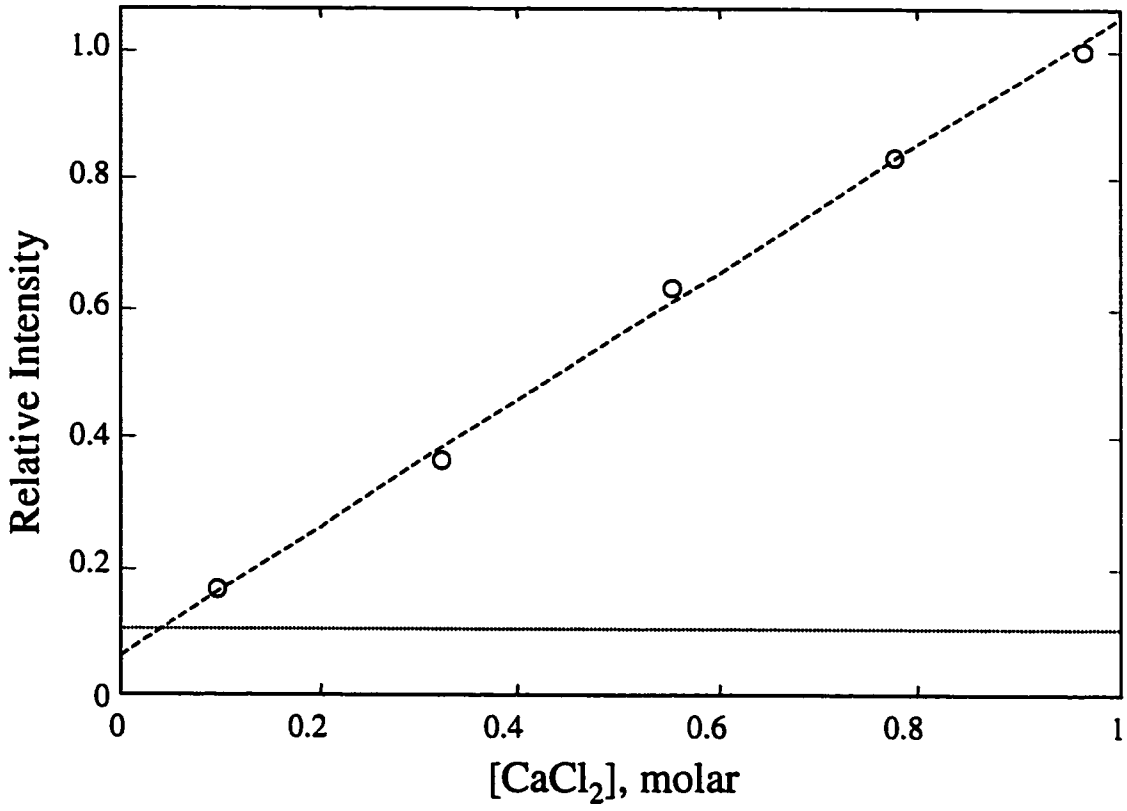

Figure 5-16. LOD Plot for Calcium

The 3x signal to noise detection limit (dotted line) for calcium was determined for the 423 nm emission line. The dashed line shows that the intensity of the peak is approximately linear in this region.

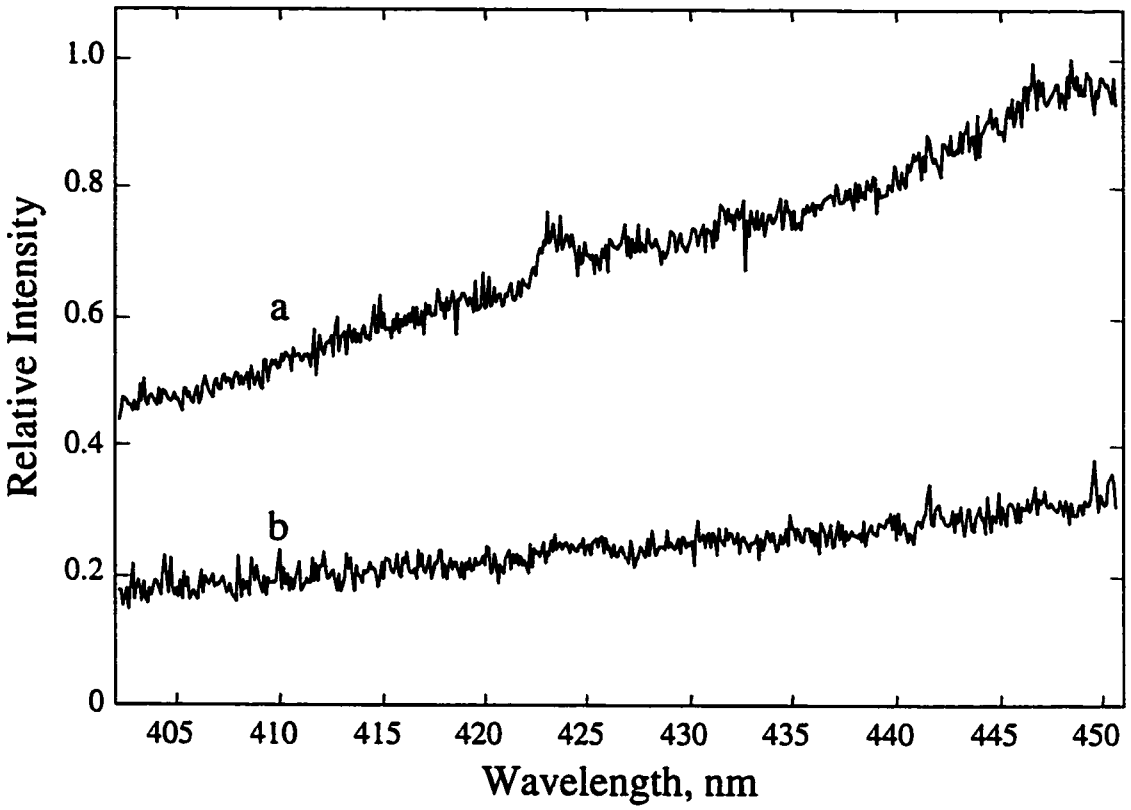

Figure 5-17. Effect of Sodium on Calcium Emission

Resonance emission from pure 0.1 M $CaCl_2$ (a) is compared to the same concentration in the presence of 5.0 M NaCl (b).

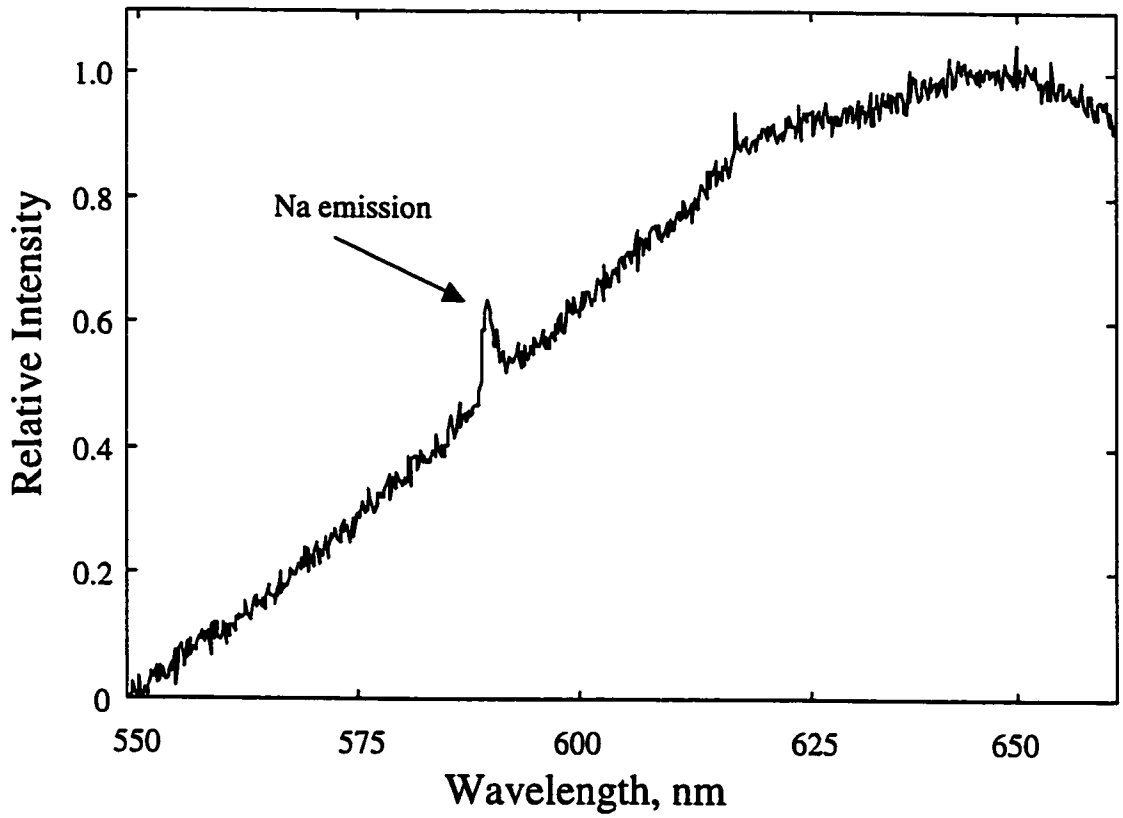

Figure 5-18. Sodium Emission on CaOH Band

The sodium emission doublet is shown on the shoulder of the calcium hydroxide band. This is the average of ten 30 second spectra. Sodium chloride and calcium chloride were 1% and 35% (w/w).

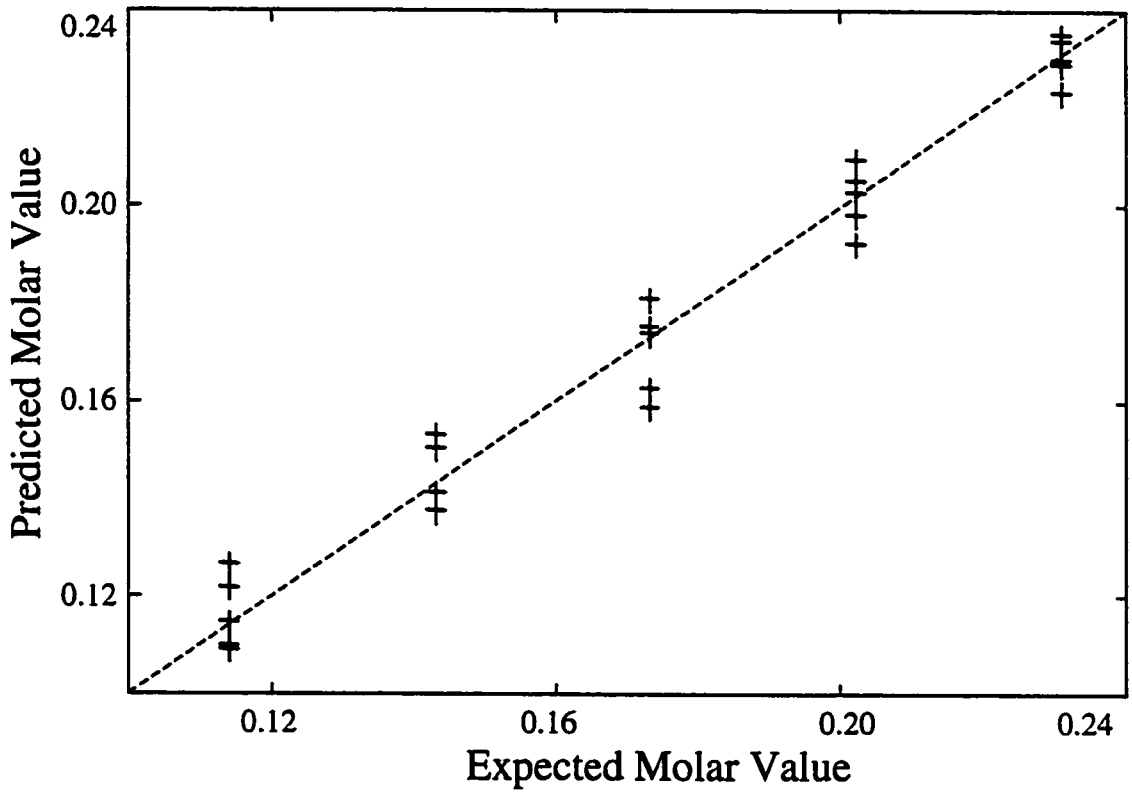

Figure 5-19. [NaCl] Prediction in High [$CaCl_2$]

The concentration of sodium chloride can be predicted in the presence of overlapping emission bands from calcium hydroxide. Calcium chloride was 35% by weight.

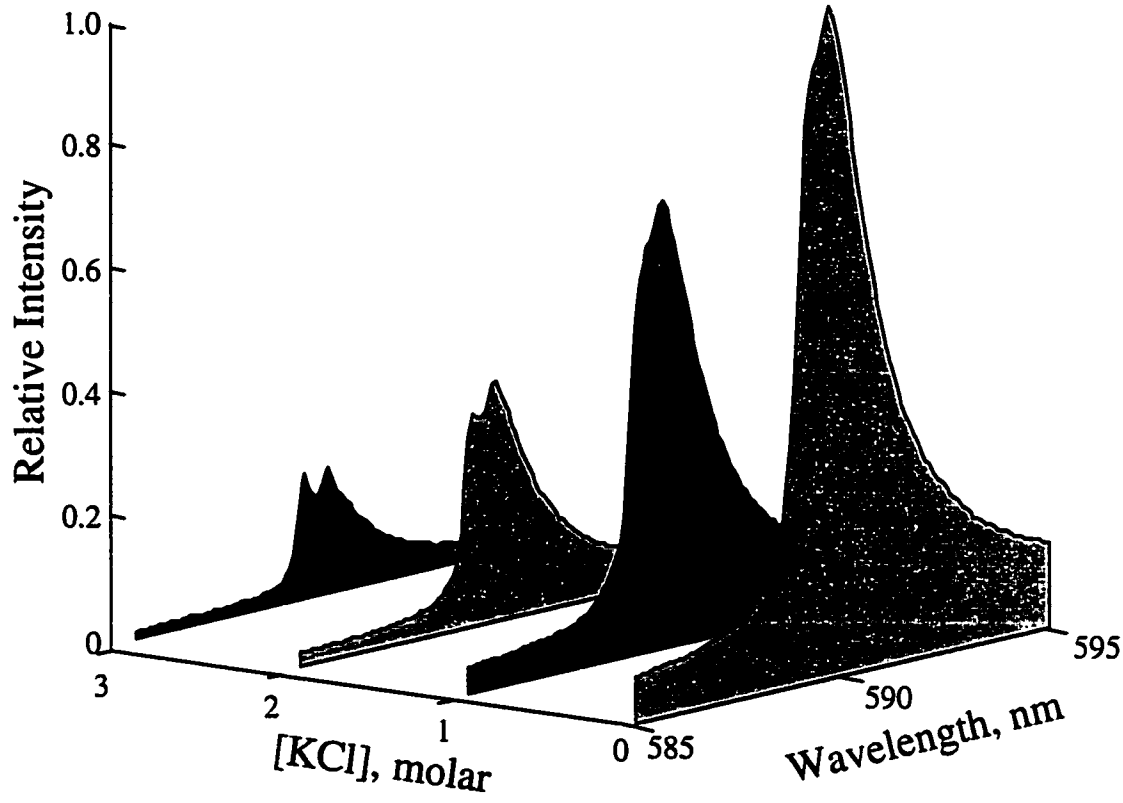

Figure 5-20. Effect of Contaminating Salt on Sodium Emission

Increasing concentrations of KCl cause emission from 1.0 M NaCl to decrease in intensity while the doublet becomes better resolved and narrows.

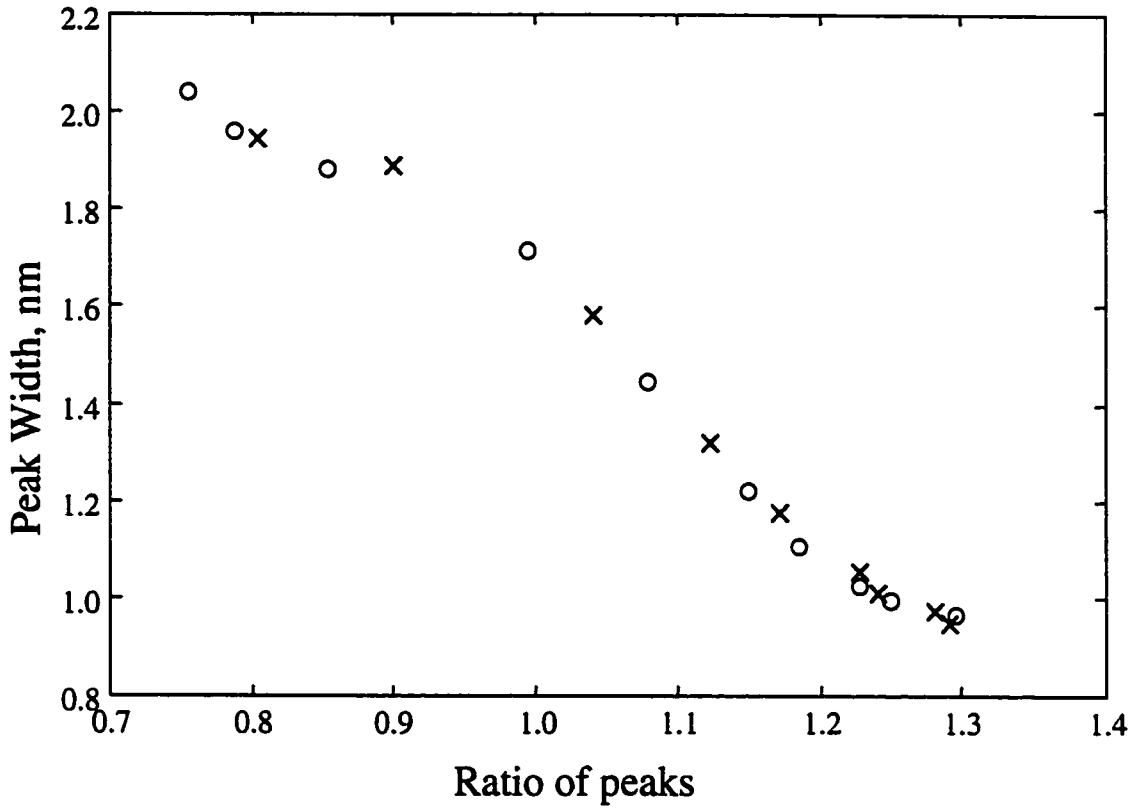

Figure 5-21. Comparison of Na Spectral Profiles with and without Contaminant

The relationship between the ratio of the higher to lower energy peaks of the sodium doublet and the peak width is explored for the spectra shown in Figure 5-22. Data from pure sodium solutions (o) and with 1.0 M KCl contaminant (x) are shown.

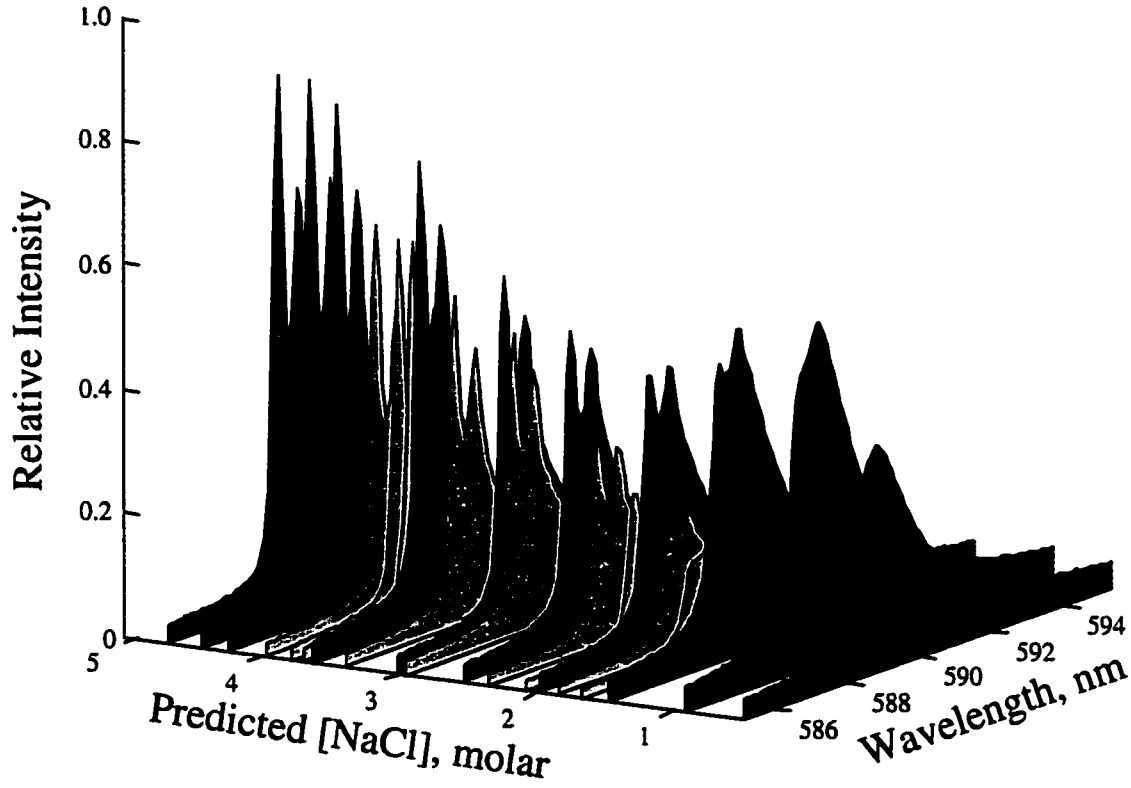

Figure 5-22. Pure Sodium Spectra with Potassium Contaminated Spectra

Sodium emission spectra from pure sodium (dark gray) are plotted along with spectra from sodium solutions contaminated with 1.0 molar potassium chloride (light gray). Concentration positions are determined by regression against a PLS model constructed using only pure sodium spectra. Actual versus predicted values are presented in Table 5-2 (next page).

Table 5-2. Pure and Contaminated Concentration Values

Actual sodium concentrations and values predicted by PLS model for a series of sodium chloride concentrations with and without 1.00 molar potassium chloride contaminant.

Actual sodium concentration	Predicted sodium concentration [pure]	Predicted sodium concentration [w/1.0 M KCl]
0.50	0.50	1.68
1.00	0.92	1.85
1.50	1.49	2.09
2.00	1.99	2.36
2.50	2.55	2.96
3.00	3.03	3.40
3.50	3.64	3.70
4.00	4.25	3.97
4.50	4.44	3.80
5.00	4.68	

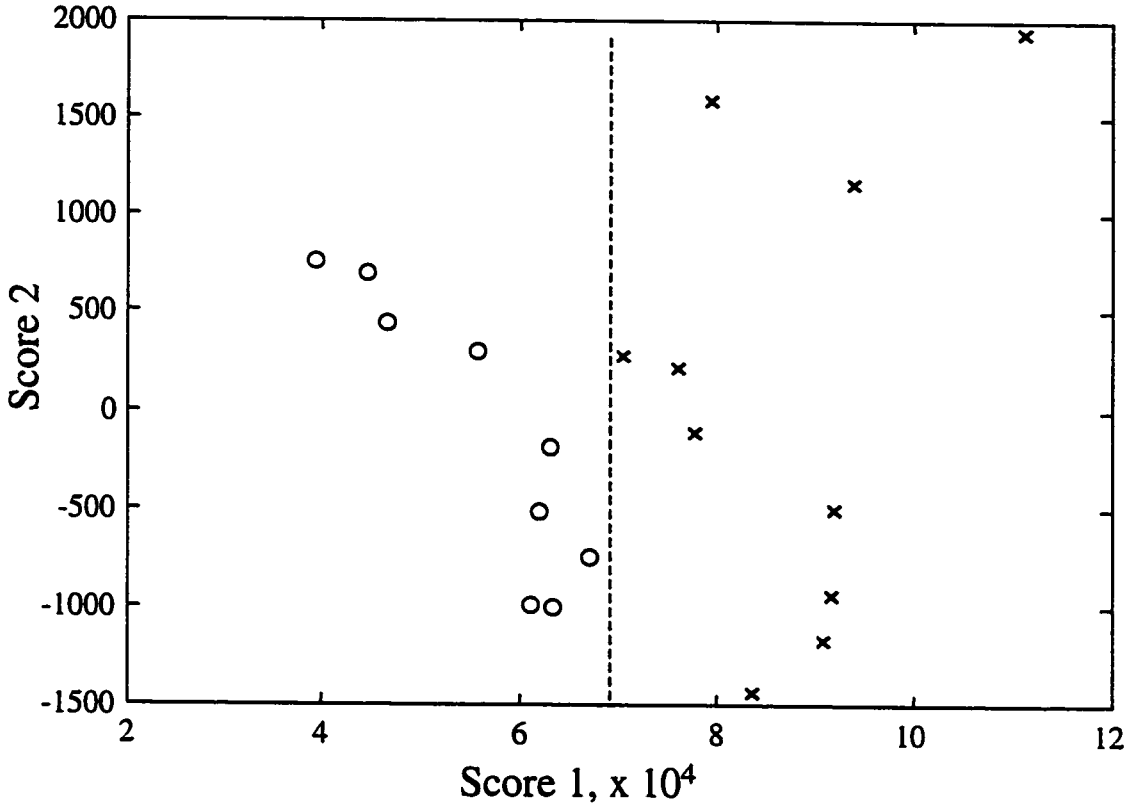

Figure 5-23. PCA Separation of Pure and Contaminated Sodium Spectra

Principle Component Analysis performed on the raw data in Figure 5-22 was able to separate the pure (o) sodium spectra from those contaminated with potassium (x) using two factors.

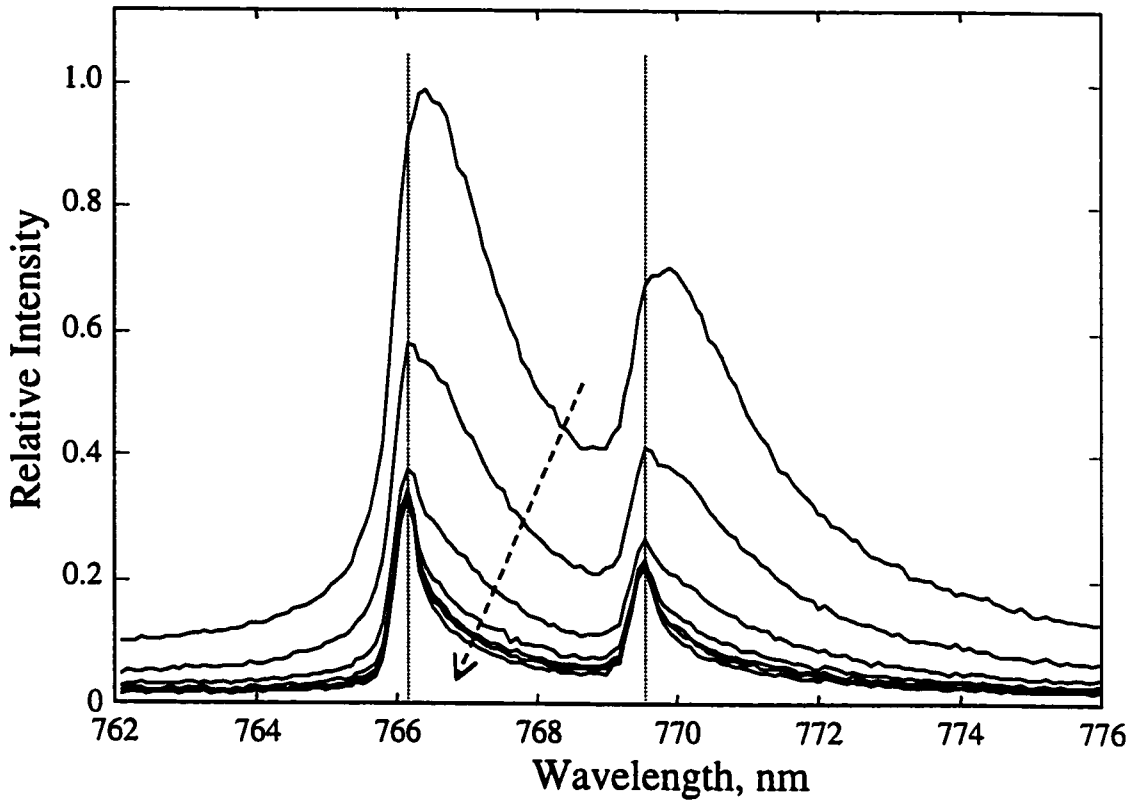

Figure 5-24. Potassium Emission Spectra with Sodium Contaminant

Potassium emission spectra from 1.0 M KCl solutions is shown with NaCl contaminants. NaCl concentration increases in the direction of the arrow according to the following molar concentrations: 0, 0.62, 1.22, 1.70, 2.16, 2.61, 3.06.

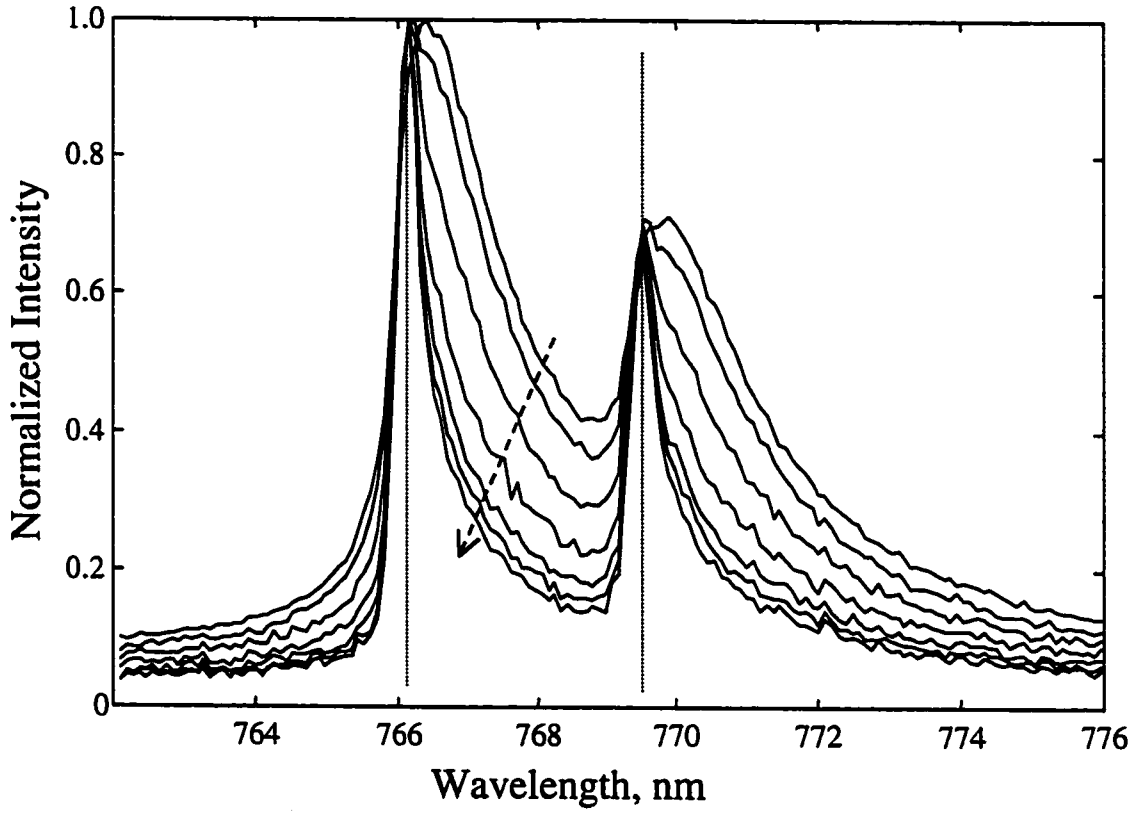

Figure 5-25. Normalized Potassium Emission Spectra with Sodium Contaminant

Same spectra as Figure 5-24, normalized. NaCl concentration increases in the direction of the arrow according to the following molar concentrations: 0, 0.62, 1.22, 1.70, 2.16, 2.61, 3.06.

Notes to Chapter 5

(1) Taylor, K. J.; Jarman, P. D. *Aust. J. Phys.* **23,** 319 (1970).

(2) Flint, E. B.; Suslick, K. S. *J. Phys. Chem.* **95,** 1484 (1991).

(3) Sehgal, C; Steer, R. P.; Sutherland, R. G.; Verrall, R. E. *J. Chem. Phys.* **70**, 2242 (1979).

(4) Lewschin, V. L.; Rschevkin, S. N. *Compt. Rend. Acad. Sci. URSS* **13**, 399 (1937).

(5) Heim, V. E. *Z. angew. Phys.* **12**, 423 (1960).

(6) Wall, M.; Ashokummar, M.; Tronson, R.; Grieser, F. *Ultrason. Sonochem.* **6**, 7 (1999).

(7) Parsons, M. L.; McElfresh, P. M. *Flame Spectroscopy: atlas of spectral lines* (IFI/Plenum: New York, 1971) p. 47.

(8) Skoog, D. A.; Leary, J. J. *Instrumental Analysis*, 4th Ed. (Saunders College Publishing: Forth Worth, 1992) p. 205.

(9) Franson, M. A. *Standard Methods for the Examination of Water and Wastewater*, 14th Ed. (American Public Health Ass.: Washington, 1976) Part 306.

(10) Brodsky, A. M.; Burgess, L. W.; Robinson, A. R., accepted for publication in *Ultrasonics* as of September 2000 (issue to be determined).

(11) Kuhns, D. W., Ph.D. Dissertation, University of Washington (1997).

(12) Parlitz, U.; Mettin, R.; Luther, S.; Akhatov, I.; Voss, M.; Lauterborn, W. *Phil. Trans. Roy. Soc. Lond. Series A* **357**, 313 (1999).

(13) Craig, V.; Ninham, B.; Pashley, R. *Nature* **364**, 317 (1993).

(14) Brodsky, A. M. *Mod. Phys. Lett. B* **13**, 1019 (1999).

(15) **CRC Handbook of Chemisrty and Physics**, 63rd Ed., eds. Weast, R. C.; Astle, M. J. (CRC Press, Inc., Florida, 1982) p. E-294.

Chapter 6

Advances in Sonoluminescence Theory

A new period of sonoluminescence research started about a decade ago when a narrow range of conditions was established allowing stable, reproducible sonoluminescence to be produced from an acoustically levitated single bubble (SBSL).1 This has allowed the detailed study of single cavitation bubbles, nearly isolated from boundary effects. Physicists have undertaken the vast majority of experiments, most of whom believe that SL emission results from Bremsstrahlung radiation from a weakly ionized plasma. In order to account for the creation of plasma conditions in the tight confines of a bubble collapsing to it van der Waals hard-core radius, it has been proposed that a spherically converging shock wave isolates the plasma from the surrounding cool water.[2,3] A number of other more exotic theories have been proposed as well (Chapter II, Section C), none of which explain all the intricacies of SL. However, the less commonly considered theory of cooperative emission effects[4, 5,6] can explain many of the experimental observations presented in this dissertation.

While studying MBSL spectra from alkali solutions, non-linearities and behaviors resembling threshold effects were observed. Atomic emission lines arising from cavitation of sodium chloride and potassium chloride solutions were studied over a range

of acoustic powers and concentrations to investigate these effects. Threshold square-root dependencies of peak width and intensity of these lines are consistent with the theory of cooperative, many-body emission of sonoluminescence. The results suggest that sonoluminescence may have been the first instance of experimentally produced collective optical emission effects, observed almost three decades prior to the first optical laser.

The permissible conditions for SBSL were found to exhibit threshold behaviors of important parameters such as bubble size, acoustic driving pressure, and dissolved gas content. In perhaps the most striking example, sonoluminescence suddenly emerges from a levitated bubble after a threshold value of acoustic driving pressure is achieved. At this point the dynamics of the radial bubble motion change qualitatively.[7,8,9] This behavior resembles dynamic phase transitions in non-equilibrium, many-body quantum systems, such as lasers. SBSL also ceases to exist above an upper driving pressure limit due to parametric instabilities in the radial motion of the bubble. Another striking aspect of SBSL is the short duration of emission, which lacks an afterglow. The duration of these flashes, releasing approximately 1 million photons per burst, has been measured at 40–350 ps long for SBSL.[10] This is significantly shorter than the characteristic emission times of both spontaneous quantum dipole-dipole transitions and electron Bremsstrahlung in weekly ionized plasmas. It has been reported that individual light emission events in MBSL occur on the same time scale as in SBSL,11 implying that only quantitative differences exist between the two.

In several articles by Brodsky[5,6,12,13] and Mohanty[4,14,15] it has been proposed that the short duration of light emission from SL results from many-body collective, non-

equilibrium quantum processes. Emission occurs from the relaxation of a population inversion in a bubble system. The species are excited either thermally or through a rapid dipole reorientation on the bubble's surface. The duration of collective emission τcoll can be orders of magnitude shorter than individual spontaneous emission τind, according to the relation

$$\tau_{coll} = \frac{\tau_{ind}}{N} \tag{10}$$

where N is the number of collectively excited species. Collective processes in SL can be connected with two types of effects. First, due to the phase correlation between electronically excited species, the effective dipole transition moment can increase greatly, reducing the emission time. Such phase correlation is observed in Dicke superluminescence.[16] The second effect is stimulated isotropic emission, which is observed in multi-scattering gain media.[17,18] Both effects are facilitated by the formation of optical excitations with relatively long-lived resonances in and around a bubble's surface layer. Such excitations are contained in the vicinity of bubbles during the final stages of compression. The bubbles can briefly be considered as optical resonators without mirrors. A similar mechanism of collective electronic excitation amplification has been referred to in the explanation of surface enhanced Raman spectroscopy, and is also well known in surface infrared spectroscopy.[19,20] The red-side broadening of emission peaks likely arises from Foster-type radiationless migrations of electronic excitations with partial energy loss to the surrounding liquid medium. The distance of

such migrations and the energy transfer loss decreases with the increasing density of species with resonant transitions.

A full analytical description of the many-body dynamics involved in SL would be extremely complicated and would have to include the effects of surface phase transitions and dynamic resonance changes of the localized optical excitations due to changes in parameters affecting the bubble. Such a description is greatly simplified near a transition threshold, the appearance of which is a generally distinctive feature of collective effects. Near such a threshold, dependence of the dynamics on external parameters should be dominated by certain single parameters. In particular, it has been predicted that the dependence on the acoustic driving power J should be proportional to fractional powers of the ratio

$$\frac{J - J_0^{\pm}}{J_0^{\pm}} \tag{11}$$

where $J_0^{\pm}$ are the upper (+) and lower (-) threshold values. These values are highly dependent on the microscopic details of the environment surrounding the emitting species. Threshold dependencies of SL on fractional powers of the ratio in Equation 11 follow from the analogy between dynamic phase transitions and second order, equilibrium phase transitions.[16] Equation 11 substitutes for the normalized temperature difference $(T\text{-}T_C)/T_C$, where T_C is the critical temperature. Correspondingly, the SL peak height I is proportional to the real part of the square-root of Equation 11 near upper and lower thresholds [21]:

$$I \sim \mathrm{Re}\left\{\frac{J - J_0^{\pm}}{J_0^{\pm}}\right\}^{\pm\frac{1}{2}}; \text{ for } \left|\frac{J - J_0^{\pm}}{J_0^{\pm}}\right| < 1 \tag{12}$$

The comparison between dynamical and equilibrium phase transitions is based on a useful, but limited analogy.[16] In particular, J_0^+ and J_0^+ can be complex quantities in the dynamical case due to the contribution of irreversible dissipation processes and to the finite size of the system. The dynamic transition remains sharp only if $\mathrm{Im}\{J_0^{\pm}\} << \mathrm{Re}\{J_0\}$. This inequality is stronger in the SBSL case where parameters are more tightly controlled. In the MBSL case, each bubble exists in a unique environment and system averages are generally measured. Nevertheless, as will be seen in the experimental data below, the existence of distinct thresholds can be seen in MBSL as well.

A characteristic feature of collective transitions is that emission line shapes are defined by the following relationship between width $\Delta\omega$ and peak height I for a constant concentration of excitable species c:

$$\begin{aligned} &\Delta\omega = \Delta\omega_0 + \frac{a}{I}; \text{ for } J > J_0 + \delta; \\ &\Delta\omega \equiv \text{constant for } J < J_0, \end{aligned} \tag{13}$$

where a is a constant, δ is the width of the transition interval of J, and $\Delta\omega_0$ is the minimum width. The dependence of $\Delta\omega$ on I in the collective emission regime is connected to the destruction of the degeneracy of excited species through mutual interactions and phase diffusion.[16] According to Equation 13, $\Delta\omega$ decreases near the threshold as I increases due to increasing correlation length between electronic

excitations. In contrast to Equation 13, peak width in the equilibrium plasmas supposed by some classical theories of SL increases with increasing temperature and emission intensity.

In cavity quantum electrodynamics there can be two distinct regimes for the $\Delta\omega_0$ dependence on external parameters.[22] These correspond to large and small ratios of the number of excited localized optical modes to the number of resonant atomic species. The transition from the first regime to the second is generally non-monotonic, with abrupt changes in $\Delta\omega_0$ at critical concentration values of the resonant species. The corresponding threshold dependence of $\Delta\omega_0$ on the concentration of excitable species in the threshold region for SL has the following form for constant acoustic pressure:

$$\Delta\omega_0 = \Delta\omega_{00} - b\,\mathrm{Re}\sqrt{c - c_0} \tag{14}$$

where b is a constant and c_0 is a threshold value.

To examine the possibility of a cooperative emission mechanism in MBSL, experimental data was compared to the relationships in Equations 12-14. Data from the sodium chloride and potassium chloride experiments provided the best means for the analysis. Typical emission peaks observed are shown in Figure 5-3 and Figure 5-4 (Chpt. V) for sodium and Figure 5-9 (Chpt. V) for potassium. Because peak broadening does not permit half-maximum resolution of the sodium doublet, its peak width FWHM is defined to be the width of the entire doublet measured half way between the maximum and the baseline of the MBSL continuum. Peak height is defined to be the global maximum of the doublet peaks, regardless of which one dominates. While the potassium doublet lines also

overlap to some degree, the peaks are readily resolved. Potassium peak width FWHM is measured only from the higher energy line, half way between its maximum and the baseline of the MBSL continuum. Peak height is determined as the maximum of the more intense, higher energy line.

In the first analysis, the effect of changing acoustic driving pressure on emission intensity and peak shape was studied. Figure 6-1 shows the squared dependence of the sodium peak height on acoustic power. The square of the peak height increases linearly in the threshold region. With higher acoustic pressures, it approaches a maximum level asymptotically. From a plot of peak width versus inverse intensity (Figure 6-2), it can be seen that the sodium doublet narrows with increasing acoustic intensity according to Equation 13. It becomes more linear beyond the threshold region. Similar behavior is observed with potassium emission lines. Next, the shapes of the sodium and potassium resonance doublets were analyzed at a constant reactive acoustic driving power density of 12.4 Watts/cm^2 over a range of salt concentrations. Below a critical concentration c_0, the FWHM remains nearly constant for both salts (Figure 6-3). Beyond the threshold, red-wing broadening diminishes. At concentrations above 1.5 molar, the individual peaks of the sodium doublet are distinguishable, becoming better resolved with higher concentrations (Figure 5-4, Chpt. V).

The non-monotonic dependences of peak width and intensity from sodium and potassium MBSL shown here cannot be explained in the framework of classical hydrodynamic models. It does, however, support a cooperative, non-equilibrium emission mechanism. Excitation could result from rapid thermal heating during bubble collapse, as

proposed in reference 4. Another mechanism for cooperative emission could result from a surface phase transition. During the final compression stage of a bubble collapse, dipolar molecules in the surface layer may undergo a phase transitions of the second order, with the bubble radius serving as the dependent external parameter. The transition takes place if compression is so fast that the surface species can not establish equilibrium with the bulk solution. During this process, localized optical excitations could form on the bubble surface. In the MBSL case, long-range collectivization could even include excited dipoles in a number of adjacent bubbles. This could allow individual emission peaks to be much narrower than in the SBSL case, where atomic emission lines are not observed for an unknown reason. Square-root threshold behaviors are not limited to the MBSL case, but can be observed in SBSL as well. In experiments by Pecha *et al.*[23] a streak camera was used to measure the duration of SBSL emission. As can be seen in Figure 6-4 a plot of the square of the FWHM emission time versus acoustic driving pressure reveals a nearly linear dependence.

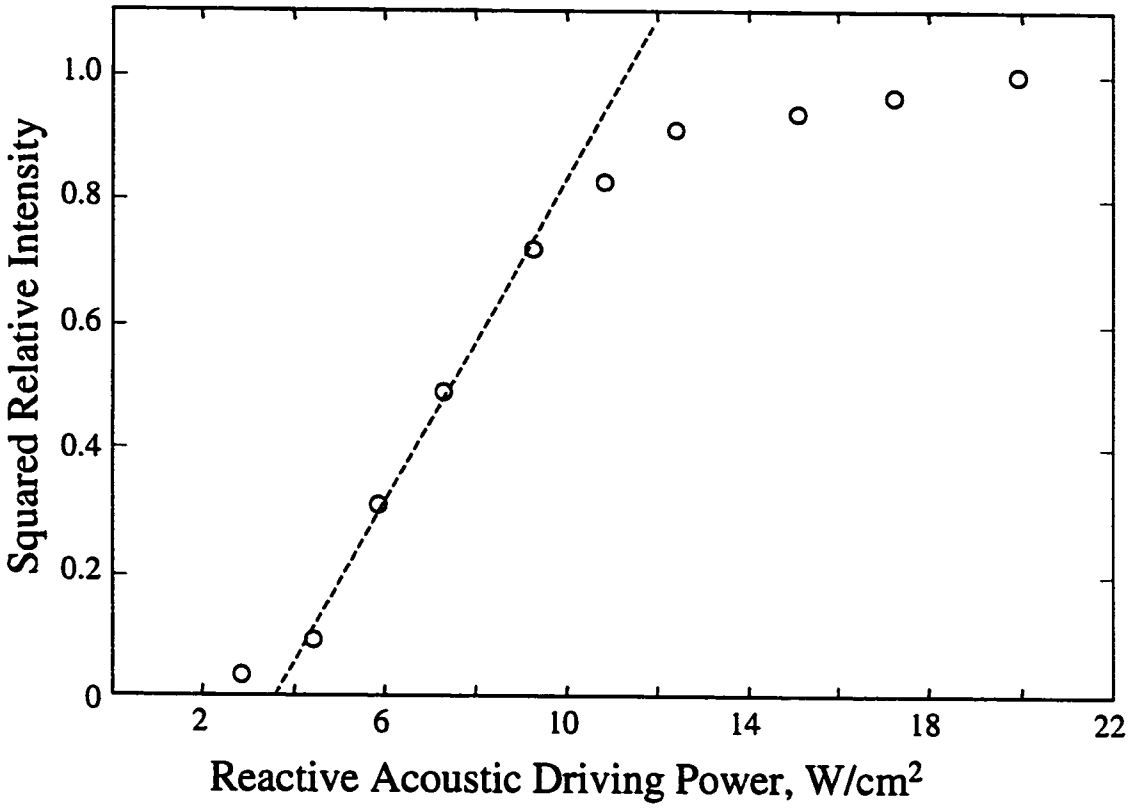

Figure 6-1. Squared Dependence of Peak Height on Acoustic Power

The squared peak height dependence of the sodium doublet on acoustic power is shown for a solution of 1.00 molar sodium chloride. The dashed line corresponds to Equation 12 for a real value of J_o^- determined from the data.

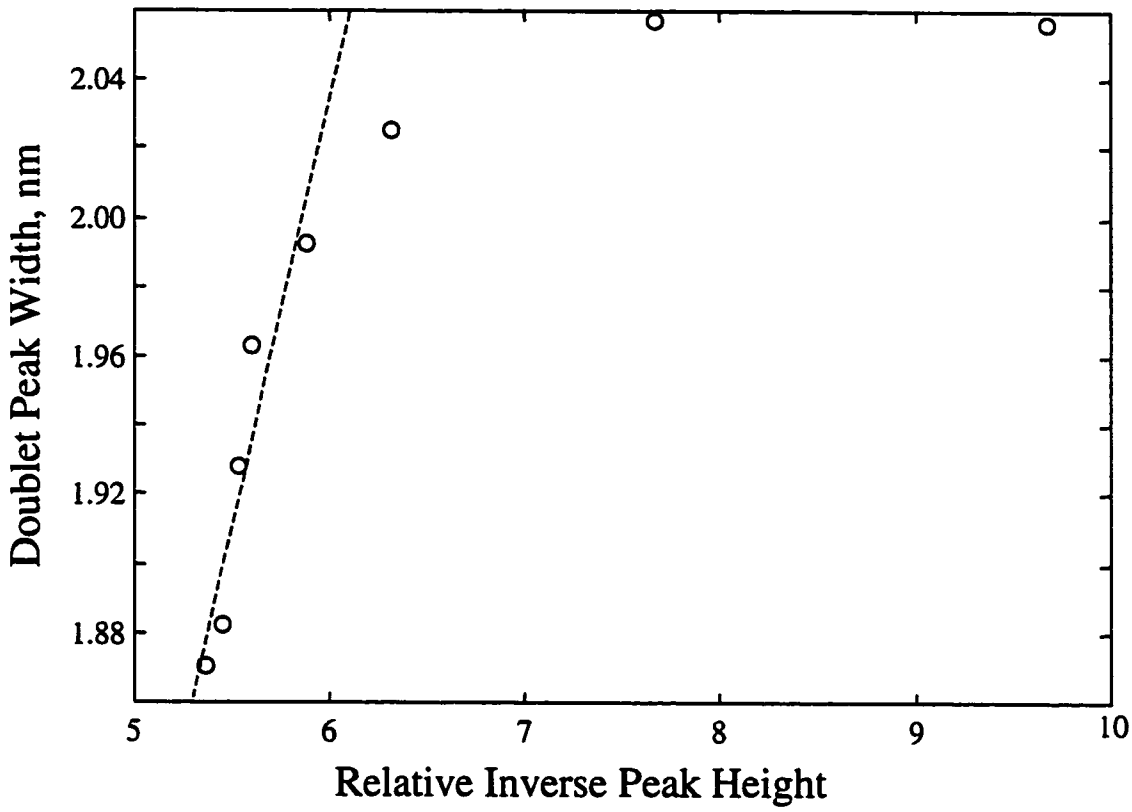

Figure 6-2. Inverse Relationship Between Peak Height and Width

Atomic peak widths decrease with increasing peak intensity. The data points are from the same experiment shown in Figure 6-1. The dashed line corresponds to theory of Equation 13.

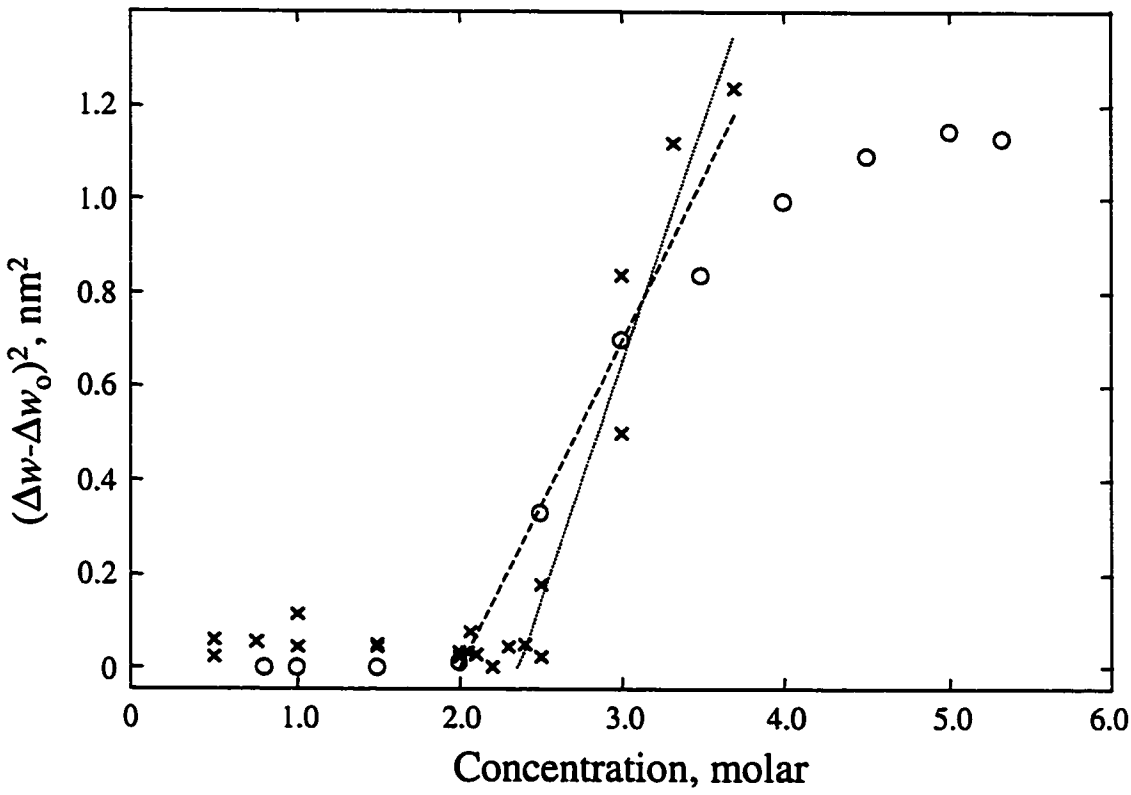

Figure 6-3. Dependence of Peak Width on Concentration

The peak width Δw dependence of sodium (o) and potassium (x) D line emissions are shown from 0.5 molar to near-saturation. Δw_0 was determined experimentally from the region of constant peak width. The dashed (sodium) and dotted (potassium) lines are theoretical fits to Equation 14.

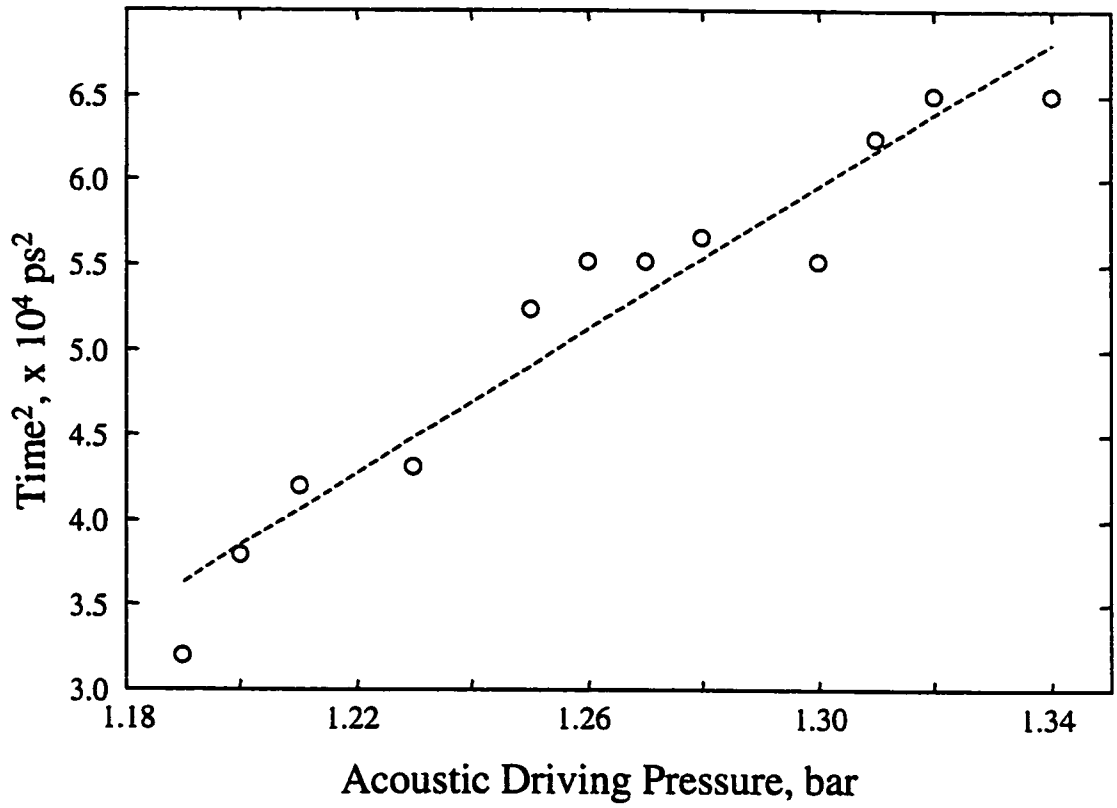

Figure 6-4. Square-Root Dependence in SBSL

The square of the FWHM emission duration of SBSL is shown to depend nearly linearly on acoustic driving pressure. The data points resulted from analysis of streak camera emission time measurements from reference 23. The dashed line corresponds to a linear best-fit to the square of the experimental data points.

Notes to Chapter 6

(1) Gaitan, D. F.; Crum, L. A. **Frontiers of Nonlinear Acoustics,** 12th ISNA. (Elsevier Applied Science, London, 1990) pp.459-463.

(2) Moss, W.; Clarke, D.; Young, D. *Science* **276**, 1398 (1997).

(3) Crum, L. A. *J. Acoust. Soc. Am.* **95**, 559 (1994).

(4) Mohanty, P.; Khare, S. *Phys. Rev. Lett.* **80**, 189 (1998).

(5) Kuhns, D.; Brodsky, A. M.; Burgess, L. W. *Phys. Rev. E* **57**, 1702 (1998).

(6) Brodsky, A. M.; Burgess, L. W.; Robinson, A. L. *Ultrasonics*, accepted for publication as of Sept. 2000.

(7) Barber, B. P.; Wu, C. C.; Lofstedt, R.; Roberts, P.; Putterman, S. J. *Phys. Rev. Lett.* **72**, 1380 (1994).

(8) Lentz, W.; Atchley, A.; Gaitan, D. *Appl. Opt.* **34**, 2648 (1995).

(9) Barber, B. P.; Hiller, R. A.; Loefstedt, R.; Putterman, S. J.; Weninger, K. R. *Physics Reports* **281,** 65 (1997).

(10) Hiller, R. A.; Putterman, S. J.; Weninger, K. R. *Phys. Rev. Lett.* **80,** 1090 (1998).

(11) Matula, T.; Roy, R. *Ultrason. Sonochem.* **4**, 61 (1997).

(12) Brodsky, A. M. *Mod. Phys. Lett. B* **13**, 1019 (1999).

(13) Brodsky, A. M., *J. Math. Phys.* **38**, 5127 (1997).

(14) Mohanty, P. http://xxx.lanl.gov/format/cond-mat/0005233

(15) Mohanty, P. http://xxx.lanl.gov/format/cond-mat/9912271

(16) Andreev, A.; Emelyanov, V. I.; Ilinskii, Y. A. **Cooperative Effects in Optics** (IOP Publishing, Philadelphia, 1993).

(17) Wiersma, D. S.; van Albada, M. P.; Lagendijk, A. *Phys. Rev. Lett.* **75**, 1739 (1995).

(18) de Oliveira, P. C.; Perkins, A. E.; Lawandy, N. M. *Optics Lett.* **21,** 1685 (1996).

(19) Moskovitz, M. *Rev. Mod. Phys. Part 1* **57**, 783 (1985).

(20) Brodsky, A. M.; Urbakh, M. *Progress in Surface Science* **33**, 91 (1991).

(21) Landau L.; Lifshitz, E. **Statistical Physics, Part I** (Pergammon Press, Oxford, 1980) Chpt. 24.

(22) Münstermann, P.; Fischer, T.; Maunz, P.; Pinkse, P. W. H.; Rempe, G. *Phys. Rev. Lett.* **84**, 4068 (2000).

(23) Pecha, R.; Gompf, B.; Nick, G.; Wang, Z. Q.; Eisenmenger, W. *Phys. Rev. Lett.* **81**, 717 (1998).

Chapter 7

Novel Flow Cells

The analytical ability of sonoluminescence was established in the apparatus described in Chapter III. The centerpiece was a stainless steel acoustic cell where 80 mL of sample was recirculated in a batch process format. While this may be an effective method of delivering continuous ultrasound for sonophysical or sonochemical effects, it presents certain inefficiencies. Before a sample can be analyzed in the batch format, it must be measured, transferred to the cell, sparged with argon for ½ hour, and pre-sonicated for ten minutes. A 50 minute analysis time may make this method inadequate for process monitoring of more quickly changing systems. For analysis of a process stream, an on-line flow-through cell has several advantages over the stainless steel cell. Most importantly, it can reduce sample volume and preparation, increase control over parameters affecting sonoluminescence, and provide nearly real-time, continual analysis of fresh sample.

With these goals in mind, a number of flow-through cells were designed, fabricated, and characterized. A common trait to each is that an external transducer was acoustically coupled to a tube through which the sample was pumped. By this method, tubes sizes and flow rates could be changed to optimize sample volume and

sonoluminescence intensity. Several cells are described below along with the pros and cons of each. With each cell, acoustic coupling was a factor that needed to be taken into account. As with any wave, reflections occur at interfaces where relevant physical properties change (Chapter III, Equation 8). Thin-walled Teflon was found to transmit energy relatively well, while stainless steel reflects 95% of incident acoustic energy. Successful coupling through stainless steel and glass was achieved in two acoustic cells.

To approximate a process line format, samples were conditioned in-line while being pumped to the acoustic cell (Figure 7-1). Solution was generally pumped through tubes from a 20 mL reservoir, where a frit sparged the sample with moisture saturated argon gas. The reservoir volume was replenished through continual siphoning from a larger reservoir. Though this created small volume fluctuations in the sparging reservoir, it did not appear to affect the analyses. After sparging, sample passed through the pump and into a stainless steel coil submerged in a thermostatting bath at 0° Celsius. The acoustic cell immediately followed. With a flow rate of 1 mL per second (through 1/16" ID tubing), the temperature of the sample exiting the cell was 5.3° ± 0.2° Celsius.

A. HIFU Cell

One of the issues associated with high power ultrasound is cavitation damage on solid surfaces (Figure 3-2). A method for reducing this problem was implemented by using a HIFU (high intensity focused ultrasound) transducer mounted on an ultrasound water tank (Figure 7-2).* Focusing allows the generation of high power densities with

lower driving power and power density near the transducer, thus protecting the sonication surface from cavitation damage. The transducer (custom built by Sonic Concepts, Inc., Woodenville, WA) was a two inch diameter concave cup, with a two inch radius of curvature, and a 1.1 MHz resonant frequency. A stainless steel plate of matching curvature mechanically backed the outer surface, and a thin film of impedance matching rubber protected the inner surface. The transducer was mounted to a small ultrasound water tank with acoustic absorbers on the opposing wall to reduce acoustic backscatter. With low amplitude oscillations, a small zone of high intensity ultrasound could be generated two inches from the transducer surface. In water with dissolved gas atmospherically equilibrated, the cavitation zone was clearly audible and visible with appropriate lighting. This was useful for positioning the sample tube, as acoustic self-focusing and streaming deformed and slightly shifted the cavitation zone from its geometrically calculated shape and position. Degassed water was used in the tank during experiments to reduce cavitation in the coupling fluid. The reason for this was two-fold. First, cavitation bubbles outside the sample tube reflect and scatter acoustic energy before it reaches the tube. Secondly, cavitation outside the tube would cause sonoluminescence virtually indistinguishable from that inside the tube. An opaque sample tube resolves the latter issue.

For the experiments, a 0.125"/0.115" OD/ID Teflon tube was placed in the center of the cavitation zone. A 1.0 molar sodium chloride solution was sparged with argon, cooled, and flowed through the cavitation zone. SL was collected with a UV grade fiber optic located at a T-junction near the cavitation zone. Total intensity was measured with

the Hamamatsu photon counting module while the transducer was driven up to its power tolerance limit. Maximum intensity was measured at ~2300 counts per second. By comparison, 160,000 counts per second was measured from the acoustic horn system. During the course of experiments, the coupling water in the tank warmed a few degrees Celsius from the acoustic energy. Cavitation outside the sample tube became more apparent as atmospheric gasses dissolved into the coupling water. These changes in the coupling fluid caused unstable, irreproducible SL signals.

While spherical focusing produced some initial success, there are additional drawbacks associated with creating zones of intense cavitation. Acoustical shielding, mentioned above, can be detrimental. The effect intensifies if bubble densities are high enough that coalescence occurs. It has been discovered that in some acoustic cells more SL emission can be coaxed from a gentle cavitation field than from more violent fields. Finally, with a highly localized cavitation zone, all sonoluminescence signal must be collected from a small area. Some of these drawbacks were addressed in the next generation cell.

B. Cylindrically Focused Cell.

To address some of the disadvantages of the HIFU system, a new acoustic cell was designed (Figure 7-3). Fabrication was performed by Sonic Concepts, Inc. The first major design change was to use a hollow cylinder transducer. Oscillated in a radial resonance mode (71.6 kHz), acoustic energy was focused to a line, where a thin-walled

Teflon tube was located (0.375"/0.355" OD/ID). A UV grade fiber optic was guided through the center of the sample tube to collect SL at the edge of the cavitation zone. The second design change involved acoustic coupling between the transducer and the sample. Several permanent options were considered, but ultimately degassed water was chosen so that a variety of sample tubes could be tested and easily replaced when necessary. Degassed water was pumped through the volume between the outer wall of the sample tube and the inner wall of the transducer. The plumbing for this water was sealed to prevent gassing up. The coupling water also passed through a cooling coil to reduce sample temperature and thermostat the transducer, which can potentially heat to the point of failure. Sample was pumped through the central tube with a Gilson pump (model 303) with flow rates from 1 to 10 mL/min. Power was provided to the transducer with a model 1040L AC amplifier from ENI and a model 335 waveform generator from Stanford Research Instruments. A variable attenuator was placed at the output of the waveform generator to further reduce the input voltage to the amplifier and to permit fine control of the acoustic power.

With cylindrical focusing, a line of cavitation was generated inside the sample tube. This provided good SL intensity with gentle cavitation. In fact, the brightest SL was achieved at lower acoustic powers. By comparison, chemiluminescence from luminol under the same conditions increased linearly with increasing acoustic power. Luminol chemiluminescence is activated by free radicals and electrons generated during cavitation. With argon sparging but no cooling, maximum sustainable SL intensities were measured for several solutions summarized in Table 7-1. Faster flow rates produced

brighter SL, and short-lived periods could produce up to 120,000 counts/sec for 1-2 seconds.

The design of this acoustic cell effectively addressed some of the drawbacks of the previous generation. However, improvements were still possible. The dissolved gas concentration in the coupling water changed continuously during experiments. It would further degas during experiments, and then redissolve the gases when the transducer was off. The extent of degassing was affected by the power applied to the transducer. One source of a gas leak was the Teflon tube itself, which has high gas permeability coefficients. With changes in the coupling fluid came instabilities in the SL signal, making reproducibility difficult. Dissolved gases outside the sample tube also caused cavitation, which could contribute SL to the analyte signal as well as damage the transducer. It was also somewhat laborious to replace the volume with freshly degassed water. Another issue may be the use of Teflon for the sample tube. Chosen for its chemical inertness, it is naturally hydrophobic. Bubbles generated near the Teflon wall are attracted to it to lower their surface tension. Once near the wall, cavitational jetting causes damage. Figure 7-4 shows the inside of the cell wall under magnification after several weeks of experimentation. The outside of the wall was undamaged, demonstrating the effectiveness of degassed water for cavitation suppression.

C. Directly Coupled Cells.

To address the issues presented above, two new cells were fabricated with the acoustic transducers directly coupled to the sample tubes (Figure 7-5). The transducers were thin-wall hollow cylinders ordered from Channel Industries (C5400 material). Several factors were considered when choosing them. Overall dimensions must follow empirical formulas, which can be found in Channel Industries' informational brochure. For effective cavitation, thicker transducers can withstand higher driving powers. However, their resonances occur at lower frequencies, causing large cavitation bubbles unsuitable for small flow-through cells. For a small, thin-wall tube shape, the ratio of inner to outer diameters must be small, and the length must be on the same order for acceptable mechanical strength. A compromise between inner diameter size and wall thickness led to the selection of sample tube outer diameters of 0.15 to 0.27 inches. Several transducers that that fell within the above constraints were chosen and combined with stainless steel and Pyrex® glass tubes. The sample tube outer diameters were closely matched to the inner diameters of the transducers (Table 7-2). For the largest of the Pyrex® cells there was 0.011 inch gap between the transducer and sample tube. Four 4.5-mil (0.0045") wires were used as permanent spacers when the epoxy was filled for this cell. These wires also served as ground leads for the transducer. The transducer on this cell also had the largest wall thickness and provided the brightest sonoluminescence.

Although stainless steel and glass have large acoustic impedance mismatches with water, efficient energy transfer was achieved by directly driving the tube walls with the transducers. Mechanical bonding was achieved with Epo-Tek H20E silver-filled epoxy.

A metal-filled epoxy can be designed to have an acoustic impedance mid-way between glass/metal and water by changing the weight percent of the metal. This improves energy transfer to the liquid. Acoustic impedance tuning of the Epo-Tek epoxy was not performed, as acoustic coupling was already acceptable. The epoxy also provided electrical contact between the ground lead wires and the transducers.

After fabricating the cells, a Hewlett-Packard 4192 Impedance Analyzer was used to determine the electrical properties of the transducers. This step must be done after the transducers are mounted, as loading changes these properties. The analyte tube should also be filled with water. The analyzer program (written in LabView) provided plots of complex impedance magnitude (Z) versus frequency, and the phase between driving current and voltage (ϕ) versus frequency. (Figure 7-6) Frequencies at which the complex impedance peaks and the current versus voltage phase approaches zero often correspond to transducer resonances. In Figure 7-6 two resonance candidates are observed at 224 and 227 kHz. These plots provided practical starting frequencies for the cell characterization. However, it was found that running the transducer at cavitation powers shifted the resonance to 222 kHz. The shift occurred over a period of minutes, and was a result of temperature equilibration. Salt concentrations changes, and thus fluid density changes, did not noticeably change the resonance frequency. An observation of that is worth mentioning is that one acoustic cell that did not produce sonoluminescence had unusually high values of complex impedance. Consultation with an experienced electrical engineer brought about the conclusion that the transducer was not efficiently coupled to the analyte tube. The complex power spectrum resembled one of an unloaded transducer.

As with the cylindrically focused cells, solutions were sparged with argon and cooled and while power was supplied to the transducer through the waveform generator-attenuator-amplifier circuit. The stainless steel and glass cells produced SL when driven near the resonant frequencies determined by the impedance analyzer. As a transducer warmed up the driving frequency was manually lowered while the resonance shifted to lower frequencies until equilibrium was achieved. Location of the current resonance frequency was determined by monitoring the current and voltage waveforms via the complex power meter on a LeCroy 9350 digital oscilloscope (Figure 7-7). This arrangement also provided the means to calculate the power applied to the transducers, which was approximately 0.35 Watts for the brightest observed SL. Higher powers were not applied to protect the transducers from shattering or decoupling from the analyte tubes. It was found that dephasing the driving current and voltage by 25 degrees (current leading), maximized sonoluminescence intensity. This caused less than 10% of the driving energy to be lost to circuit heating and enhanced the signal by 20% or more. Maximum intensities for the stainless steal and Pyrex cells were 6×10^5 and 1.2×10^6 counts per second, respectively. Maximum sustainable intensities were 3×10^5 and 6×10^5 counts per second, respectively.

Initial experiments began from the moment power was applied to the transducer. After periods of dormancy longer than several hours, SL was not immediately seen. After 20-40 seconds, the signal would suddenly appear. This was attributed to initial conditioning or warming up of the transducer. Once SL was observed, it's intensity slowly cycled through intensity maxima and minima with periods of several minutes.

This continued for 20-30 minutes, after which the signal became steady. For process monitoring, the transducer could be run continuously. SL from the Pyrex cell after final signal stabilization is shown in (Figure 7-8) for a 2 molar sodium chloride solution. Short term fluctuations can be largely explained by the integration time of the PMT (1 second), and the rate of peristaltic pumping (~2.4 pumps/second). Figure 7-9 shows data acquired with 10 millisecond integrations for the same system. Intensity spikes correspond to when the peristaltic pump induced hydraulic pressure pulses in the fluid. This is analogous to the hydrostatic pressure pulses observed previously.[1] With 1 second integrations (Figure 7-8), approximately every other data point would consist of SL enhancement from an extra pressure pulse. The plot with shorter integration times demonstrate the achievable stability in the absence of pressure spikes. Steady pressure could be achieved with a syringe pump in a laboratory setting, or through other more involved methods on-line. The pressure spikes are not detrimental to the spectroscopic analysis, but indeed enhance the light emission.

A series of sodium chloride solutions were analyzed using the Pyrex cell and the spectrometer with CCD detector. The sodium peak height was compared to the total SL signal collected with the blue-sensitive photon counting PMT for the new cells and the acoustic horn system. While the PMT measured much brighter SL from the new cells, the sodium signal was much brighter from the acoustic horn system. It follows that the spectral energy was shifted to higher energies in the new cells. This effect has been documented in studies of the effects of frequency on SL spectra[2].

SL emission from the concentration series produced very similar spectra, each with the sodium doublet resolved to approximately the half-height. Figure 7-10 shows that the peaks overlap to a high degree when normalized to the height of the higher energy peak. The variations observed on the lower energy tail did not correlate to concentration, nor did overall intensity of the unnormalized peaks. As correlations between peak shape and concentration were the basis for the analysis of Chapter 5, it appears that these particular cells are not useful for high sodium salt analysis. However, sodium peak height from solutions below 1 molar did correlate well with peak height. The peak shapes were identical to the higher concentration ones. A simple analysis of the ratio of peak height to SL baseline was sufficient for the low concentration analysis. From the observed effects of driving frequency here and in the study by Gordeychuk *et al.*,[2] it is quite likely that cells built with for lower frequencies would provide the information for quantification at higher concentrations. For large volume processes, like the chlor-alkali process, it would be practical to use larger diameter tubes and transducers. For smaller volumes, it should be possible to use large diameter transducers coupled to thick-walled analyte tubes with small inner diameters and volumes.

An unanticipated application that arose from the development of these sonoluminescence cells involved a sonophysical method. The precursor fluid mixture for making injectable ultrasound contrast agent from Sonus Pharmaceutical Inc. was flowed through the Pyrex cell during sonication. Gas filled ultrasound contrast bubbles formed and were observed under a microscope. Single-pass insonation of the fluid within a syringe or bottle may provide an effective method for reproducibly generating bubbles of

the proper size and distribution. These experiments were cursory, and an extensive systematic study would be required for FDA approval.

D. Conclusions

Alternative sonoluminescence cells were explored to find a faster, more efficient method of analyzing solutions. Focusing transducers were found to be effective at generating cavitation in small, localized points or lines in flowing sample cells. One issue studied involved coupling the ultrasound to the analyte. Coupling fluids changed too easily, preventing reproducible analysis. Directly coupling ultrasound through the analyte wall proved most effective. However, sodium spectra at high concentrations did not provide discriminating information. Low concentrations could be analyzed by ratioing two wavelengths. Larger transducers with lower resonant frequencies may solve this issue. The directly coupled tubes also provide an opportunity for using other sonochemical or sonophysical techniques on small, flowing systems.

Table 7-1. Maximum Sonoluminescence Intensities for Cylindrically Focused Cell

Solution	Photon counts/sec
DI water	10,000
1 M NaCl	36,000
1 M $CaCl_2$	51,000

Table 7-2. Physical Properties of Directly Coupled Cells.

	Cell 1	Cell 2
transducer:		
outer diameter	0.205"	0.375"
inner diameter	0.155"	0.269"
length	0.200"	0.375"
equilibrium resonant frequency	380 kHz	222 kHz
sample tube:		
material	304 SS	Pyrex glass
outer diameter	0.148"	0.255"
wall thickness	0.135"	0.155"
maximum sustainable intensity with NaCl	6×10^5 counts/sec	1.2×10^6 counts/sec

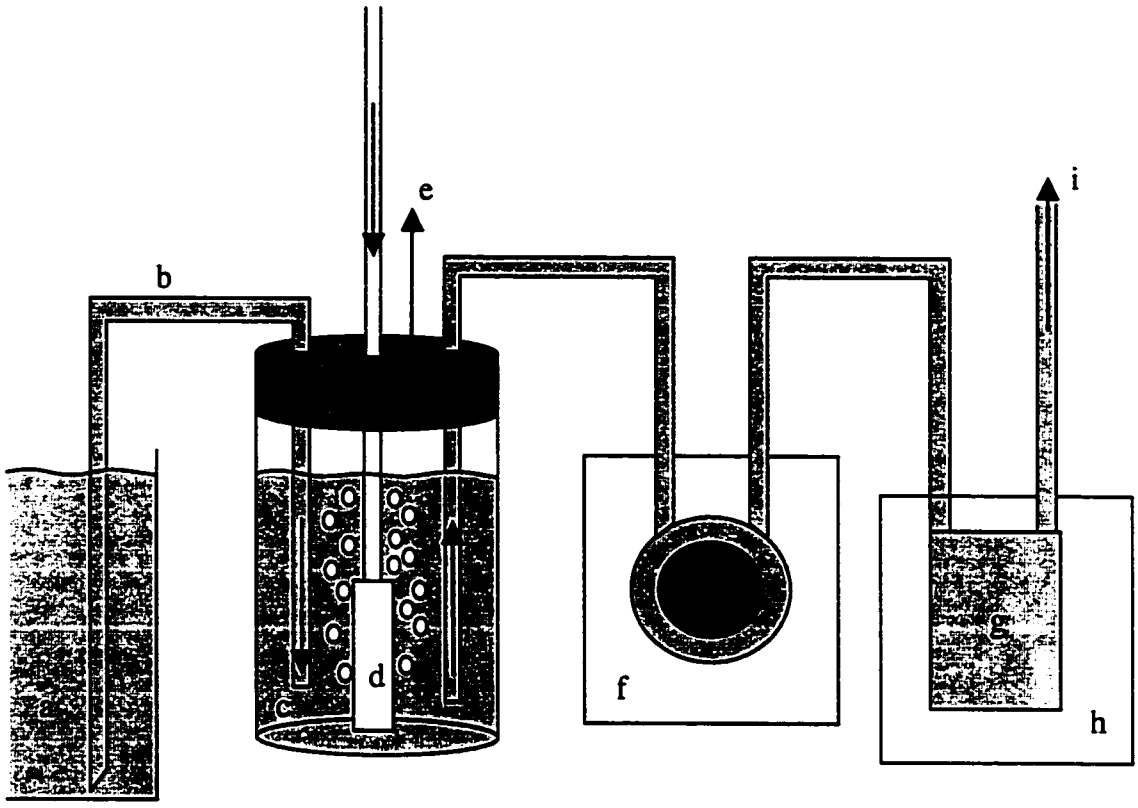

Figure 7-1. Sample Pretreatment Apparatus

Fluid was drawn from a reservoir (a) through a siphon (b) into a chamber (c) where argon gas sparged it with through a frit (d). A peristaltic pump (f) pumped the sample through a coil (g) submerged in a thermostatting bath (h) and then to the acoustic cell (i).

Figure 7-2. HIFU Transducer Cell

Sample was pumped through a Teflon tube (a) at the 2½ inch focal point of a high intensity ultrasound (HIFU) transducer (b). A fiber optic collected SL light from where the Swagelok fitting (c) ends. A second passive transducer that detects cavitation can be seen directly behind the sample tube.

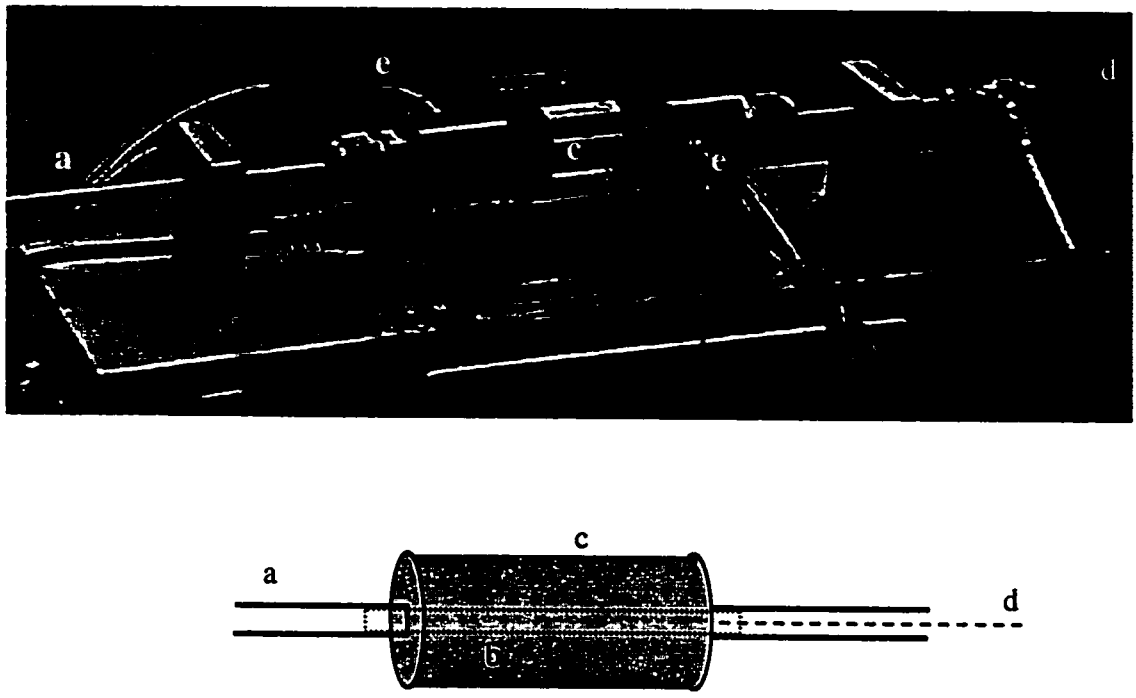

Figure 7-3. Cylindrically Focused Cell

Sample was pumped through a stainless steel tube (a) to a Teflon tube (b) located concentrically with a cylindrically focused transducer (c). A fiber optic (d), brought in from the left above, collected SL light from the edge of the transducer. Degassed water, used as a coupling fluid between the transducer and sample tube, was pumped through the cell via ports (e) located in the black Delrin blocks.

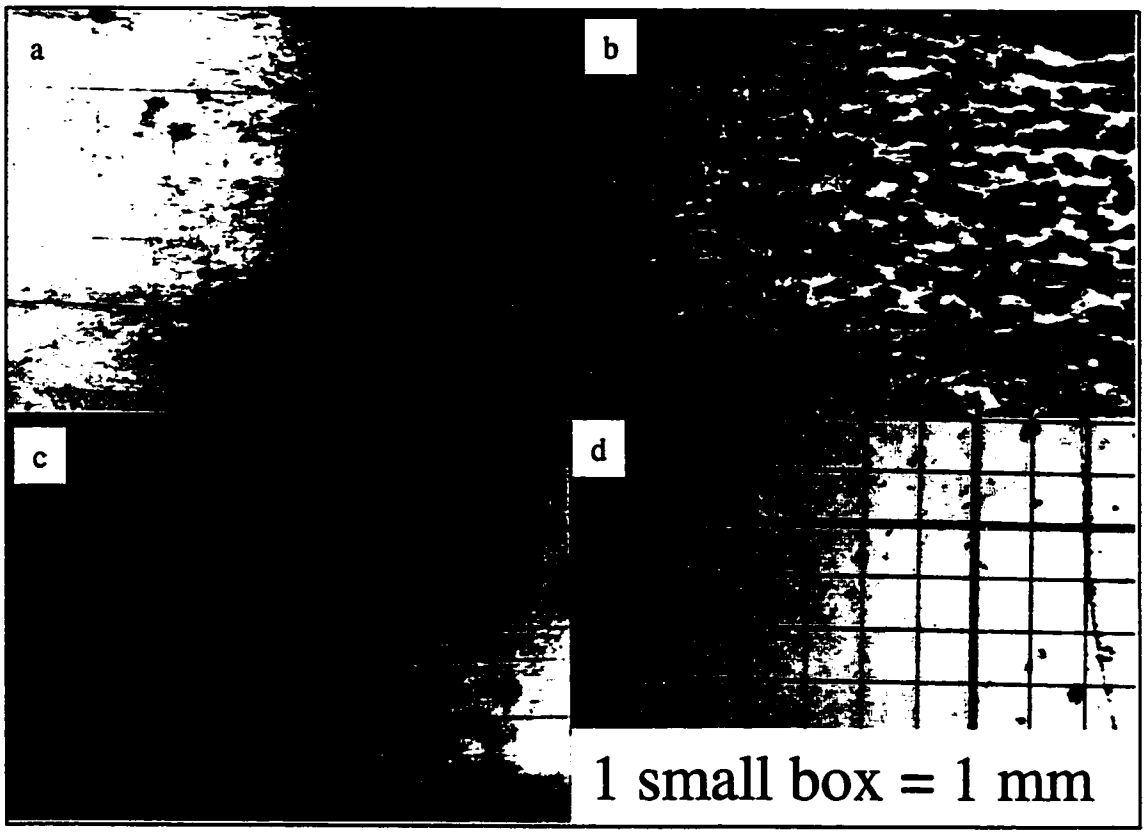

Figure 7-4. Cavitation Damage

Several sections of the Teflon sample tube used with the cylindrically focused cell are shown. Sections were taken from (a) the edge of the cavitation zone, (b) deep inside the cavitation zone, and (c) well removed from the cavitation zone. A grid (d) under the same magnification is shown for scale.

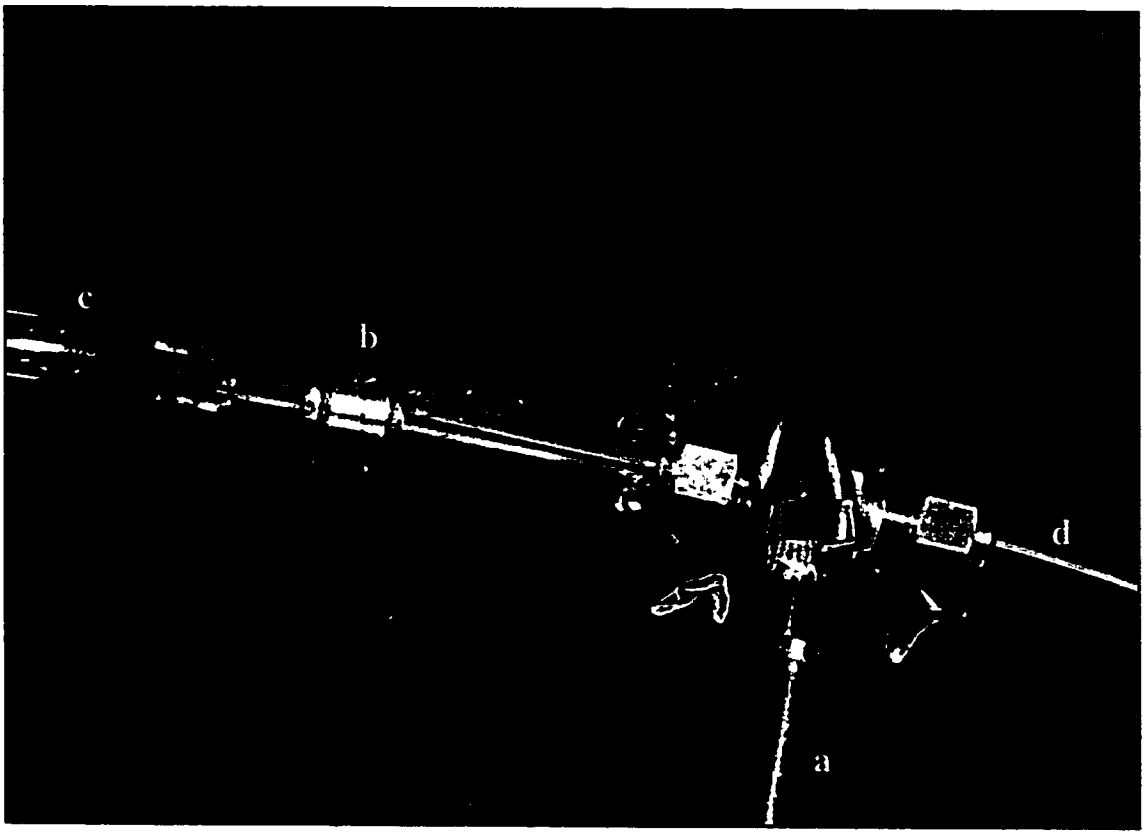

Figure 7-5. Directly Coupled Cylindrical Cell

Sample was pumped through this glass cell from (a) through the transducer (b) and out to waste through (c). A fiber optic (d) ran through a Swagelok T into the tube and collected sonoluminescence from the edge of the transducer. The electrical leads can be seen hanging down from the transducer.

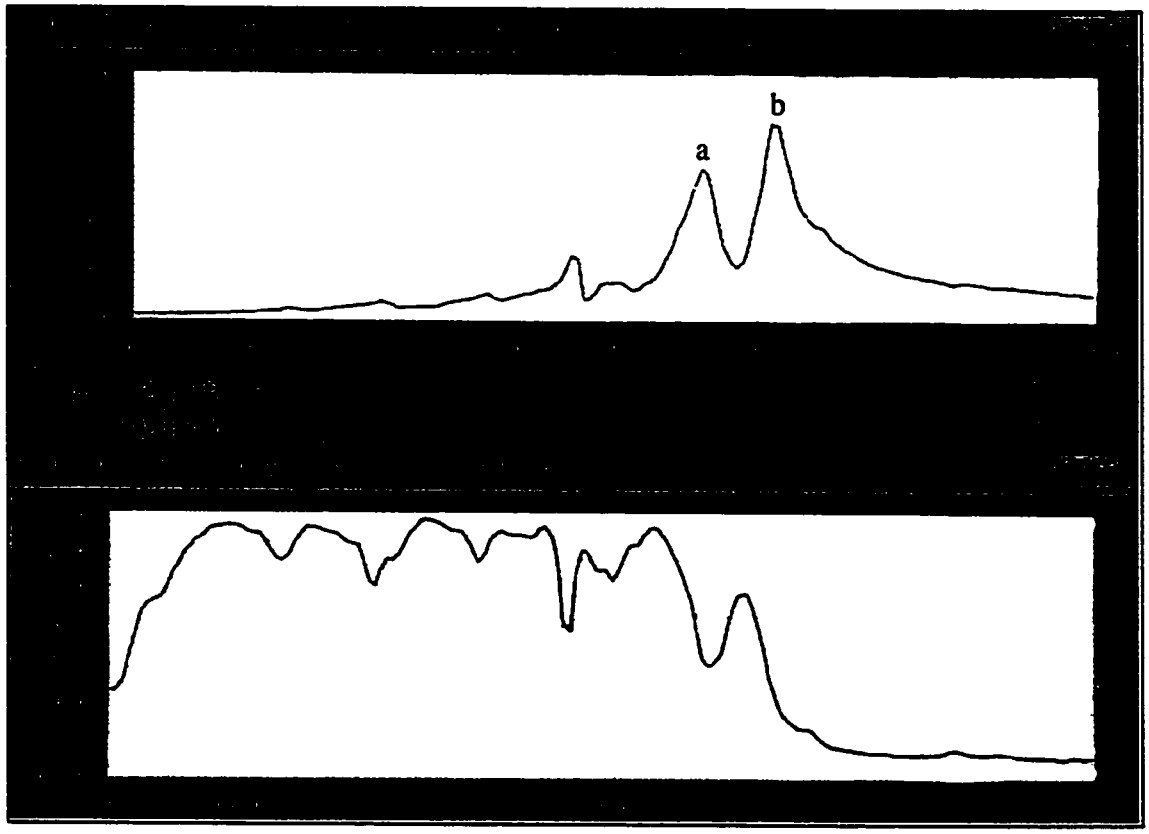

Figure 7-6. Impedance Analyzer Traces for Flow-Through Cell

A plot of complex impedance versus frequency (top) shows where the maximal resistive responses of a transducer occur: a) 224 kHz, b) 227 kHz. These usually correspond to transducer resonances. The second plot (bottom) shows the phase relationship between the driving current and voltage. When in phase, driving energy is optimally used to create transducer motion. These plots were acquired from a LabView program interfaced with an HP 4192 Impedance Analyzer.

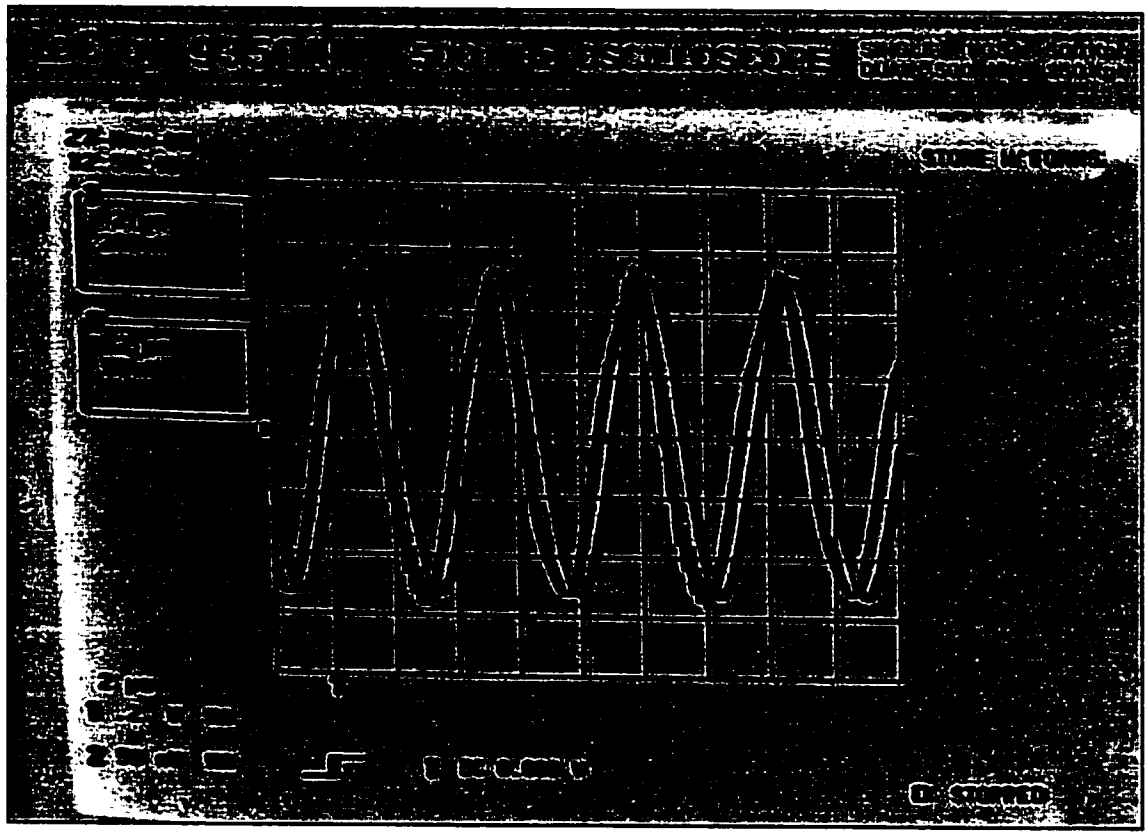

Figure 7-7. Optimal Driving Current and Voltage Phase for Flow-Through Cell

Sonoluminescence was maximized when the driving current and voltage were dephased with the current leading by 25 degrees. These waveforms were acquired with a LeCroy 9350AM digital oscilloscope from the complex power meter, which was in-line between the amplifier and transducer.

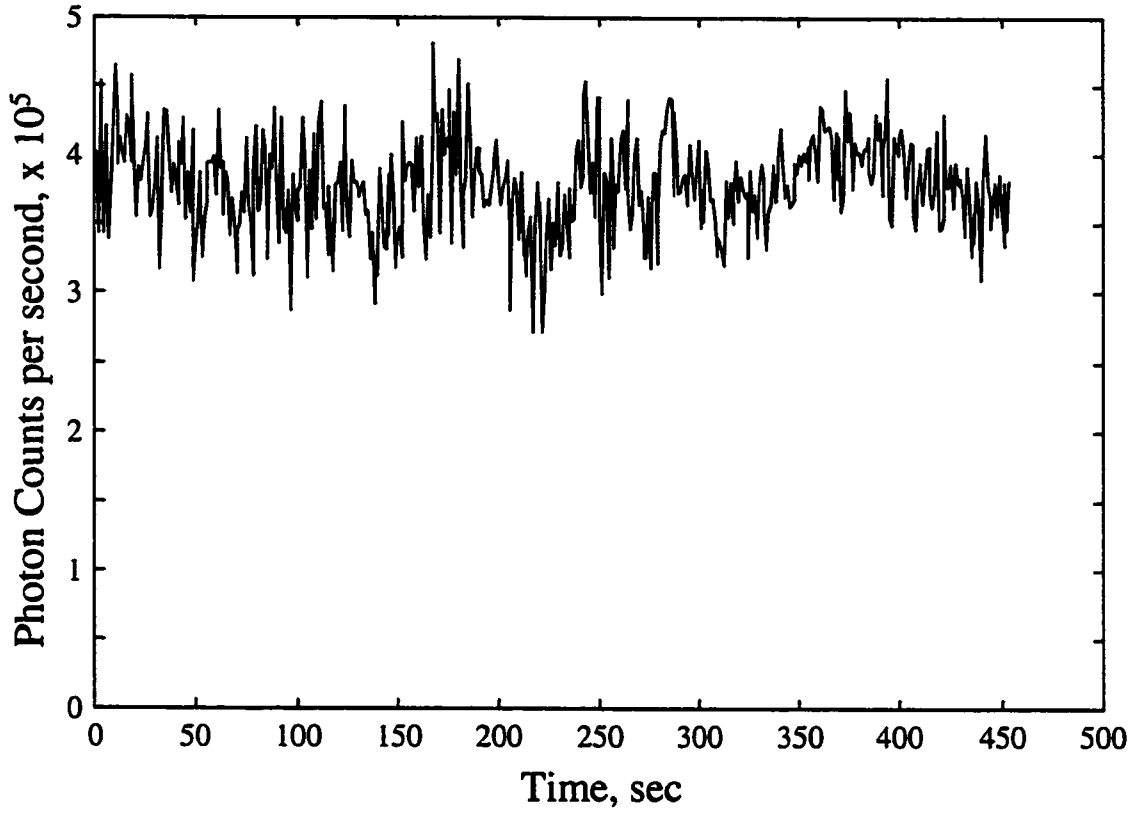

Figure 7-8. Signal Stability of Flow-Through Cell

The long-term stability of the SL signal can be seen from cavitation of a 2 molar solution of sodium chloride. With one second light integrations, short term fluctuations resulted from the timing of hydrostatic pressure pulses induced by the peristaltic pump.

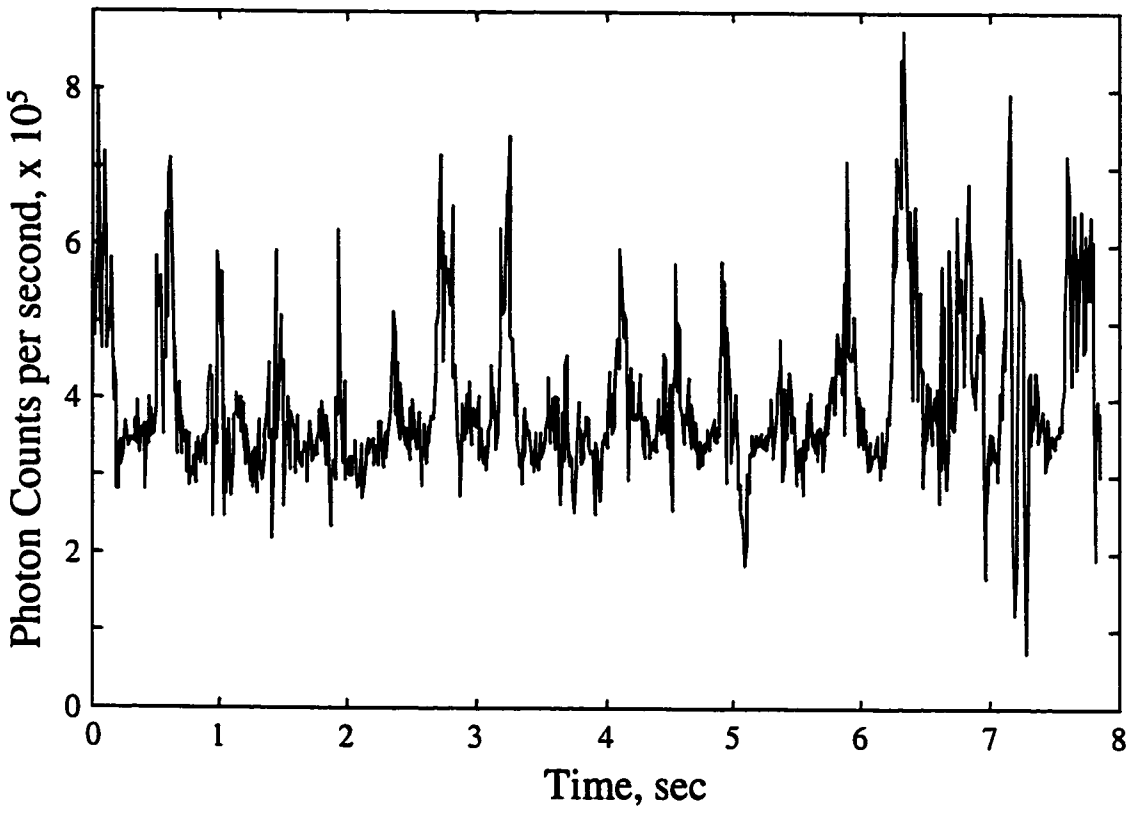

Figure 7-9. Hydraulically Induced SL Spikes in Flow-Through Cell.

The peristaltic pump driving sample through the acoustic cell induced periodic pressure pulses in the solution. Hydrostatic pressure jumps have previously been observed to induce rapid increases in SL intensity. The periodicity of the pressure pulses explains the short-term fluctuations observed in Figure 7-8.

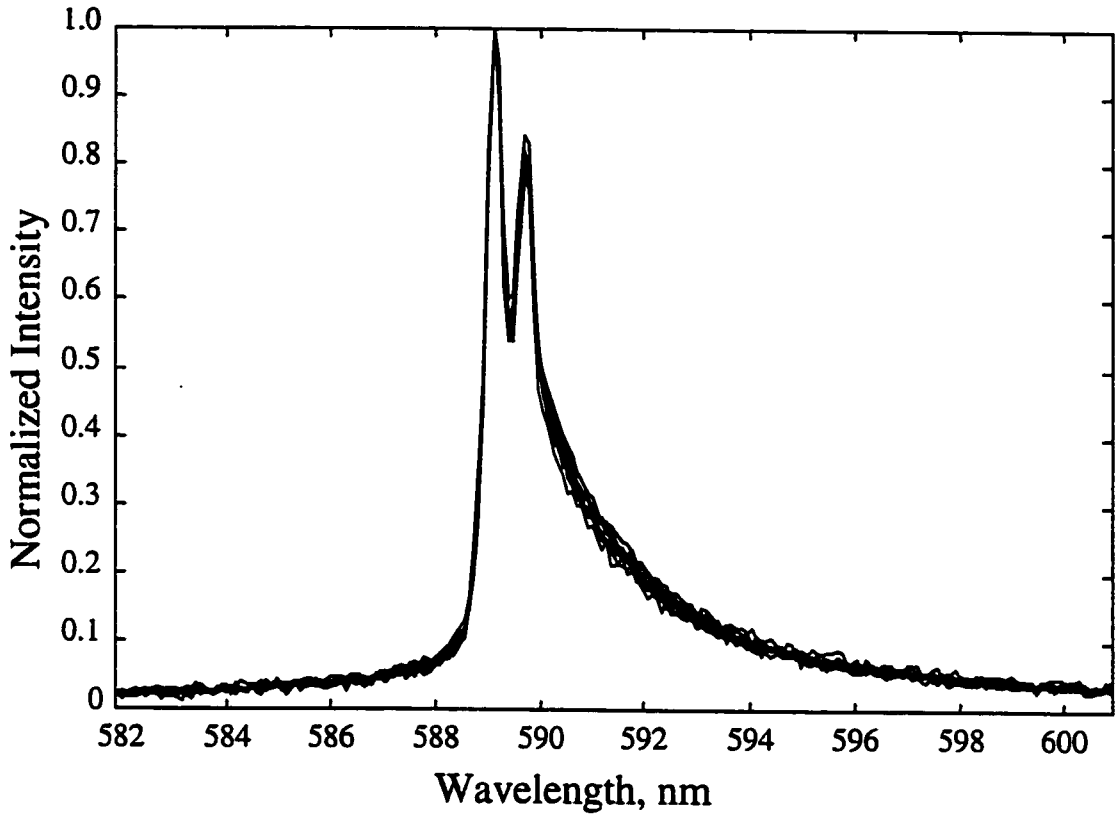

Figure 7-10. Sodium SL Emission from Flow-Through Cell

Sodium SL emission spectra from various concentrations of sodium chloride overlap each other to a high degree when normalized to the same intensity. No correlation between peak height or width and concentration was obtained for concentrations over one molar.

Notes to Chapter 7

(1) Kuhns, D. W., Ph.D. Dissertation, University of Washington (1997).

(2) Gordeychuk, T. V.; Didenko, Y. T.; Pugach, S. P. *Acoustical Physics* **42**, 240 (1996).

Chapter 8

Extended and Additional Work

Although the field of acoustics has been explored for centuries, many experimental results have been difficult to interpret. Advancements in use have thus been concentrated in a few narrowly defined areas. Ultrasonic imaging it likely the most advanced method involving acoustics, utilizing state-of-the-art electronics and computer algorithms. As computational power increases and equipment and theory improve, more uses for ultrasound will be discovered. These will come in the areas of physical effects, sonochemical reactions, and analytical methods. This chapter will describe initial results from a previously undescribed analytical method. Some physical and sonochemical effects observed during cavitation experiments will be described as well.

A. Acoustic Impedance Measurements

The acoustic impedance of a fluid or solid is the product of its density and the speed of sound in the material. Changes in the acoustic impedance can be caused by variations in properties such as temperature, static pressure, and composition. These changes can be detected as changes in the complex power from the power supply.

Experiments were performed to determine the sensitivity of the complex power meter to changes in sodium chloride concentration. This system was chosen for its simplicity, though many other two component systems could be used.

The acoustic horn described in Chapter III has a bulky, mechanical mass extending from the piezoelectric transducers. This highly dampens the sensitivity of the electrical system to the mechanical load. For this reason, a more sensitive system was chosen. A 1.4 inch diameter 1.0 MHz medical diathermy probe from Dynawave Corporation (Model DW 101) was fitted to the bottom of a flow-through Teflon cylinder cell. The complex power meter was placed in-line between the transducer and a Krohn-Hite 75 Watt (model 7500) AC amplifier. The driving frequency was swept from 490 to 515 kHz for a series of sodium chloride solutions. Figure 8-1 shows the response of the power meter for the complex real power and imaginary powers (See Chapter III, Section A) for several solutions. The effect of raising the acoustic impedance of the load is to raise the frequencies of the local resonances. The selectivity and sensitivity of this method were determined to be inadequate for the desired analysis, but may find use in other applications.

B. Particulate Agglomeration

Agglomeration is a documented effect of cavitation in systems containing small particulates.[1] The high velocity of bubble collapse causes particulates in the vicinity of the liquid interface to rapidly collide. Coupled with elevated temperatures and pressures,

small particulates below a certain size tend to fuse together. Larger particles can be reduced in size by shock waves from symmetrical collapse and jetting from asymmetrical collapse. The equilibrium median size depends on a number of factors including acoustic pressure, particle density, and general fluid characteristics. Agglomeration followed by sedimentation or centrifugation can be used to clarify solutions.[2] While performing experiments on the effects of highly reflective particles on atomic line narrowing,[3] the size distribution of titanium dioxide particulates was observed to change.

In the experiments ~0.05 grams of titanium dioxide was dispersed in 80 mL of water in the 20 kHz acoustic cell. SL experiments were performed, exposing the solutions to cavitation for periods of approximately 6 hours. Some shorter-term ultrasound exposure experiments were performed in beakers. Estimates of particulate size were then made by measuring settling rates and using Stokes law. The solutions were optically opaque, so measurements were made from the top of the fluid level to the top of the sinking front, above which was clarified water. This only provides an estimate of the smallest particle sizes. For uncavitated sample, the settling rate corresponded to a particle size of 110 nm. The solution did not completely clarify, indicating that some particles were small enough for Brownian motion to overcome gravity. Following 15 minutes of cavitation, the smallest particle size was calculated to be 81 nm. After 30 minutes of cavitation, the smallest particle size was calculated to be 72 nm. After 6 hours of cavitation in the cooled cell, the smallest particle size was calculated to be 200 nm. In each case above, the solution above the falling front was mostly clarified after cavitation, indicating that the very smallest particles agglomerated quickly. The 6 hour experiment

left no noticeable cloudiness. Short periods of cavitation are useful for breaking larger particles into smaller ones, while longer periods of cavitation agglomerate those particles into larger sizes. This cursory analysis could benefit from size exclusion chromatography or a surface technique such as SEM, which would both include particle size distributions.

C. Sonochemistry

During the course of studying sonoluminescence, a few instances of sonochemistry were studied or observed. First, sonochemical destruction of sulfur compounds was studied. As petroleum companies have been required to lower the concentration of sulfur compounds in their products, new methods have been sought for desulfurization of petroleum.[4] In response to an invitation to write a grant proposal involving sonochemistry for this purpose, a few initial experiments were undertaken to determine the feasibility of quantifying and destroying sulfur compounds in a representative matrix. The majority of sulfur remaining in gasoline after traditional treatments is in the form of thiophenes (C0-C4 substituted) and benzothiophenes (C0-C2 substituted). The conjugated heterocyclic thiophene was chosen as the most difficult and important molecule to study.

In the 20 kHz acoustic cell samples of n-heptane with and without thiophene were cavitated at 5 degrees Celsius. The cell was pressurized to 38 p.s.i. with argon gas to increase the sonochemical potential. Thiophene concentration was monitored off-line using its UV absorption band with a maximum at 232 nm. Emission spectra for

quantification were not obtained during these preliminary tests. For the first part of the experiment, 80 mL of heptane was sonicated for 2 1/2 hours. Then, thiophene was added to a final concentration of 1800 ppm. One-hundred microliters of 3% hydrogen peroxide was also added to increase the oxidation potential. Sonication continued for another 2 hours. Samples were taken at approximately one hour intervals during these experiments.

Straight chain hydrocarbons have been reported to form conjugated dienes during sonication. These have overlapping absorption bands in the UV. As expected, a peak did slowly grow in with a broad peak at 220 nm. The tail of the peak extended past 300 nm, overlapping the thiophene peak. The shape of the diene peak was interpolated and subtracted to obtain corrected thiophene spectra. The thiophene peak shows a decrease over time with a destruction rate of approximately $5x10^{-9}$ mol/min. While this may appear to be a slow rate, there are several parameters that can be altered to increase efficiency. It should be recognized that ultrasonic degradation is not a linear process. There are thresholds of activation energies, below which sonochemical reactions are not favorable. Increasing the cavitation efficiency by a few percent may bring the system into a condition of more rapid degradation. While the thermostatting bath used in the experiment is not capable of maintaining temperatures below 0 degrees Celsius, temperatures near a solvent's freezing point (-90.6 Celsius for n-heptane) have proven to be optimal for cavitational collapse. Continuously utilizing the static pressure jump effect outlined in Chapter 4D may also increase the sonochemical potential by two or more orders of magnitude.

An interesting observation of the heptane-only part of the experiment above is the rapid destruction of an unknown contaminant, as evidenced by the disappearance of a UV absorption peak at 220 nm. Within two hours of heptane sonication, the peak completely disappeared from an initial absorbance of ~0.2 A.U. This rate of destruction compared to that of thiophene is testament to the main mechanism of sonochemical reactions, secondary reactions with cavitation by-products. If thermal decomposition inside the bubble were the main mechanism, thiophene would have been more rapidly destroyed. Due to its conjugation, thiophene is highly resistant to radical reduction, and the small amount of destruction observed was likely due to the thermal breakdown mechanism.

Another instance of sonochemistry occurred during cavitation of a mercury salt solution. At Hanford Nuclear Reservation, there are storage tanks of various mixed nuclear, organic, and inorganic wastes. Taking and analyzing a single sample is extremely expensive. Currently, there is an on-site project studying the use of ultrasound to degrade organic components to reduce the hazardous complexity of the mixtures. The techniques developed during my project could benefit the Hanford site by allowing simultaneous quantification of dissolved metals, such as sodium, and perhaps mercury. An attempt was made to determine if dissolved mercury (II) chloride would emit MBSL emission lines.

A solution 0.18 M $HgCl_2$ was cavitated at 5 degrees Celsius in the 20 kHz acoustic cell for approximately six hours. While no emission lines were successfully detected, an interesting and perhaps useful observation was made. Cavitation produced a dark-grayish precipitate. Raman spectra of dry, uncavitated $HgCl_2$ and the dried

precipitate (Figure 8-2) were obtained with a Kaiser Raman system, described below in Section D. Compared to literature spectra,[5,6] it appears that the cavitated precipitate is a form of mercury (II) oxide. The spectrum of the cavitated sample displayed Raman lines most similar to the orthorhombic form (171 and 280 cm^{-1}), and unidentified lines as well. These could have arisen from poor crystallinity or non-HgO precipitate. While crystalline HgO is yellow or red in color, powdered Hg_2O is black or brownish black. A mixture of crystalline and amorphous mercury oxides was likely formed, and then agglomerated into larger precipitates by the mechanical forces of further cavitation events. Filtering precipitates formed from dissolved mercury may be an effective method of reducing the toxicity of mercury contaminated solutions. At Hanford, precipitated mercury solids could be vitrified with nuclear species for long term storage.

D. NIR Spectra

In the sonoluminescence literature a number of water MBSL and SBSL spectra appear under varying conditions. Most of these are acquired using sensitive PMTs and spectrometers under low resolution conditions to increase light throughput. The spectra often extend out to 800 nm, with rapidly falling intensity. Due to the absence of NIR spectra in the literature, an experiment was designed in collaboration with Professor Tom Matula at Applied Physics to measure sonoluminescence intensity from 800 to 1050 nm for SBSL and MBSL using a NIR Raman system without the laser. In addition, the presence of the $3d \rightarrow 3p$ transition from 0.1 M sodium chloride was explored for both

cases. Stable single bubble levitation can not be achieved in higher concentrations of sodium chloride.

For the NIR experiments the optics and detector of a HoloLAB Series 5000 (Kaiser Optical Systems, Inc.) fiber coupled Raman system was used without the Raman laser. Two stacked, high efficiency, in-line transmission gratings diffracted the light onto different sections of a 1024 x 256 element TE (thermo-electrically) cooled CCD array. To increase light throughput, a 500 micron slit was used, resulting in 4 nm resolution. Kaiser's HoloGRAMS software was used to collect data, subtract background, and remove cosmic rays.

For the SBSL experiments, the acoustic cell consisted of a 2" diameter round-bottom flask with a 25 kHz cylindrical transducer of 1 inch O.D attached to the bottom. With such a system, a single bubble driven at the appropriate resonant frequency will levitate at the acoustic node against buoyant forces. With each acoustic cycle, it will undergo stable cavitation and emit a flash of SL. A digital waveform generator supplied the resonant frequency to an AC amplifier, which drove the transducer. Solutions were kept at room temperature while SBSL light was focused into a 500 micron fiber optic by a 1.5" bi-convex f/2 lens. Experiments were performed inside a dark box, with the fiber leading to the Raman system. A broad band light source was used to align one focal point of the lens with the levitated bubble. Then, using laser light scattered from the bubble, the fiber was aligned with the other focal point of the lens by maximizing the signal intensity of a PMT at the far end of the fiber. The PMT was then replaced with the Raman system. For MBSL experiments, the 20 kHz acoustic cell replaced the SBSL setup.

The results of the experiments are presented in Figure 8-3 and Figure 8-4 for water and 0.1 M NaCl respectively. The spectra have been intensity corrected using a NIST traceable tungsten source, and corresponding MBSL and SBSL spectra have been normalized at 900 nm for comparison. The accuracy of the intensity correction falls off at the edges of the spectra, where the detector and/or grating efficiencies were lowest. A slight intensity mismatch can also be seen around 910 nm, resulting from errors where the gratings overlap. The NIR tails from SBSL and MBSL are quite similar to their visible spectra. Both continue to decrease in intensity towards lower energy wavelengths. Their profiles were not expected to overlap, as many factors affect MBSL and SBSL spectra. As was the case with the sodium 3p → 3s doublet at 590 nm, the sodium 3d → 3p transition was observed at 819 nm with the MBSL case, but not with SBSL. The reason for the absence of such emission lines in SBSL spectra remains unclear. In the SBSL spectrum a slight decrease in intensity can be seen around 960 nm from the second overtone OH absorption band from the water. This is less apparent in the MBSL spectrum due to short optical path length, as SL occurred very near the observation window with the cavitation bubble cloud causing a significant void fraction.

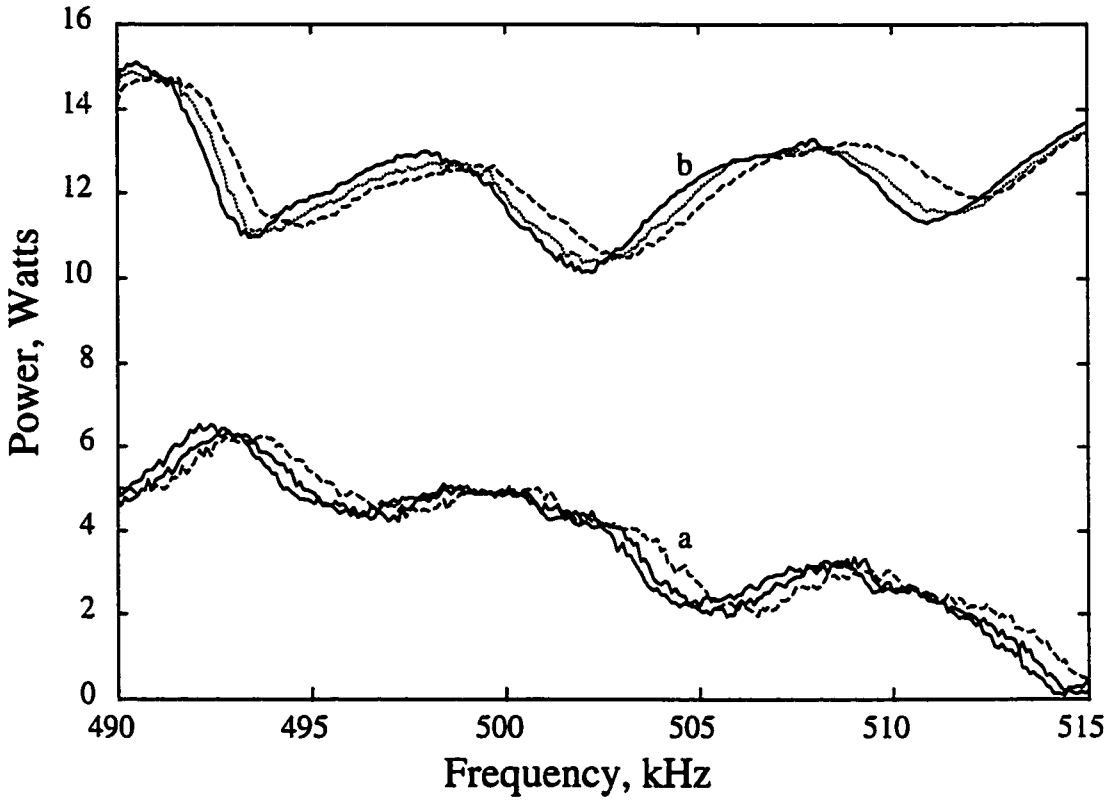

Figure 8-1. Acoustic Impedance Spectrum

A spectrum of real (a) and imaginary (b) power was obtained for three salt concentrations while sweeping the transducer over a range of driving frequencies. Certain frequencies (510 kHz) showed better discrimination, with the imaginary component being more sensitive. Above: DI water (solid line), 0.05 M NaCl (dotted line), and 0.10 M NaCl (dashed line).

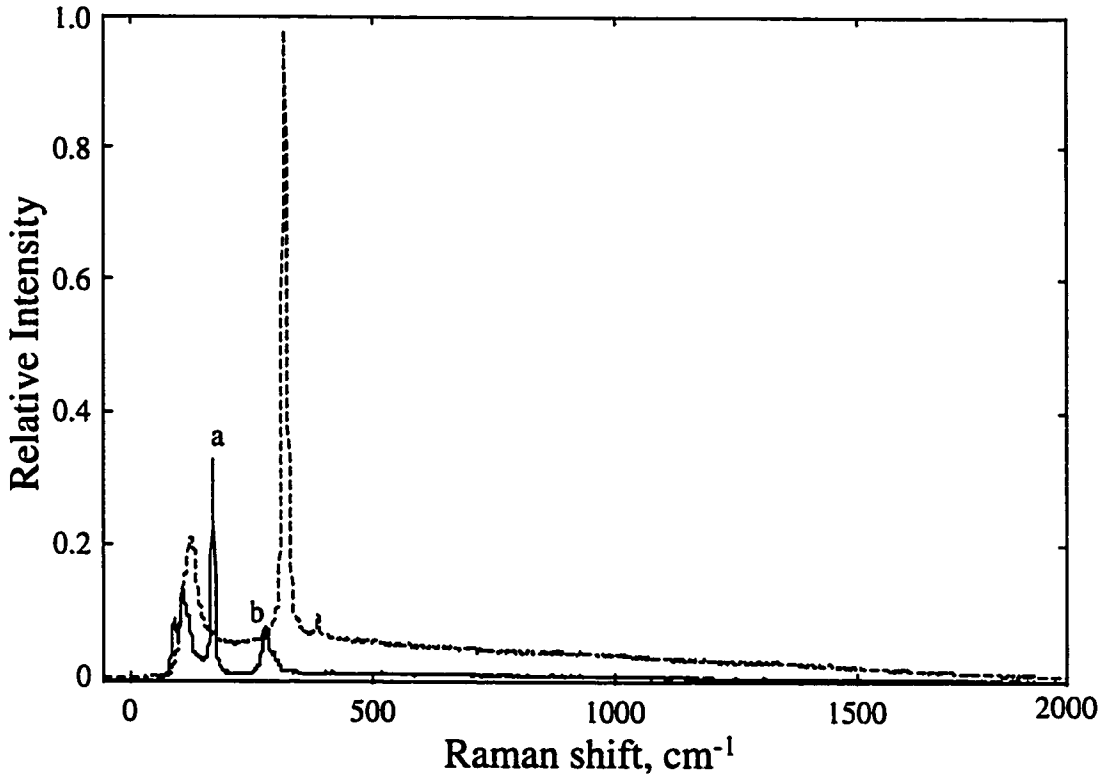

Figure 8-2. Raman of Mercury Precipitates

Raman spectra were taken for fresh (dashed) mercury chloride crystals and a grayish precipitate (solid) collected after cavitation of the same. Lines at 171 (a) and 280 (b) cm^{-1} may result from orthorhombic HgO.

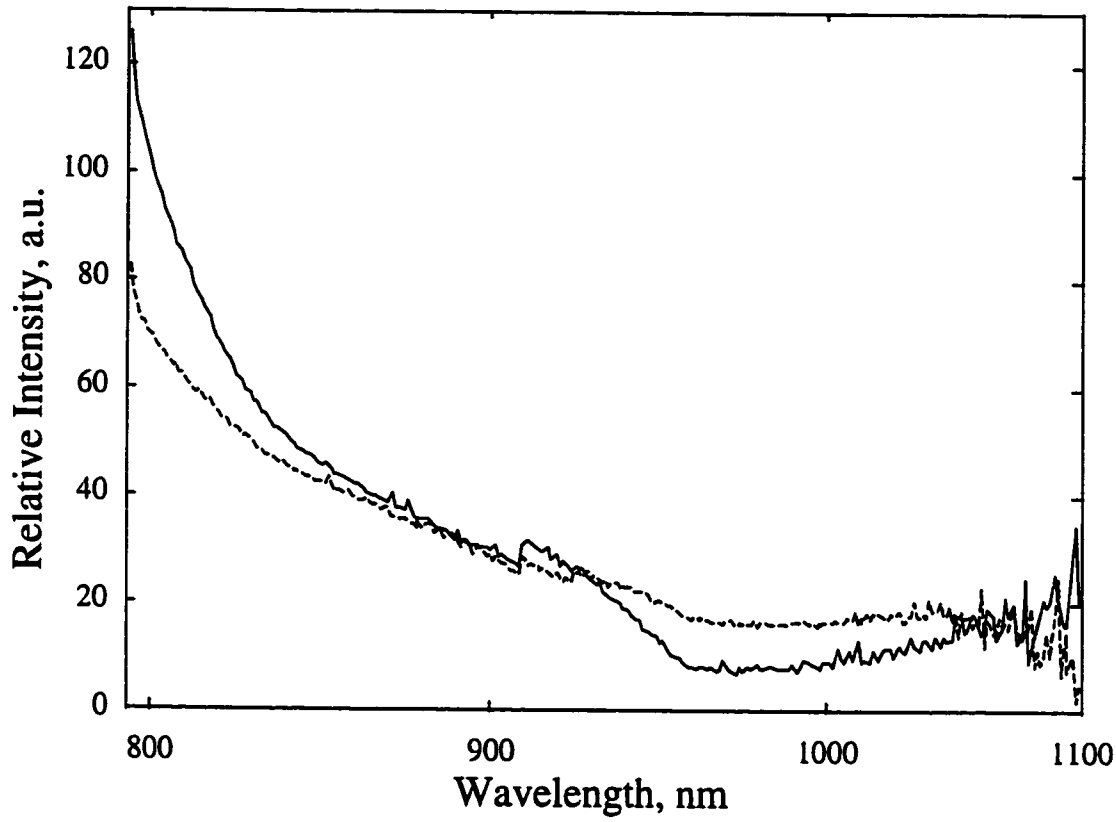

Figure 8-3. NIR Spectra of MBSL and SBSL

Normalized MBSL (dashed) and SBSL (solid) spectra are shown for DI water, obtained using a Raman system with the excitation laser off. An error where the gratings overlap can be seen at 910 nm. The dip between 960-1000 nm in the SBSL curve resulted from second overtone OH absorption from the surrounding water. The spectra are otherwise qualitatively similar.

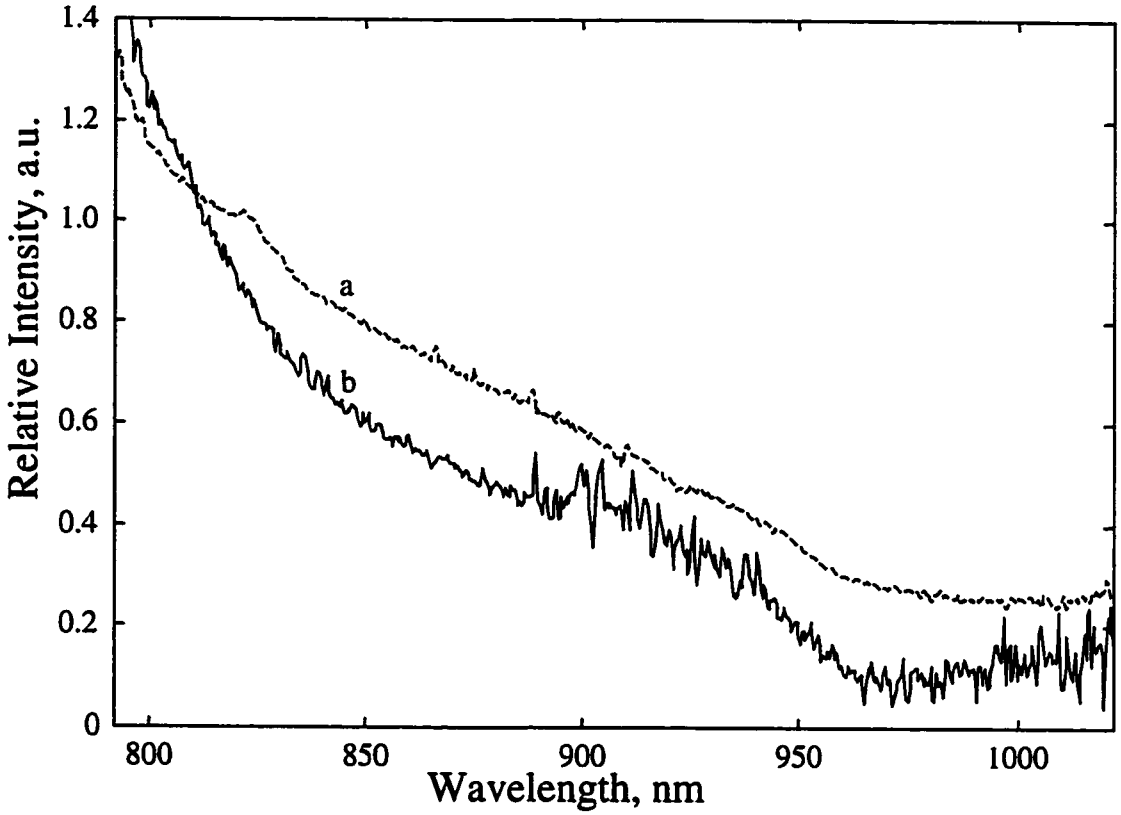

Figure 8-4. NIR SL Spectra with NaCl

Normalized MBSL (dashed, a) and SBSL (solid, b) spectra are shown for 0.1 M NaCl, obtained using a Raman system with the excitation laser off. The sodium 3d → 3p doublet at 819 nm can be seen only in the MBSL case. The OH absorption band between 960-1000 nm is more apparent in this MBSL spectrum than in Figure 8-3. Lower intensity increased the noise for the SBSL spectrum.

Notes to Chapter 8

(1) Suslick, K. S.; Doktycz, S. J.; Flint, E. B. *Ultrasonics* **28**, 280 (1990).

(2) Trampler, F.; Sonderhoff, S. A.; Pui, P. W. S.; Kilburn, D. G.;

Piret, J. M. *Biotechnology* **12**, 281 (1994).

(3) de Oliveira, P. C.; Perkins, A. E.; Lawandy, N. M. *Optics Lett.* **21**, 1685 (1996).

(4) Parkinson, G. *Chem. Eng.* **Aug.**, 48 (2000).

(5) Decamps, E. A.; Durand, M.; Marqueton, Y.; Ayrault, B. *Opt. Comm.* **4**, 358 (1972).

(6) Clark, R. J. H.; Rippon, D. M. *J. Chem. Soc. Farad. Trans. II* **69**, 1496 (1973).

Chapter 9

Conclusions

Sonoluminescence is a fascinating phenomenon that has alluded complete understanding for more than 60 years. Research into its origins has increased exponentially in recent years. The physics community has conducted much of this effort, studying single levitated bubbles and the resulting single bubble sonoluminescence (SBSL). Guided by idealized hydrodynamic theory and highly parameterized computer simulations, attempts at nuclear fusion in otherwise room temperature water have been attempted. While the possibility of producing nuclear fusion is now considered unlikely, there are more realistic applications of sonoluminescence. It has been demonstrated that chemical information is carried on the MBSL signal. It is very sensitive to external experimental parameters and intrinsic properties of the cavitating fluid. If external parameters can be held constant, or closely monitored, reproducible spectra can be obtained, reflecting changes in the intrinsic properties. While the technique is not entirely non-destructive (but nearly so), analysis can be performed *in-situ*, requiring no additional analytes. This is particularly important in harsh environments where sampling can be hazardous and expensive.

The use of sonoluminescence to quantify alkali and alkaline earth metals in solution has been explored. From ionic forms, these metals are reduced to neutral species in electronically excited states during the cavitation process. Emissions from the excited states then occur at wavelengths characteristic to the individual species. These emission lines are significantly broadened, the degree of which is dependent upon the concentrations of that species and of other species in the solution. These concentration dependencies also affect radiation intensity. Spectra obtained from MBSL of salt solutions provide second order data that can be analyzed using multivariate techniques, such as Partial Least Squares analysis. From this, quantification of the salts can be performed.

The origin of sonoluminescence has been debated since its discovery in the 1930s. At least a dozen explanations have been presented from scientists around the world. These have ranged from simple adiabatic heating to more fantastical quantum mechanisms. Most of the physics community has settled on a theory involving plasma generation from a converging shock wave. Assuming a "cold, dense plasma" and Bremsstrahlung radiation, parameterized computer modeling has generated spectra that closely approximate emission spectra from the SBSL case. This model does not address the generation of atomic and molecular emission lines observed from MBSL. Comparisons of experimental MBSL data show strong evidence against a plasma model of SL emission. The analysis does provide support of a cooperative emission mechanism.

The use of acoustics for chemical analysis will continue to become more widespread as advances in equipment and theory continue. While sonoluminescence has

been an interesting curiosity for over 50 years, there are niches in which it could prove to be useful for process analysis, particularly as part of a robust, on-line sensor. For this next step to occur, a sensor needs to be tested with industrial samples under process line conditions. In this instance, a new flow cell would need to be built and characterized for the specific process conditions. Other possibilities exist for using sonoluminescence for analysis. With its sensitivity to surface-active species, it could be used during cleaning validation to determine when detergents and biocides are satisfactorily removed from batch mixers or pipes. An interesting aspect of sonoluminescence that has only briefly been explored is the analysis of organic solutions. Few MBSL spectrum of an organic species have been published. With so many organics liquids, a comparison of their spectra may provide interesting information. In the near-IR to IR region, it may be possible to view vibrational emission bands, indicating the nature of the thermal properties of cavitation bubbles. There are many other interesting aspects to ultrasound. Some of these have been touched on in Chapter VIII, and include chemical and physical transformations, and monitoring ultrasound transmission, reflection, and attenuation to determine chemical properties.

Bibliography

Andreev, A.; Emelyanov, V. I.; Ilinskii, Y. A. **Cooperative Effects in Optics** (IOP Publishing, Philadelphia, 1993).

Ballantine, D. S. Jr.; Rose, S. L.; Grate, J. W.; Wohltjen, H. *Anal. Chem.* **58**, 3058 (1986).

Barber, B. P.; Hiller, R. A.; Loefstedt, R.; Putterman, S. J.; Weninger, K. R. *Physics Reports* **281**, 65 (1997).

Barber, B. P.; Hiller, R.; Arisaka, K.; Fetterman, H.; Putterman, S. J. *J. Acoust. Soc. Am.* **91**, 3061 (1992).

Barber, B. P.; Wu, C. C.; Lofstedt, R.; Roberts, P.; Putterman, S. J. *Phys. Rev. Lett.* **72**, 1380 (1994).

Barber, B.; Wu, C.; Lofstedt, R.; Roberts, P.; Putterman, S. *Phys. Rev. Lett.* **72**, 1380 (1994).

Bjerkness, V. F. K. **Fields of Force** (Columbia University Press, New York, 1906).

Brennen, C. E. **Cavitation and Bubble Dynamics** (Oxford University Press, New York, 1995) p.65.

Brodsky, A. M. *Mod. Phys. Lett. B* **13**, 1019 (1999).

Brodsky, A. M., *J. Math. Phys.* **38**, 5127 (1997).

Brodsky, A. M.; Burgess, L. W.; Robinson, A. L. *Ultrasonics*, accepted for publication as of Sept. 2000.

Brodsky, A. M.; Urbakh, M. *Progress in Surface Science* **33**, 91 (1991).

Clark, R. J. H.; Rippon, D. M. *J. Chem. Soc. Farad. Trans. II* **69**, 1496 (1973).

Craig, V.; Ninham, B.; Pashley, R. *Nature* **364**, 317 (1993).

CRC Handbook of Chemisrty and Physics, 63rd Ed., eds. Weast, R. C.; Astle, M. J. (CRC Press, Inc., Florida, 1982) p. E-294.

Crum, L. A. *J. Acoust. Soc. Am.* **95**, 559 (1994).

Crum, L. A. *Physics Today* **Sept.**, 22 (1994).

Crum, L. A. *Ultrasonics* **9**, 215 (1984).

Crum, L.; Matula, T. J.; Robinson, A. L.; Burgess, L. W., manuscript in preparation.

Decamps, E. A.; Durand, M.; Marqueton, Y.; Ayrault, B. *Opt. Comm.* **4**, 358 (1972).

Didenko, Y. T.; Gordeychuk, T. V. *Phys. Rev. Lett.* **84**, 5640 (2000).

Didenko, Y. T.; Gordeychuk, T. V.; Koretz, V. L. *J. Sound and Vib.* **147**, 409 (1991).

Didenko, Y. T.; Nastich, D. N.; Pugach, S. P.; Polovinka, Y. A.; Kvochka, V. I. *Ultrasonics* **32**, 71 (1994).

Didenko, Y. T.; Pugach, S. P. *J. Phys. Chem.* **98**, 9742 (1994).

Entezari, M.H.; Kruus, P.; Otson, R. *Ultrasonics Sonochemistry* **4**, 49 (1997).

Flint, E. B.; Suslick, K. S. *J. Phys. Chem.* **95**, 1484 (1991).

Franson, M. A. *Standard Methods for the Examination of Water and Wastewater*, 14th Ed. (American Public Health Ass.: Washington, 1976) Part 306.

Frenzel, H.; Schultes, H. *Z. Phys. Chem.* **27B** 421 (1934).

Gaitan, D. F.; Crum, L. A. **Frontiers of Nonlinear Acoustics,** 12th ISNA. (Elsevier Applied Science, London, 1990) pp.459-463.

Gaitan, D. F.; Crum, L. A.; Roy, R. A.; Church, C. C. *J. Acoust. Soc. Am.* **91**, 3166, (1992).

Giri, A.; Arakeri, V. H. *Phys. Rev. E.* **58**, R2713 (1998).

Gordeychuk, T. V.; Didenko, Y. T.; Pugach, S. P. *Acoustical Physics* **42**, 240, (1996).

Gutierrez, M.; Henglein, A. *J. Phys. Chem.* **94**, 3625 (1990).

Hauptmann, P.; Lucklum, R.; Puttmer, A.; Henning, B. *Sens. and Act. A* **67**, 32 (1998).

Heim, V. E. *Z. angew. Phys.* **12**, 423 (1960).

Hiller *et al.* (1998).

Hiller, R. A.; Putterman, S. J.; Weninger, K. R. *Phys. Rev. Lett.* **80**, 1090 (1998).

Ho, C. K.; Moon, G. J. *Jap. J. Appl. Phys. Part 1* **35**, 2758 (1996).

Janata, J. *Principles of Chemical Sensors*; Plenum Press: New York, 1990; Chapter 3.

Jarman, P. D., *J. Acoust. Soc. Am.* **32** 1459 (1960).

Kamath, V.; Prosperetti, A. J. *J. Acoust. Soc. Am.* **94**, 248 (1993).

Kuhns, D. W., Ph.D. Dissertation, University of Washington (1997).

Kuhns, D.; Brodsky, A. M.; Burgess, L. W. *Phys. Rev. E* **57**, 1702 (1998).

Landau L.; Lifshitz, E. **Statistical Physics, Part I** (Pergammon Press, Oxford, 1980) Chpt. 24.

Lentz, W.; Atchley, A.; Gaitan, D. *Appl. Opt.* **34**, 2648 (1995).

Lewschin, V. L.; Rschevkin, S. N. *Compt. Rend. Acad. Sci. URSS* **13**, 399 (1937).

Lohse, D.; Brenner, M. P.; Dupont, T. F.; Hilgenfeldt, S.; Johnston, B. *Phys. Rev. Lett.* **78**, 1359 (1997).

Matula, T. J.; Roy, R. A. *Ultrasonic Sonochemistry* **4**, 61 (1997).

Mohanty, P. http://xxx.lanl.gov/format/cond-mat/0005233

Mohanty, P. http://xxx.lanl.gov/format/cond-mat/9912271

Mohanty, P.; Khare, S. *Phys. Rev. Lett.* **80**, 189 (1998).

Moskovitz, M. *Rev. Mod. Phys. Part 1* **57**, 783 (1985).

Moss, W. C., *et al.*, *Phys. Rev. E* **59**, 2986 (1999).

Moss, W. C.; Clarke, D.; Young, D. *Science* **276**, 1398 (1997).

Münstermann, P.; Fischer, T.; Maunz, P.; Pinkse, P. W. H.; Rempe, G. *Phys. Rev. Lett.* **84**, 4068 (2000).

de Oliveira, P. C.; Perkins, A. E.; Lawandy, N. M. *Optics Lett.* **21**, 1685 (1996).

Parkinson, G. *Chem. Eng.* **Aug.**, 48 (2000).

Parlitz, U.; Mettin, R.; Luther, S.; Akhatov, I.; Voss, M.; Lauterborn, W. *Phil. Trans. Roy. Soc. Lond. Series A* **357**, 313 (1999).

Parsons, M. L.; McElfresh, P. M. *Flame Spectroscopy: atlas of spectral lines* (IFI/Plenum: New York, 1971) p. 47.

Pecha, R.; Gompf, B.; Nick, G.; Wang, Z. Q.; Eisenmenger, W. *Phys. Rev. Lett.* **81**, 717 (1998).

Petrier, C.; Francony, A. *Ultrasonics Sonochemistry* **4**, 295 (1997).

Piret, J. M. *Biotechnology* **12**, 281 (1994).

Prosperetti, A. *J. Acoust. Soc. Am.* **101**, 2003 (1997).

Putterman, S. J. *Scientific American* **Feb.**, 47 (1995).

Putterman, S. *Physics World* **May**, 38 (1998).

Putterman, S.; Weninger, K.; Hiller, R. A.; Barber, B. P. *Proceedings of the 16th International Conference on Acoustics and the 135th Meeting of the Acoustical Society of America*, p. 2837 (1998).

Rosencwaig, A.; Gersho, A. *J. Appl. Phys.* **47**, 64 (1976).

Sehgal, C; Steer, R. P.; Sutherland, R. G.; Verrall, R. E. *J. Chem. Phys.* **70**, 2242 (1979).

Skoog, D. A.; Leary, J. J. *Instrumental Analysis*, 4th Ed. (Saunders College Publishing: Forth Worth, 1992) p. 205.

Storey, B. D.; Szeri, A. J. *Proc. Roy. Soc. Lond. A* **456**, 1685 (2000).

Suslick, K. S.; Doktycz, S. J.; Flint, E. B. *Ultrasonics* **28**, 280 (1990).

Suslick, K. S.; Kemper, K. A. *Ultrasonics* **31**, 463 (1993).

Taylor, K. J.; Jarman, P. D. *Aust. J. Phys.* **23**, 319 (1970).

Trampler, F.; Sonderhoff, S. A.; Pui, P. W. S.; Kilburn, D. G.;

Unnikrishnan, C. S.; Mukhopadhyay, S. *Phys. Rev. Lett.* **77**, 4690 (1996).

Wade, A. P.; Sibbald, D. B.; Bailey, M. N.; Belchamber, R. M.; Bittman, S.; McLean, J. A.; Wentzell, P. D. *Anal. Chem.* **63**, 497A (1991).

Wall, M.; Ashokummar, M.; Tronson, R.; Grieser, F. *Ultrason. Sonochem.* **6**, 7 (1999).

Welsh, W.; Klein, C.; von Schickfus, M.; Hunklinger, S. *Anal. Chem.* **68**, 2000 (1996).

Wiersma, D. S.; van Albada, M. P.; Lagendijk, A. *Phys. Rev. Lett.* **75**, 1739 (1995).

Workman, J. Jr.; Veltkamp, D. J.; Doherty, S.; Anderson, B. B.; Creasy, K. E.; Koch, M.; Tatera, J. F.; Robinson, A. L.; Bond, L.; Burgess, L. W.; Bokerman, G. N.; Ullman, A. H.; Darsey, G. P.; Mozayeni, F.; Bamberger, J. A.; Greenwood, M. S. *Anal. Chem.* **71**, 121 (1999).

Wu, C. C.; Roberts, P.H. *Phys. Rev. Lett.* **70**, 3424 (1993).

Young, F. R. **Cavitation**, (Mcgraw Hill, New York, 1989) p. 2.

Zumdahl, S. S. **Chemistry**, 2nd Ed. (D.C. Heath and Co., USA, 1989), pp. 813, 1048.

Appendix A. Non-Linear Bubble Dynamics in an Acoustic Field

The dynamics of a bubble in a liquid driven by an acoustic field of moderate to high intensity are extremely non-linear due to the great disparity of the densities. Dissolved gas and vapor stream into the bubble while the vapor pressure of the liquid exceeds the surrounding pressure (rarefaction phase), this is a slow process compared to the time scale of the acoustic frequency (25 microseconds for the rarefaction phase at 20 kHz). The result is a vacuous bubble up to 100 times larger than its equilibrium radius. During the compressive phase of the acoustic cycle, the collapse is driven inertially by the weakly compressible fluid surrounding the bubble. With very little internal pressure to retard the surface's advance, the bubble collapses quite violently. While parametric surface instabilities prevent a perfectly symmetric collapse, the radial motion of the bubble can be modeled over more than 99% of an acoustic cycle by classical equations. The following formulas are based on a linearized derivation of the Keller-Miksis[1] model, and are taken directly from a paper by Parlitz et al.[2] A number of variations on these formulas exist, each with its own set of assumptions.

For air and water vapor bubbles in water, the time-radius curve $R(t) = R_0 + R'(t)$ follows Equation 9, the variables of which are defined below. The dot and double dot above the Rs denote first and second derivatives with respect to time.

---

[1] Keller, J. B.; Miksis, M. *J. Acoust. Soc. Am.* 68, 628, 1980.

$$\ddot{R}'+\alpha\dot{R}'+\omega_0^2 R'=-\frac{P_a}{\rho R_0}\cos(\omega t), \tag{9}$$

where

$$\alpha=\frac{4\mu}{\rho R_0^2}+\frac{\omega_0^2 R_0}{c}, \tag{10}$$

and

$$\omega_0^2=\frac{1}{\rho R_0^2\left[3\kappa p_0+\frac{2\sigma}{R_0}(3\kappa-1)\right]}, \tag{11}$$

$R(t)$ = bubble radius as a function of time

$R'(t)$ = radially function of time

t = time

P_a = acoustic pressure amplitude

R_o = equilibrium radius of bubble

ρ = liquid density

ω = radial frequency (2π x frequency)

μ = viscosity

c = sound velocity in liquid

p_o = ambient pressure

σ = surface tension of liquid

κ = polytropic exponent

The dynamics of a bubble in a multiple bubble field or near a rough surface are more complicated and less stable than those of the isolated bubble case. Such a derivation can be found by Nigmatulin.[3]

---

[2] Parlitz, U.; Mettin, R.; Luther, S.; Akhatov, I.; Voss, M.; Lauterborn, W. *Phil. Trans. R. Soc. Lond. A* **357**, 313 (1999).

[3] Nigmatulin, R. I. **Dynamics of Multi-Phase Media**, vol. 1-2. (Hemisphere, New York, 1991).

Appendix B. Complex Power Meter

Instrument Purpose

This circuit was designed to acquire voltage and current information from the loading effects of an ultrasonic transducer driving an experimental load, while providing signal conditioning and conversions for load characterization and calculations.

General Circuit Description

Appropriately scaled and buffered samples of load current and voltage are provided as parametric outputs for direct viewing by means of an oscilloscope or other data acquisition equipment. In addition, there are three more outputs based upon (1) instantaneous power (the instantaneous product of voltage and current), (2) average power (a measure of heating effects on the load), and (3) phase angle (a measure of the time difference between voltage and current expressed as an angular displacement). Each output is expressed as a voltage and is a linear function of the measured parameter whose value can be extracted by multiplying by the appropriate scale factor tabulated below.

PARAMETER	SYMBOL	SCALE FACTOR
Current	$I_{,A}$	(0.1 A/V)
Voltage	$V_{,V}$	(100 V/V)
Instantaneous Power	$P_{,W}$	(100 W/V)
Average Power	$P_{ave,W}$	(100 W/V)
Phase	$\phi,°$	(36 °/V)

Detailed Circuit Description

In operation, this circuit intercepts the output of a power driver by passing the load current through a current transformer, modified from its original ratio of 50:1 to a final ratio of 5:1. This means that a resulting current of one fifth the load current is impressed upon a 50 ohm internal termination resistor resulting in an output voltage of 10 volts per amp of load current, or as expressed by the scale factor, one tenth amp per volt. This signal is then buffered by the follower amplifier, Ul [The nominal RMS current rating of this transformer is 5 amps, but because we have essentially increased the number of primary turns by a factor of ten, the new limit is now 0.5 amps thereby preserving the ampere-turn product limit.].

The voltage applied to the load is sampled by a 100:1 resistive voltage divider. Time constant or phase compensation is accomplished by the 3-60 pF variable capacitor to ground. This mode of compensation is required owing to the parasitic capacitance

across the input 1 K-ohm resistor. As with the current sample signal, the voltage sample is buffered by follower amplifier U2.

Both of the above signals are applied to respective isolation/limit networks composed of a 3.01 K-ohm series resistor and shunt reverse parallel signal diodes. The clamping action of the diodes is required so that the voltages ultimately applied to the dual discriminator, U5 are constrained within their defined operating levels. U3 and U4 buffer the output of the clamp diodes and provide the required low impedance source drive to the U5 discriminator. Also, the positive feedback divider network composed of the 2 K-ohm and 22 ohm resistors provide the necessary hysteresis to preserve stability near zero input voltage. Finally, the 2.94 K-ohm resistor tied to the 5 volt supply biases the divider junction so that the discriminators will change state at a true zero volt crossing, thereby avoiding timing errors which would result from signal amplitude variations.

Outputs from the discriminators are applied to a phase comparator, U6. If the two inputs are time coincident on their positive rising edges, the output on pin 13 will remain in a high impedance state and the output of amplifier U8 will rest at zero volts, thereby indicating an in phase condition. For conditions other than in phase the phase comparator output will exhibit (1) high level (+5 volt) pulses whose widths correspond to a phase lead in the current derived signal, or (2) low level pulses whose widths correspond to a phase lag in the case of a lagging current. Op-amp U8 is part of differential amplifier with appropriate offset and gain of 2 to convert the 0 to 5 volt signal range from the phase comparator to a -5 to +5 volt phase output. The 1 nF input capacitor forms a

passive filter with the R/4 resistors to set a corner frequency of ~12.7 KHz. The 0.1 μF capacitor is part of an effective low pass active filter, placing the final output corner frequency at 16 Hz. The overall effect is to time average the phase pulses into a smooth output whose level corresponds to a phase angle measurement. Finally, U13 is a follower buffer amp with a 49.9 ohm resistor interposed with its output to enable driving an essentially open circuit terminated 50 ohm coax cable connection, thereby providing a back termination for any reflections.

U7 is a fast multiplier used to directly implement the taking of the product of voltage and current applied to an experimental load. Its output voltage is given by the product of voltage and current signals divided by ten (a convenient scale factor, which essentially allows the two input signals and the output signal to occupy the same operating range of values). The multiplier output is directly buffered by U11 for the instantaneous power output signal and also low pass filtered by the 78.7 K-ohm resistor and a 0.1 μF capacitor with a corner frequency of 20.2 Hz. This signal is in turn buffered by U12 to source the average power output signal.

Additional notes

Each of the five outputs uses a 49.9 ohm resistor, as described in the phase measurement path, to provide amplifier isolation from possible reactive loads and provide effective back termination of any reflections resulting from open circuit termination of lab standard 50 ohm cables.

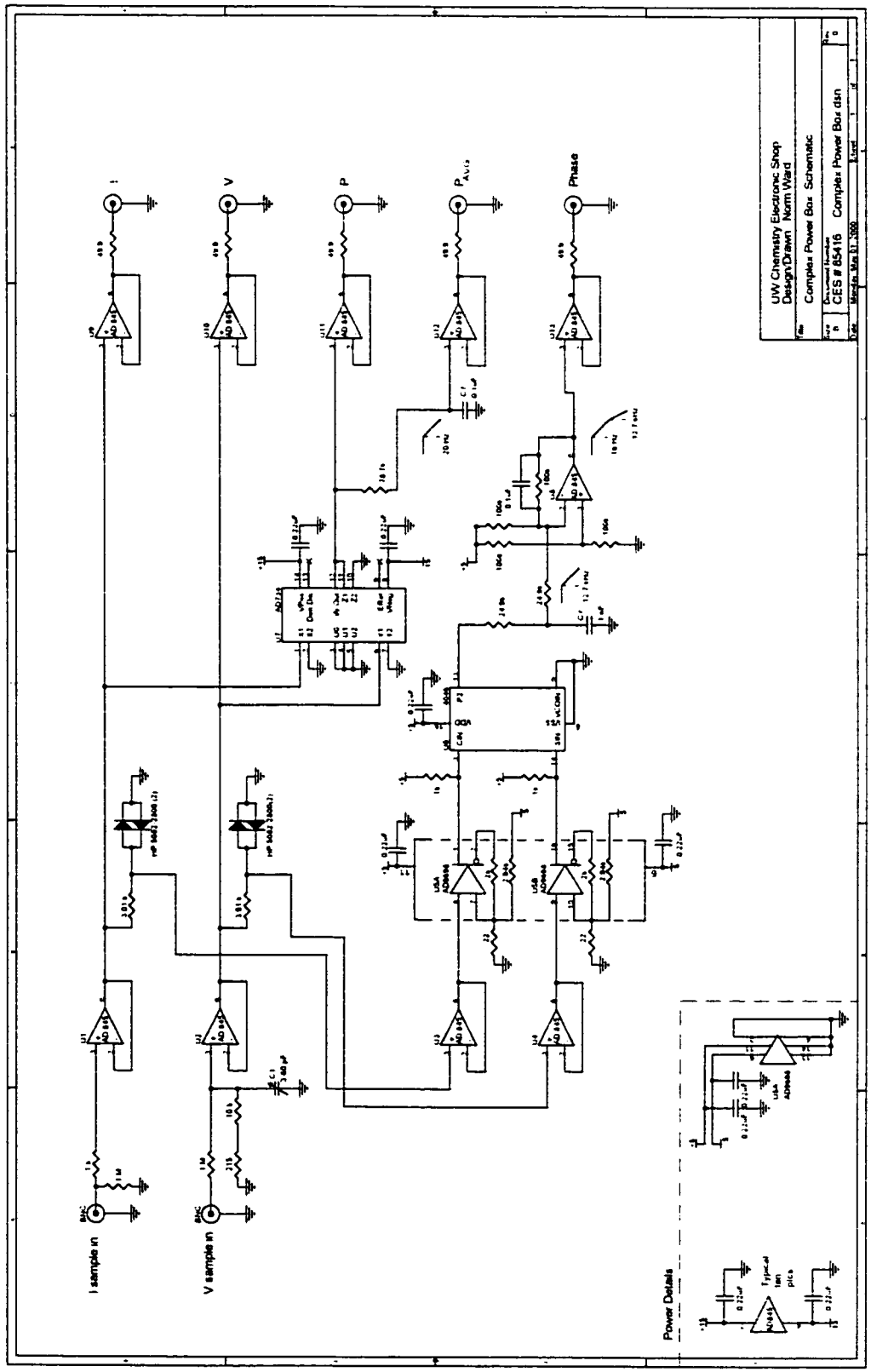
UW Chemistry Electronic Shop
Design/Drawn Norm Ward
Complex Power Box Schematic
CES # 85416 Complex Power Box.dsn
I
V
P
P Aux
Phase
I sample in
V sample in
Power Details

Appendix C. Matlab Programs

Several programs were written in Matlab for data analysis. The most useful were for the removal of localized intensity spikes caused by cosmic rays striking the CCD array. Two examples are included here. The first removes cosmic ray spikes by spatial analysis, and the latter by temporal analysis.

Spatial cosmic ray removal, individual spectrum:

```
%%%%%%%%%%%%%%%%%%%%%%%%% cosmic.m %%%%%%%%%%%%%%%%%%%%%%%%%%%%%%%%%%
%
% This function takes a matrix of CCD values and searches for sudden
% jumps in value, which may be due to cosmic rays.  A plot is
% generated and the user is asked if the value is due to a cosmic ray.
% An answer of 'y[es]' will replace the value with an average of
% surrounding values.
%
% function [outputZ] = cosmic(inputZ,jump), where 'jump' is the
% magnitude of the sudden increase in value to be searched for.
%
% Alex Robinson, Dec. 22, 1997
%
%%%%%%%%%%%%%%%%%%%%%%%%% cosmic.m %%%%%%%%%%%%%%%%%%%%%%%%%%%%%%%%%%


function [outputZ] = cosmic(inputZ,jump)

[m,n]=size(inputZ);

for i=1:n;
  for k=4:m-4;
    a=find(inputZ(k,i)>(inputZ(k-3,i)+jump)&inputZ(k,i)>...
                                          ...(inputZ(k+3,i)+jump));
      if size(a)>0
        plot(inputZ(:,i))
        hold on
        plot(k,inputZ(k,i),'ko')
        eval(['title(num2str(i))'])
        c=input('Cosmic Ray? (y/n) ','s');
        if ~isempty(c)
          if (c=='y')
             inputZ(k,i)=ceil((inputZ(k-3,i)+inputZ(k+3,i))/2);
          end
        end

        hold off
        clf
        clear a c
      end
  end
end

outputZ=inputZ;
plot(outputZ);
```

Temporal cosmic ray removal, set of similar spectra:

```
%%%%%%%%%%%%%%%%%%%%%%%%%%%% cosmic2.m %%%%%%%%%%%%%%%%%%%%%%%%%%%%%%%%
%
% This function takes a matrix of CCD values and searches down the
% wavelength vectors for sudden jumps in value, which may be due to
% cosmic rays. The jumps are assigned new values equal to the average
% of that wavelength vector without the jumps.
%
% function [outputZ] = cosmic6(inputZ,jump), where 'jump' is the
% magnitude of the sudden increase in value to be searched for.
%
% Alex Robinson, April 6, 1999
% modified July 18, 2000
%
%%%%%%%%%%%%%%%%%%%%%%%%%%%% cosmic2.m %%%%%%%%%%%%%%%%%%%%%%%%%%%%%%%%

function [outputZ] = cosmic6(inputZ,jump)

inputZ=inputZ';
[m,n]=size(inputZ);

for i=1:n;
   mn=mean(inputZ(:,i));
   ind=[];
   [ind,temp]=find(inputZ(:,i)>mn+jump);
   if ~isempty(ind)
      sumz=0;
      [ind2,temp]=size(ind);
      for k=1:ind2
         sumz=sumz+inputZ(ind(k),i);
      end
      newmn=(sum(inputZ(:,i))-sumz)/(m-ind2);
      for k=1:ind2
         inputZ(ind(k),i)=newmn;
      end
   end
end

outputZ=inputZ';
plot(outputZ);
```

Curriculum Vita

ALEX ROBINSON

University of Washington
Department of Chemistry, Box 351700
Seattle, Washington 98195-1700
Office phone: (206) 685-8466

4747 30th Ave NE Apartment J160
Seattle, Washington 98105
Phone: (206) 522-2848
AlexR@u.washington.edu

CAREER OBJECTIVE

Obtain analytical research and development position involved with instrument and methods development, process control, analyte identification and quantification.

ACCOMPLISHMENTS

- Advised and conducted research with undergraduates for zero gravity sonochemistry experiments aboard NASA's KC-135.
- Developed a quantitative calibration method using sonoluminescence for Group I and II salts.
- Developed and characterized sonoluminescence flow cells.
- Tested and evaluated pH and conductivity sensors for total organic carbon (TOC) analyzer placed aboard space station *MIR* for high resistivity, potable water supply.
- Established reaction mechanism of a peroxyoxalate chemiluminescent reaction using stopped-flow kinetics.
- Established ionization energy levels of molybdenum monoxide using photoelectron spectroscopy.

EDUCATION

March 2001 — Ph.D., Analytical Chemistry
University of Washington, Seattle, Washington
Advisors: Professors Lloyd W. Burgess and Gary D. Christian
Thesis: "Sonoluminescence for the Quantitative Analysis of Alkali and Alkaline Earth Chlorides"

1995 — B.A., Chemistry, *Summa cum Laude*, ACS Certified
University of Colorado, Boulder, Colorado
Advisors: Professors John W. Birks and Kathy L. Rowlen
Thesis: "Stopped-Flow Kinetics Investigation of the Imidazole-Catalyzed Peroxyoxalate Chemiluminescence Reaction"

PROFESSIONAL EXPERIENCE

1995-2001	University of Washington, Seattle, Washington Graduate Teaching Assistant, Graduate Research Assistant, Center for Process Analytical Chemistry (CPAC); Research Assistant, Applied Physics Laboratories
2000	Private consultation in design and fabrication of acoustic processing cells
Summer 1995	Sievers Instruments, Boulder, Colorado Research Scientist
1994-1995	University of Colorado, Boulder, Colorado Teaching Assistant, Research Assistant
Summer 1993	Joint Institute for Laboratory Astrophysics, Boulder, Colorado Undergraduate Research Assistant

TECHNICAL SKILLS

Analytical Chemistry, Chemometrics, Ultrasonics, Sonochemistry, NIR, IR and UV/VIS Spectroscopy, Sputter Coating, Fiber Optics, Low Level Light Collection, Chromatography, Total Organic Carbon analysis, AA, NMR. Computer hardware, small parts machining, basic electronics. Windows, DOS, Macintosh, and UNIX. Program in LabView, MatLab, Basic.

AWARDS AND ACTIVITIES

- Candidate in Philosophy, University of Washington, 1998
- Phi Beta Kappa, 1994
- ACS Division of Analytical Chemistry Undergraduate Student Award, 1994
- Golden Key National Honor Society, 1994
- PTA, Seattle, WA, present
- UW Kayak Club, 1999
- Student Daycare Planning Committee, University of Washington, 1998
- Club Water Polo, 1991-1994

PAPERS

"Sonoluminescence for the Quantitative Analysis of Alkaline and Alkaline Earth Chlorides," in preparation.

"Cooperative Effects in Sonoluminescence," submitted to *Physical Review Letters*, September 2000.

"Cooperative Effects in Multibubble Sonoluminescence," accepted for publication, *Ultrasonics*.

"Process Analytical Chemistry," *Analytical Chemistry*, v. 71, n. 12, pp. 121R- 166R, 1999.

"Hydrodynamical Perturbation Effects in Multibubble Sonoluminescence," *Proceedings of the 16th International Conference on Acoustics and the 135th Meeting of the Acoustical Society of America*, pp. 1709-1710, 1998.

"Stopped-Flow Kinetics Investigation of the Imidazole-Catalyzed Peroxyoxalate Chemiluminescence Reaction," *Journal of Organic Chemistry*, v. 63, n. 9, pp. 3023-3031, 1998.

PRESENTATIONS

"Cavitation: Using Bubble Dynamics as an Analytical Probe via Acoustic Backscattering and Sonoluminescence," Presentations at biannual meetings of the Center for Process Analytical Chemistry (CPAC), Seattle, Washington, November 1997, May 1998, November 1998, May 1999, November 1999, May 2000.

"Cavitation: Using Bubble Dynamics as an Analytical Probe via Acoustic Backscattering and Sonoluminescence," Presentation at the 26th Annual Conference of the Federation of Analytical Chemistry and Spectroscopy Societies, Vancouver, B.C., Canada, October 1999.

"Cooperative Effects in Sonoluminescence," Presentation at Ultrasonics International '99 and the World Conference on Ultrasonics 1999, Copenhagen, Denmark, June 1999.

"Sonoluminescence for Quantitative Analysis," Presentation at the 54th Northwest Regional Meeting of the American Chemical Society, Portland, Oregon, June 1999.

"Hydrodynamical Perturbation Effects in Multibubble Sonoluminescence," Presentation at the 16th International Conference on Acoustics and the 135th Meeting of the Acoustical Society of America, Seattle, Washington, June 1998.

"Acoustics in Time Domain Reflectometry and Chemical Characterization," Presentation at the Center for Process Analytical Chemistry, Seattle, Washington, November 1996.